ELECTRODE ARCHITECTURES FOR ENHANCED LITHIUM ION BATTERY PERFORMANCE

A Dissertation Presented

By

Sharon Loeffler Kotz

to

The Department of Mechanical and Industrial Engineering

in partial fulfillment of the requirements

for the degree of

Doctor of Philosophy

in the field of

Mechanical Engineering

Northeastern University

Boston, Massachusetts

May 2016

ABSTRACT

Increasing prevalence of portable electronic devices and growing concern over the consumption of fossil fuels have led to a growing demand for more efficient energy storage options. Lithium ion chemistry has grown to dominate the battery market, but still requires improvement to meet the increasing need for smaller, cheaper, better performing batteries. The use of nanomaterials has garnered much attention in recent years as a potential way of improving battery performance while decreasing the size. However, new problems are introduced with these materials such as low packing density and high reactivity with the electrolyte. This research focuses on the development of an electrode architecture using nanomaterials which will decrease lithium ion transport distance while enhancing electrical conductivity within the cell. The proposed architecture consists of a stacked, 2D structure composed of layers of carbon nanotubes and active material particles, and can be applied to both the anode and the cathode. The process also has the advantage of low cost because it can be performed under normal laboratory conditions (e.g. temperature and pressure) and easily adapted to a commercial scale.

TABLE OF CONTENTS

1. Introduction

1.1 Battery Evolution

The concept of energy storage is both familiar and old. Humans have invented myriad ways of storing energy over centuries of scientific progress. Even the storage of electrical energy, a seemingly modern invention, could be as much as 2,000 years old as evidenced by a device known as the Parthian Battery, although there is some debate as to the device's actual purpose. The first recorded battery was created by Alessandro Volta in 1800 and is known as the Voltaic Pile, a stack of alternating zinc and copper discs separated by brine soaked cloth. Since then, many improvements have been made and many new battery chemistries introduced, as illustrated in the timeline in Figure 1 [1].

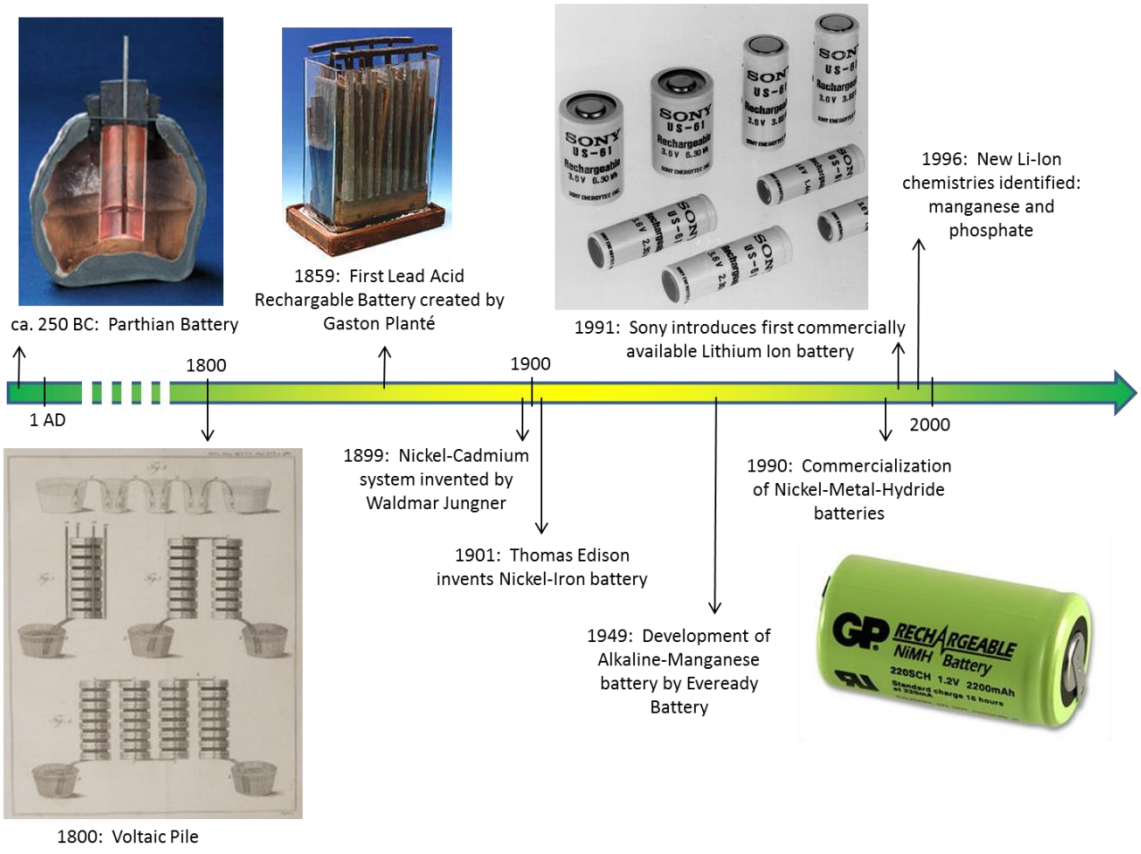

Figure 1: Timeline of Battery Evolution. Image sources: [1-5]

The introduction of the lithium ion battery in 1991 was the last major breakthrough in battery evolution. Since that time, progress has slowed despite increasing demand for more efficient portable power sources. Growing prevalence and shrinking sizes of portable electronics demand smaller, higher performing, and cheaper batteries. The hybrid and all-electric vehicle market is growing due to concerns over the cost and sustainability of fossil fuels, yet most batteries are not up to the standards needed to provide the driving range of internal combustion engine powered cars. Because of these limitations and the ever-increasing push to overcome them, much research is focused on the improvement of lithium ion batteries. The major factors driving the next stages of battery evolution include performance, cost, safety, size and weight, and sustainability.

1.1.1 Performance

Several metrics are used to determine a battery's performance: capacity, power density, energy density, and cycle life are some of the most important. Portable electronics such as cell phones and laptop or tablet style computers are the main application for lithium-ion batteries. Branching out to new applications, however, adds new performance demands. A notable example is hybrid and all-electric vehicles. Unlike portable electronics, which are optimized for high energy, vehicles require both high power and high energy. In addition, phones and computers are generally considered obsolete within a few years, whereas a vehicle is expected to last for a much longer period, so a longer cycle life is required [6-8].

The amount of energy stored in a battery can be improved several ways: by increasing the potential difference between the two electrodes, making the exchange reaction as efficient as possible, and reducing the amount of electrolyte consumed during cycling. These improvements are a function of the battery chemistry used. The first rechargeable batteries, for instance, were lead-acid. These had a potential difference of around 2 Volts. The now-dominant lithium ion battery, however, has a potential difference between 3 and 4 Volts, allowing for more energy storage [6]. Specific chemistries also have different storage capabilities: using lithium manganese oxide (LMO) as an example, $LiMn_2O_4$ has a theoretical

capacity of 148 milli-ampere hours per gram (mAh/g), while $LiMn_3O_4$has a lower capacity of 117 mAh/g [9]. Making an electrode with the same capacity would therefore require less material using $LiMn_2O_4$. To retain this energy, the electrolyte must not react with the active material during cycling. This was a problem for early batteries such as lead-acid, but the introduction of Nickel-Metal Hydride (Ni-MH) and Lithium-Ion batteries greatly improved the electrolyte consumption issue [6]. Figure 2 shows the advances in batteries in the form of a Ragone plot (energy density vs. power density). State of the art rechargeable batteries have steadily improved with each iteration beginning with the lead acid battery, to nickel-cadmium (Ni-Cd) and Ni-MH, to today's lithium-ion. It also shows how far batteries have to go before reaching the performance level of the internal combustion (IC) engine [10].

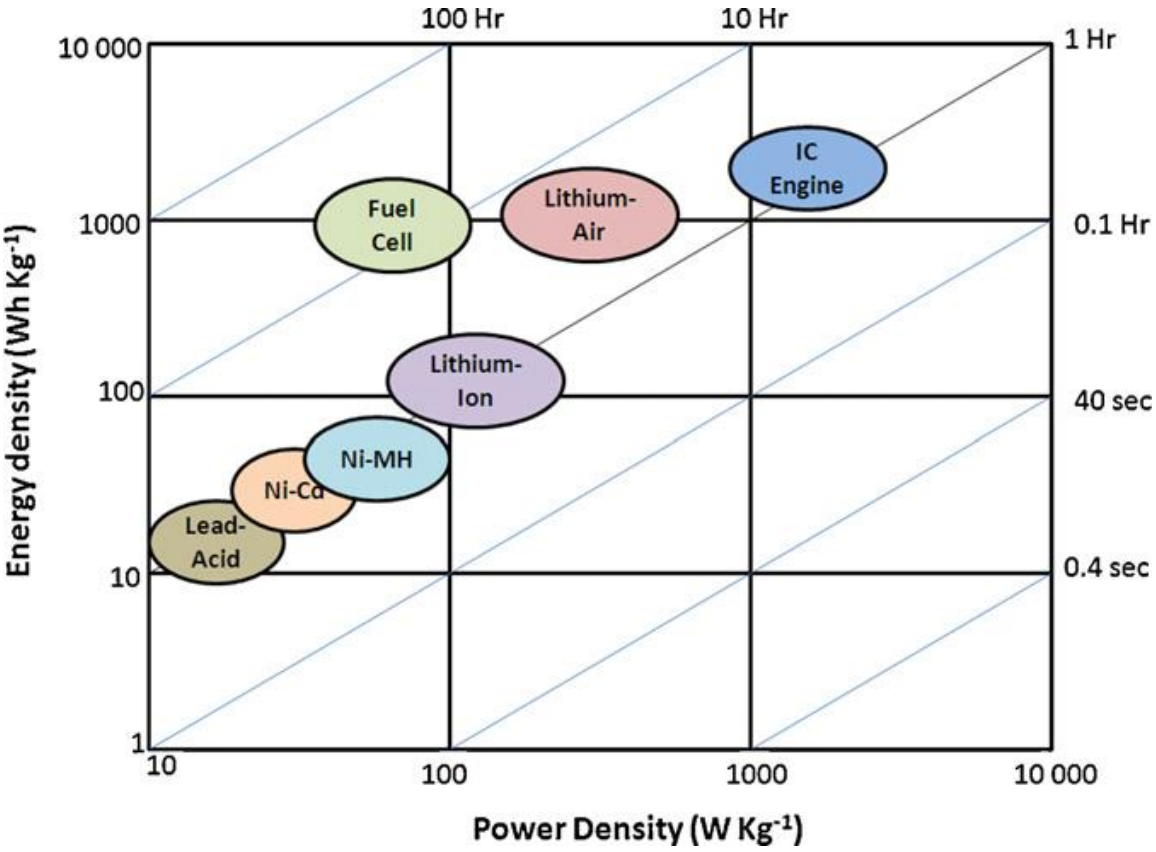

Figure 2: Ragone plot comparing energy and power densities of energy storage systems. Figure source: [10]

Unfortunately, many improvements to batteries come with a cost: the performance parameters are coupled and therefore improving one area often leads to the deterioration of another. One of the most well-known is the trade-off between power and energy density. Cells that have been manufactured to yield high-energy have an internal resistance which makes high-power operation impossible[7, 11]. Another compromise is between charging rate and capacity: in order to charge a battery quickly, one sacrifices capacity. This is the greatest challenge to battery researchers: to improve one or more performance parameters without sacrificing the others.

1.1.2 Cost

The cost of a battery is of course an important factor in its commercial viability. The use of expensive materials or manufacturing processes can render a product impractical for consumer use, even if its performance is an improvement over existing technology. To demonstrate this, consider the case of the electric vehicle: current lithium-ion battery technologies could support an electric vehicle which could drive up to 200 miles on one charge with a 90kWh battery [7]. Using the US Department of Energy's "aggressive" goal of achieving battery production costs of $300/kWh, the battery alone would cost $27,000 [12]. This prices an all-electric vehicle out of the reach of the average American family.

1.1.3 Safety

Safety is one of the primary concerns in creating a commercializable product. Due to the presence of combustible material and oxidizing agents in lithium-ion cells, fires and explosions are the main cause for concern in these batteriesMost current applications do not present a danger, but in order to adapt to more uses, such as electric vehicles, safe operation at higher temperature ranges must be ensured [6, 8, 13, 14].

1.1.4 Size and Weight

There are several reasons to reduce the size and weight of batteries. In the case of portable electronics, the battery takes up a large percentage of the volume, space which could be used for more memory or additional hardware. In the case of electric vehicles, the lighter the car, the less power is needed to drive it. A more dramatic example is space applications. Satellites rely on battery-stored solar power, but weight is a critical issue, since every pound sent into orbit costs $10,000 [15]. It is therefore advantageous to seek materials and manufacturing methods which result in a smaller, lighter battery while still maintaining performance standards.

1.1.5 Sustainability

As the fossil fuel supply dwindles and oil prices rise, the quest for sustainable energy sources has gained momentum. This causes an increasing demand for batteries in electric vehicles as well as grid storage of green energy sources. But the batteries themselves must also be made with sustainability in mind. The manufacturing process and materials to make lithium-ion batteries currently produces around 70 kg CO_2 per kWh, which, while less damaging than current fossil fuel consumption rates, is still fairly high. It has been suggested, however, that improvements to the manufacturing processes, as well as increased recycling programs and new lithium harvesting techniques, could drastically reduce the carbon footprint of lithium-ion batteries [6].

1.1.6 Nanomaterials

The next major step in battery evolution may be the use of nanomaterials. Nanomaterials have garnered much attention in recent years because they offer potential solutions to some of the problems discussed so far. Reducing the size of the active material particles increases the surface area to volume aspect ratio, thereby increasing the available

surface area for electrochemical reactions, providing additional lithium ion storage space. The shortened ion diffusion length associated with nanomaterials leads to better rate capability, and therefore shorter charging times as compared to the same material on a larger scale. Some materials which expand and contract during lithium insertion and extraction are subject to pulverization, but nanoparticles are less likely to experience this, resulting in better cycle stability. While these advantages are attractive, nanomaterials come with disadvantages as well. The reduced particle size results in low packing density, decreasing the volumetric energy density of the cell. The increased surface area also leads to unwanted reactions with the electrolyte, such as the formation of thick solid electrolyte interphase (SEI) layers, causing reduced cycle life. Additionally, the synthesis of some nanomaterials can be complicated and costly, rendering it impractically expensive. The adoption of nanomaterials, while accompanied by some attractive advantages, is thus not a complete solution to the challenges faced by battery researchers [16].

1.2 Project Description

This project is focused on creating a novel electrode architecture which can be applied to any battery chemistry to enhance its performance. The approach is a layer-by-layer fabrication technique utilizing nanomaterials to enhance both the electronic and ionic transport properties of an electrode. Using this architecture, both the power and energy density of the cell can be simultaneously improved without sacrificing other performance parameters. In addition, the fabrication procedure can be performed at ordinary environmental conditions (i.e. room temperature, pressure, and humidity), which makes it low cost as compared to many other nanoscale fabrication techniques. The process is also high-rate and scalable, allowing for easy commercial adaptation.

1.2.1 Research Objectives

There are six main objectives to this research:

1. To develop the aforementioned layered architecture in order to enhance the ionic and electronic conductivities of the electrode.
2. To apply the architecture to both the anode and cathode and compare with electrodes made using standard fabrication methods.
3. To investigate the effects of electrode parameters on cell performance. This includes parameters such as electrode thickness and composition, number of layers, and fabrication method.
4. To examine physical properties of electrodes before and after cycling to enhance understanding of internal changes within the cell due to cycling and assess durability of electrode architecture.
5. To explore various fabrication techniques and develop a process which is low-cost, high-rate, and scalable.
6. To apply this approach to full cells and evaluate performance.

2. Background and Literature Review

2.1 Battery Basics

2.1.1 Working Principle

Every battery contains two electrodes: the positive electrode (cathode), and the negative electrode (anode). In a lithium ion battery, the cathode is typically composed of a transition metal oxide on an aluminum current collector, and the anode is usually a graphitic carbon on a copper current collector. These electrodes are immersed in an electrolyte consisting of a lithium salt dissolved in an organic solvent, and kept isolated from contact by a separator made of polyethylene or polypropylene. This polymer membrane is porous enough

for lithium ions to flow between the two electrodes, but is electronically insulating to prevent electrical shorts in the cell. During charging, lithium ions are extracted from the cathode (de-intercalation), pass through the separator, and are inserted into the anode (intercalation). As the positively charged ions flow through the cell, electrons flow through the external circuit, drawing current from the power source. During discharge, the process is reversed and the electrons flowing through the external circuit provide the current to power the device it is connected to. This process is illustrated in Figure 3.

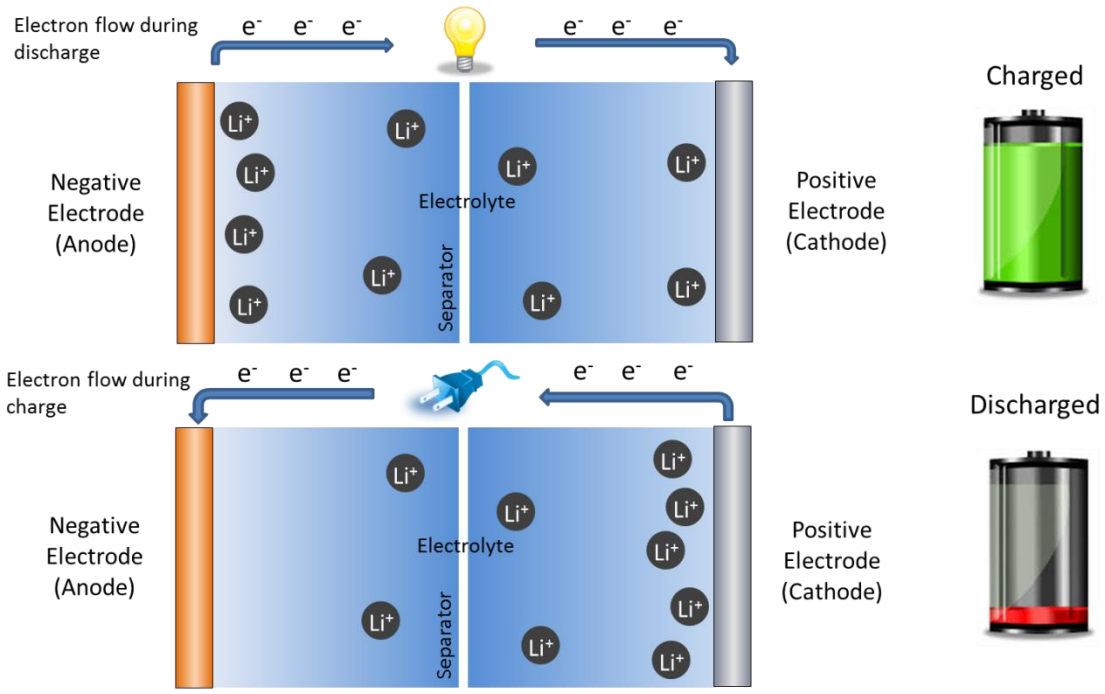

Figure 3: Working principle of a lithium-ion battery

2.1.2 Governing Equations

The amount of energy that a battery can deliver is dependent on the chemical energy stored within the active material. During discharge, this chemical energy is converted into electrical energy via a redox reaction in which lithium ions are extracted from the cathode

material and inserted into the anode material. This reaction is described generally by the equations

$$Cathode:\ aA + ne\ \rightarrow cC$$

$$Anode:\ bB - ne\ \rightarrow dD$$

$$Overall:\ aA + bB\ \rightarrow cC + dD$$

In the cathode equation, a number a moles of A are reduced and n electrons consumed to form c moles of C. On the anode side, b moles of B are oxidized to form d moles of D and n electrons are released. The overall reaction is the sum of the two half cell reactions. More specifically, for a graphite/lithium metal oxide cell, these equations become

$$Cathode:\ LiMO_2 + xe^-\ \leftrightarrow\ Li_{x-1}MO_2 + xLi^+$$

$$Anode:\ C + xLi^+ \leftrightarrow\ Li_xC + xe^-$$

$$Overall:\ LiMO_2 + C\ \leftrightarrow\ Li_{x-1}MO_2 + Li_xC$$

where M represents a transition metal. This redox reaction causes a change in the Gibbs free energy (ΔG) of the system given by the equation

$$\Delta G = -nFV$$

where n is the number of electrons involved in the reaction, F is the Faraday constant (96,485 Coulombs per mole), and V is the potential of the cell in Volts. Thus it can be seen that the open circuit potential of a cell is dependent on the Gibbs free energy of the system [17, 18].

The power output of a battery is related to the potential of the cell by

$$P = VI$$

where P is power, V is voltage, and I is current. Using Ohm's Law, this can be expressed as

$$P = \frac{V^2}{R_i}$$

where R_i is the internal resistance of the battery. The inverse relationship of power and resistance clearly indicates that to maximize the power output of a battery, its internal

resistance must be minimized. As illustrated in Figure 4, there are four main contributors to the internal resistance: the electrical resistance of the bulk electrode material (R_e), the resistance in the electrolyte against lithium ions (R_{sol}), the ionic resistance of the active material (R_{ion}) , and the resistance to electrochemical charge transfer (R_{ct}) [19]. The total internal resistance of the battery is a simple sum of these contributors:

$$R_i = R_e + R_{sol} + R_{ion} + R_{ct}$$

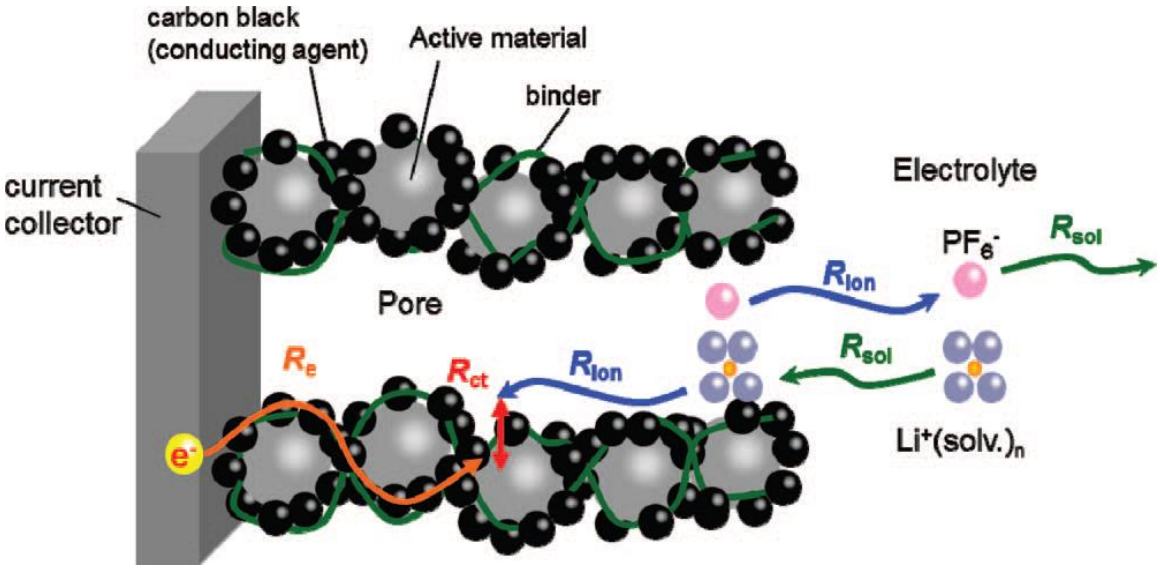

Figure 4: Schematic representation of internal resistances in a lithium ion battery. Figure source: [19]

The electrical resistance of the bulk material can be described by

$$R_e = \frac{\rho t}{A}$$

where ρ is the resistivity of the material, t is the thickness of the electrode, and A is the surface area of the electrode [20]. The resistance due to the electrolyte depends on both the electrolyte itself as well as the geometry of the cell:

$$R_{sol} = \frac{L}{\kappa A}$$

where L is the distance between the electrodes, κ is the ionic conductivity of the electrolyte, and A is again the surface area of the electrode [21]. The ionic resistance is expressed similarly to the first two resistances:

$$R_{ion} = \frac{t}{\kappa_{eff} A}$$

where κ_{eff} is the effective ionic conductivity of the porous electrode [19, 20]. The last term in the internal resistance equation is the charge transfer resistance. The mathematical formulation for the charge transfer resistance originates from the Butler-Volmer equation [22]:

$$i = i_0\left(e^{-\alpha n f \eta} - e^{(1-\alpha) n f \eta}\right)$$

Here, i is the current, i_0 the exchange current, α the reaction order, and n the number of electrons involved in the reaction. The term f represents F/RT, the Faraday constant over the gas constant times the temperature. The term η represents the overpotential, $E - E_{eq}$, the potential of the electrode minus its equilibrium potential. When the overpotential is small, a Taylor series reduces this equation to

$$i = i_0(-nf\eta)$$

The charge transfer resistance is the ratio of –η/i, which can now be expressed as [22]

$$R_{ct} = \frac{RT}{nFi_0}$$

The above equations show that the internal resistance of a battery depends not only on the materials used, but also on the environment (e.g. temperature) and the cell geometry. The thickness of the electrode, for example, increases both the electrical and ionic resistance of the active material. It has been demonstrated that increasing the thickness of the active material layer decreases both the capacity and rate capability of the electrode, as shown in Figure 5 [23]. Unfortunately, this means that increasing the capacity of a battery is not a simple matter of adding more material.

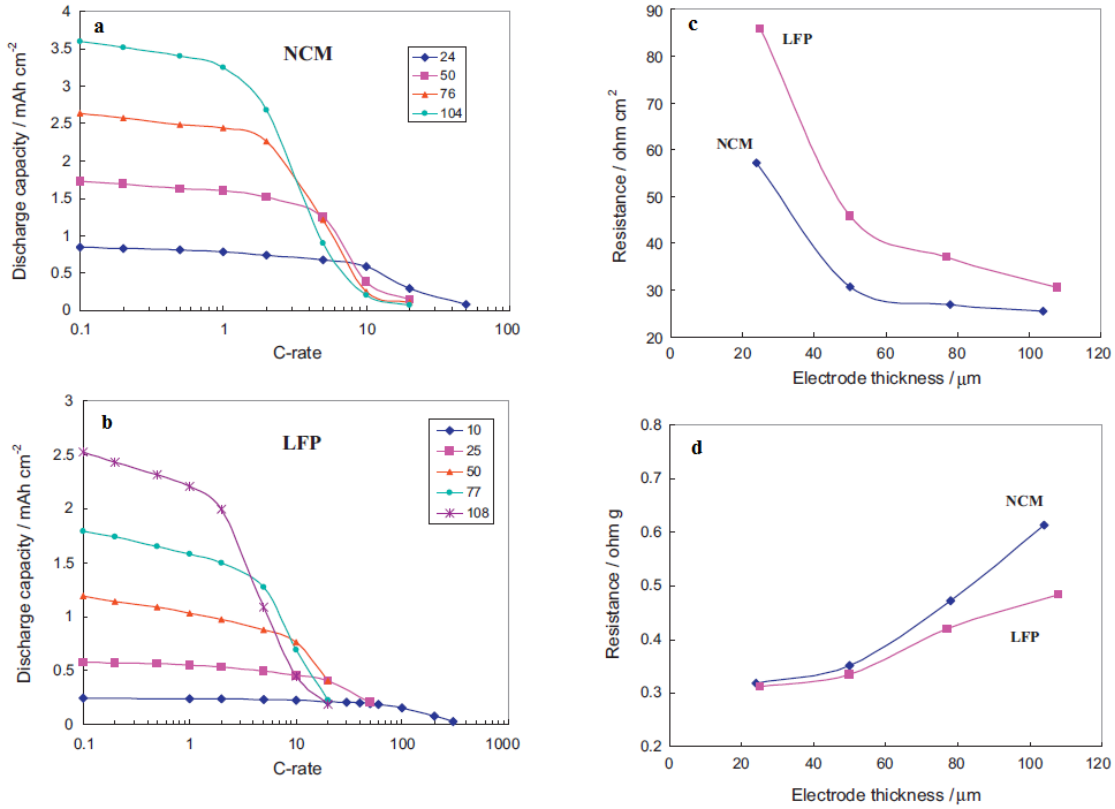

Figure 5: Dependence of battery capacity and rate capability on electrode thickness for two materials, NCM and LFP (a & b respectively): legend entries refer to the thickness of the material in microns; and effect of electrode thickness on internal resistance for the same materials (c & d). Figure source: [23]

2.2 Commercial Batteries

2.2.1 Manufacturing Techniques

The manufacturing process for making most types of batteries is very similar. The material must first be mixed into a slurry suitable for spreading onto a substrate. This slurry contains the active material for either the cathode or anode in a solvent as well as a conductive additive (usually carbon) and a binder. To keep the cell as efficient as possible, the percentage of the last two ingredients is kept to a minimum. The carbon is added to improve the conductivity within the electrode, as many active materials used in batteries are insulating or semi-conducting. The binder, generally a polymer, is added for adhesion, so the material stays

in contact with the current collector and does not flake off during fabrication or cycling. Once this slurry is well mixed, it is coated onto the current collector: usually aluminum foil for the cathode and copper foil for the anode. The current collector provides structural stability for the electrode and an electrical connection to the terminals of the battery. The coating, or calendaring, process can yield micron-precision active material layers, which allows the battery to be tuned to the right application (high-power or high-energy). The electrode is then heated until it is dry and compressed to ensure good contact with the current collector. It is then cut to the appropriate size and hermetically sealed in a metal container which provides the external circuit contacts [24].

2.2.2 Cell Configurations

There are four common battery cell configurations: cylindrical, coin, prismatic, and pouch cells. Examples of each are shown in Figure 6 [25].

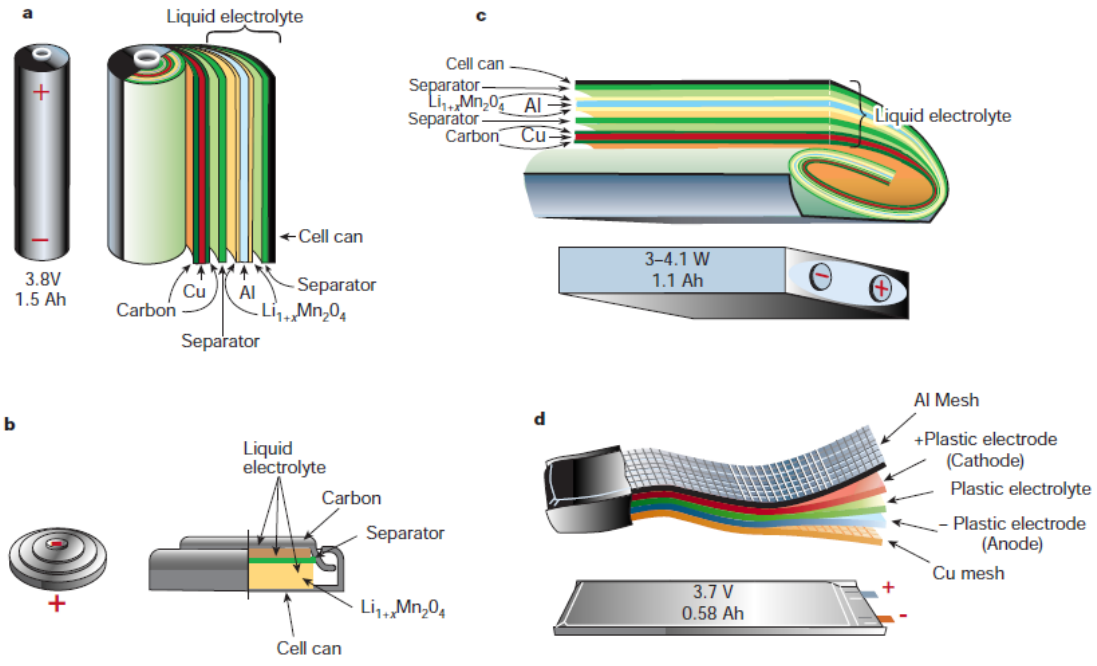

Figure 6: Common battery cell configurations: (a) cylindrical, (b) coin, (c) prismatic, (d) pouch. Figure source: [25]

The cylindrical cell (illustration a in Figure 6) was the first commercial battery packaging to be introduced, starting in 1896. Due to ease of manufacturing, it is still a popular design today with familiar cells such as the AA size. It consists of long rectangular double sided electrodes wound around an inner shaft with a separator in between. This configuration allows for large amounts of active material to be present without increasing the thickness of the material layer, creating a cell that can deliver both high energy and relatively high power. For this reason, they have a wide range of applications including power tools, portable computers, and even some electric vehicles. One of the most common lithium ion cells of this type is the 18650 cell, so named for the size: 18 mm in diameter and 65 mm in length. An 18650 cell using lithium manganese oxide can deliver 1.2-1.5 Ah capacity; lithium cobalt oxide gives 2.4-3 Ah [26].

The coin, or button, cell (illustration b in Figure 6) was introduced in the 1980s to meet the demand for smaller batteries to power portable electronic devices. These cells are not only small enough to power devices such as watches and hearing aids, they are also inexpensive to manufacture and can be stacked in series to supply higher voltage. The drawback to these cells, however, is the lack of a safety vent to prevent gas buildup, which prohibits charging at high currents [26].

Prismatic cells (illustration c in Figure 6) are similar to cylindrical cells in concept, but instead of being wound around a circular shaft, the electrodes are folded into a flat rectangular shape. These cells were invented in the 1990s as portable electronics became more and more popular, and are still predominantly used by devices such as cell phones. Advantages of these cells include a thinner format and excellent space utilization, resulting in higher volumetric capacity. This configuration also offers more flexibility in shape and size as compared to cylindrical cells, so manufacturers can tailor the cell to fit the device. Disadvantages include a thicker cell wall to compensate for lowered physical robustness, less efficient thermal management, and lowered cycle life. A typical prismatic cell for portable electronics can deliver anywhere from 0.4 – 2 Ah capacity; larger versions have been designed to yield up to 20 – 30 Ah [26].

In 1995, the pouch cell (illustration d in Figure 6) was introduced. It is similar to a prismatic cell, but lacks the hard external packaging and merely has two protruding metal foil tabs as terminals. This cell provides the lightest and most space efficient packaging of all the cells, although the lack of a supportive case means it must have some alternative means of

support to prevent damage, and also makes it more vulnerable to heat and humidity. Another concern with pouch cells, like coin cells, is gas generation, as there is no vent and pouch cells have been known to swell during cycling.

2.3 Lithium Ion Battery Materials

2.3.1 Cathode Materials

Lithium ion battery cathodes are typically made of transition metal oxides coated onto aluminum. Since the cathode is usually the limiting factor in the capacity of the cell, there is much interest in improved cathodic materials. Lithium metal oxides are arranged in a crystal structure which allows them to reversibly intercalate lithium ions, making them good candidates for rechargeable batteries. They can be further classified by the shape of their crystal structure: layered, spinel, or olivine. Illustrations of each type can be found in Figure 7 [27].

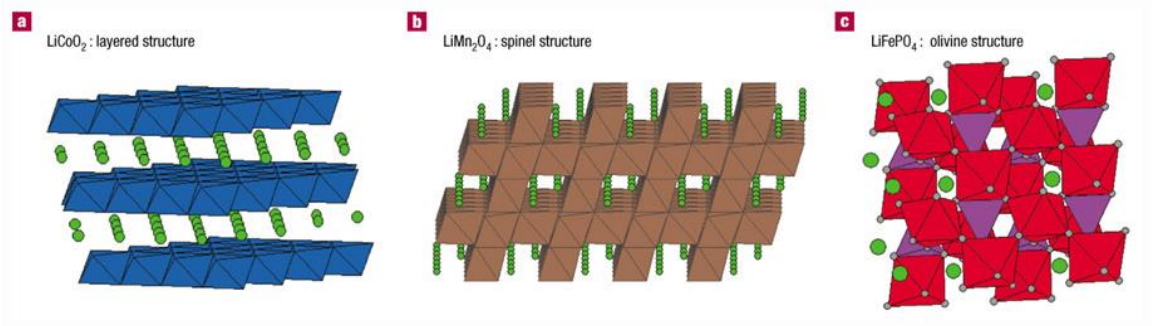

Figure 7: Cathode material crystal structures: (a) layered, (b) spinel, and (c) olivine. Green circles represent lithium ions. Figure source: [27]

The most prevalent cathode material is lithium cobalt oxide ($LiCoO_2$, or LCO), a compound with a layered structure (illustration a in Figure 7). It is commonly used in battery cells for phones, computers, and digital cameras because of its high specific energy. The main disadvantage of LCO is its inability to be charged at high currents; it must be limited to a charge rate of no more than 1 C. Higher C-rates risk overheating, a major safety concern for LCO: at

high temperatures, LCO decomposes to produce oxygen, a reaction that can lead to thermal runaway within the cell as well as in adjacent cells. This results in a very unstable situation and renders LCO unsafe to use at higher temperature ranges [26, 28]. Properties for LCO and other common cathode materials can be found in Table 1.

The improved mobility of lithium ions in the spinel structure (illustration b in Figure 7) lowers the internal resistance and allows for better rate capability, as well as improved safety. One of the most promising compounds of this class is lithium manganese oxide ($LiMn_2O_4$ or LMO), although it does have its drawbacks: lower specific energy and capacity compared to LCO, as well as capacity fade issues due to manganese dissolution in the electrolyte. The capacity fade can be markedly improved, however, with certain synthesis techniques [9, 26, 28, 29].

The olivine structure (illustration c in Figure 7) has the lowest internal resistance due to easy lithium ion flow paths within the structure. This makes it capable of charging at very high rates and able to operate at very high temperatures with little risk of fire. Some cells have even been shown to perform better at higher temperatures than low [30]. Additionally, these cells have longer life spans than LCO or LMO electrodes. The tradeoff, however, is comparatively low specific energy and low voltage. This class is composed of phosphate compounds, most notably lithium iron phosphate ($LiFePO_4$ or LFP) [26, 28].

Recent research focuses on making modifications to these common base materials in order to improve the properties the electrode can offer. Common approaches include cation and anion substitution, useful for enhancing stability of the material during charge and discharge, and insertion of structural units to create energetically favorable pathways for lithium ions. An example of cation insertion is found in the LCO derivative material, $LiNi_{0.80}Co_{0.15}Al_{0.05}O_2$, in which Al^{3+} ions provide greater binding energy in the layered structure, making it more stable during delithiation. This increased stability can raise the practical capacity of the cathode from about 160 for LCO to 180 mAh/g for the altered material [31]. An even greater capacity increase can be achieved using the method of stabilizing structural units, such as in the case of lithium-rich layered transition metal oxides. By inserting the structural unit xLi_2MnO_3 into the transition metal oxide serving as the active material (denoted $(1-x)LiMO_2$, where M could be Mn, Co, or Ni) a more stable overall structure can be attained, while still providing efficient ion transport pathways. These materials can reach capacities of 230-250 mAh/g, however they still have

disadvantages, such as a large irreversible capacity in the first cycle due to activation of the Li_2MnO_3 and poor rate capability [31-34].

Another approach to cathode material is taken by lithium-air batteries in which gaseous oxygen serves as the cathode and lithium metal as the anode. Lithium-air batteries have an extremely high energy density comparable to that of gasoline, which makes them an attractive choice for electric vehicles. There are still challenges to lithium-air batteries, however, including low power density and energy efficiency as well as safety and stability concerns since the lithium metal anode is very reactive with moisture in the air [10, 35].

	Working Potential vs. Li/Li+ (V)	Theoretical /Experimental Capacity (Ah/kg)	Theoretical /Experimental Energy Density (Wh/kg)	Maximum Discharge Rate	Electrical Conductivity (S/cm)	Diffusion Coefficient (cm^2/s)	Cost (USD/kg)	Cycle Life	Safety at High Discharge Rates and Temperatures
$LiCoO_2$	3.6	273/162	980/648	C/2	10^{-4}	10^{-10}-10^{-8}	20-50	800	Poor
$LiMn_2O_4$	4.1	148/120	620/504	5C	10^{-6}	10^{-11}-10^{-9}	10-15	500	Moderate
$LiFePO_4$	3.5	170/150	580/515	30C	10^{-9}	10^{-14}-10^{-5}	20-25	2000	High

Table 1: Properties of common cathode materials. Source: [17, 36]

2.3.2 Anode Materials

Originally, lithium ion batteries used a pure lithium metal anode. The abundance of available lithium ions in the system allowed for high capacity cells, but there were serious safety issues: lithium plating on the anode caused short circuits in the cells, leading to severe overheating. Today's batteries use a carbon, usually graphitic, anode, which avoids the plating problem while simultaneously reducing the overall toxicity of the cell. Graphite is structured into planes with lithium ion intercalation sites between the planes, as shown in Figure 8. It has a theoretical capacity of 372 mAh/g and good cycle stability because the intercalation is reversible and has no effect on the structure of the graphite [26].

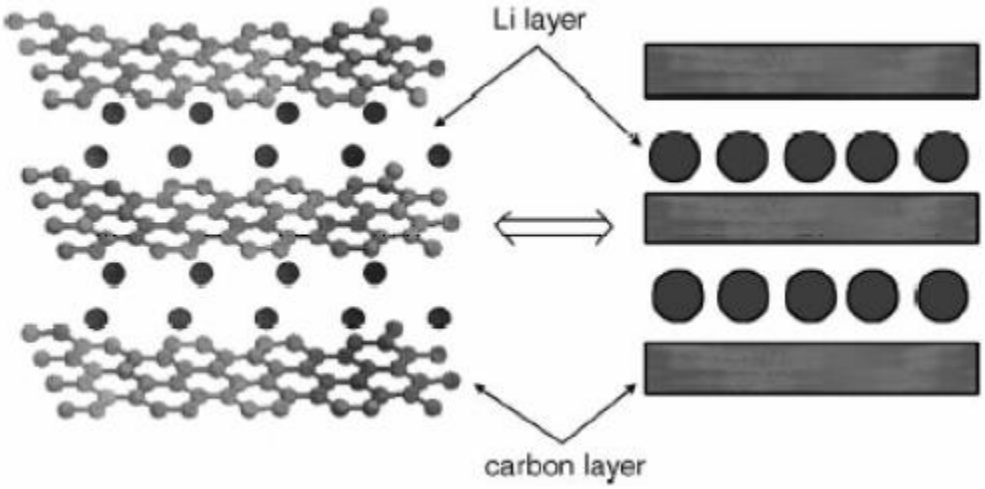

Figure 8: Intercalation of lithium ions into a graphite anode Figure source: [37]

There are many materials available for use in anodes, however, and among these, graphite has a fairly low capacity. Replacing graphite with an alternative, higher-capacity substance would mean being able to use less material in the anode to match the same amount of cathode material, thereby making the cell lighter and thinner. This can be accomplished by using one of a number of elements belonging to a class of higher capacity anode materials, including germanium, tin, and silicon. Of these, silicon has the highest known theoretical capacity, at 4200 mAh/g, more than eleven times that of graphite. For this reason, along with silicon's low discharge potential, natural abundance, and low cost, much current research is

focused on silicon anodes for lithium ion batteries. Silicon owes its high capacity to its ability to incorporate 4.4 lithium ions per silicon atom. However, this is also the cause of its biggest drawback: the incorporation of lithium ions causes the silicon to expand to 400% of its original size and then shrink again as the lithium ions are extracted. With extended cycling, this repeated expansion and contraction causes pulverization of the silicon, which in turn causes loss of contact with the current collector, as illustrated in Figure 9. Because of this, silicon is subject to severe capacity fade [39-51]. This expansion also causes the solid electrolyte interphase (SEI) layer, which is a passivating layer that forms due to the interaction between the active material and electrolyte during cycling, to crack and reform, eventually building up a very thick insulating layer and isolating the silicon [42]. This process is shown in Figure 10.

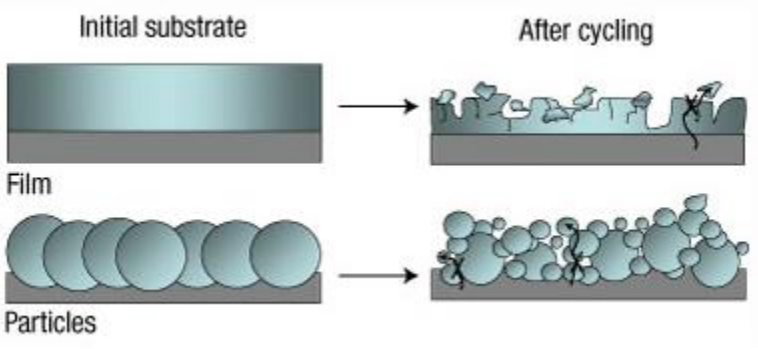

Figure 9: Illustration of silicon pulverization during cycling. Figure Source: [39]

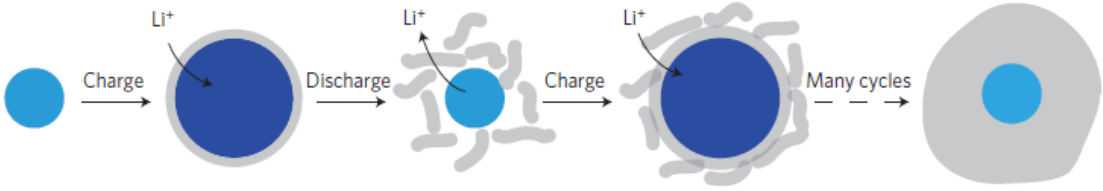

Figure 10: SEI layer buildup during cycling. Figure Source: [52]

There have been many attempts to solve silicon's capacity fade issue. The most common strategies include incorporation of vacant space in the electrode structure to allow for expansion, use of composite materials, and stabilization of the SEI layer. A comparison of some capacity fade mitigation strategies can be found in Table 2.

Some of the most successful silicon anodes owe their high capacity retention to the vacant space built into the material. A few examples of this include hollow spheres or tubes. The hollow sphere method creates what the researchers termed a "yolk-shell" structure, where a silicon particle (the "yolk") is encased in a sphere of carbon (the "shell"), with a void in between. The silicon rests in contact with the bottom of the carbon shell, which is conductive, allowing electrons and ions to be transported through the electrode. When the silicon particle intercalates lithium ions, it expands, filling the void between it and the encapsulating carbon sphere, but the overall shell structure does not expand, which lessens the problem of material degradation and allows electrical contact to be maintained over many more cycles. Using this method, the researchers reported 74% capacity retention after 1000 cycles. In comparison, bare silicon particles have essentially 0% capacity retention after only 50 cycles. The capacity of these spheres was over 2800 mAh/g at a rate of C/10, but only about 630 mAh/g at 4C [41].

Using a similar idea, Wu et al. created double walled silicon nanotubes with a hollow tube of silicon coated in a mechanically confining silicon oxide outer layer. During lithiation, the inner silicon layer expands inward, filling the empty core of the tube. Like the sphere structure, this lessens degradation of the material and also promotes a stable SEI layer since it is not being constantly broken and reformed. The researchers reported a capacity of 940 mAh/g at the high rate of 12 C, and a remarkable 88% capacity retention after 6000 cycles at 10C. The loading reported for these electrodes, however, was 0.02-0.1 mg/cm^2, which is nowhere near the necessary loading for commercial batteries, which will usually have 10-40 mg/cm^2, depending on the application [42]. In addition, these silicon nanotubes, the hollow spheres above, and similar methods generally involve complicated and costly synthesis routes in order to create the necessary void space, rendering them impractical for commercial use.

Another approach with less expensive synthesis options is to use silicon composite materials. The idea behind this approach is that replacing some of the silicon with another anode material such as graphite will result in less overall expansion of the active material layer, but the filler material still contributes to the capacity of the cell. Zhang et al. simply ball-milled silicon, graphite, and CNTs together to make a composite material, significantly simpler and cheaper than the hollow structures described above. The drawback, however is reduced capacity retention: only 25% after 20 cycles. They obtained a stable reversible capacity of 584 mAh/g [53], which is an improvement over graphite, but still does not take full advantage of

silicon's capabilities. Lee et al. used a slightly more complicated synthesis route to create a silicon/graphene composite paper anode in which the silicon particles were dispersed in between sheets of graphene. This method yielded a higher initial capacity of more than 2200 mAh/g, and higher capacity retention, but still faded by about 50% after 300 cycles [47].

Several groups have tried using silicon decorated CNTs as a composite material. Wang et al. reported a capacity of over 900 mAh/g at 2.5C using this method and an average capacity fade of 0.15 mAh/g per cycle over 25 cycles, although this does not include the 20% loss in the first cycle, and long term testing was not yet carried out. This technique includes the use of a high temperature and often low-yield chemical vapor deposition (CVD) process, which would make it expensive to commercialize [48].

A final example of a silicon composite material (more can be found in Table 2) is carbon coated silicon particles. Although similar in theory to the hollow carbon spheres discussed previously, these silicon particles are directly in contact with the carbon coating, with no void in between. This means that the synthesis for these particles is simpler, but they also do not receive the advantages that the vacant space provides. Hu et al. showed a reversible capacity of approximately 1100 mAh/g (at ~C/20) using carbon coated silicon particles, but a 50% capacity loss in the first cycle alone. In this case, the restrictive carbon coating seems to inhibit the intercalation of lithium, as shown by the comparison to bare silicon particles, which had an initial capacity exceeding 3000 mAh/g. However, the bare silicon quickly fades to almost no capacity at all, while the carbon coated silicon showed very little fading (with the exception of the first cycle loss) even at a rate of around 4C [46].

A similar idea is to increase the conductivity of the silicon particles themselves by using doping. Doping is a process in which impurities are introduced to alter the properties of a material. There are two types of doping: negative (n-type) and positive (p-type). N-type doping is accomplished by introducing an atom with one more valence electron than the base element lattice structure. This extra electron is not needed to complete the bonds between the atoms and is therefore free to participate in conduction, making the overall conductivity of the material higher. In the case of silicon, which has four valence electrons, phosphorus is usually used for n-type doping, since it has five valence electrons. P-type doping is just the opposite: an atom with one fewer valence electrons is introduced, which leaves a hole in the bond structure, thereby giving the material a positive charge. With silicon, this type of doping is usually

accomplished with boron [54]. Liu et al. reported that silicon particles doped with phosphorus (n-type doping) have a conductivity six orders of magnitude higher than plain silicon, and two to three orders of magnitude higher than carbon coated silicon [55]. Chakrapani et al. performed cycling tests on undoped, n-doped, and p-doped silicon and found that n-doped showed the highest capacity, although it did not solve the problem of capacity fade [56].

An entirely different approach is to alter the binder or electrolyte used in cell fabrication. The traditional binder is polyvinylidene fluoride (PVDF), however it has been shown that PVDF does not accommodate the expansion of silicon well [57]. Alternatives include carboxymethyl cellulose (CMC), polyaniline (PANI), or even self-healing polymers (SHP). Li, Lewis, and Dahn investigated the effects of replacing PVDF with CMC and found that after 70 cycles, plain silicon particles in PVDF returned almost no capacity, while those in CMC showed a capacity exceeding 1100. They suggest that the CMC may be aiding in creating a more stable SEI layer [57].

Another potential binder is PANI, attractive because it is a conductive polymer (PVDF insulates), thermally and chemically stable, and inexpensive [58]. Chen et al. studied the use of PANI in the cathode using lithium iron phosphate and reported that the capacity was increased by around 10% with the use of PANI, and capacity retention as much as doubled [59]. PANI has not, however, been extensively studied with silicon.

A self-healing polymer (SHP) is another potential candidate for a replacement binder because it would be able to recover from cracking during expansion and contraction. Instead of the active material breaking apart and losing electrical contact, an electrode made with a SHP would break apart but then be pulled back together by the polymer, which is able to repair its own hydrogen bonds repeatedly and autonomously, thereby healing cracks in the material layer. Wang et al. explored the use of a conducting SHP with silicon microparticles, finding that they could achieve a capacity exceeding 3000 mAh/g at low charging/discharging rates and a fairly stable 1400 mAh/g at C/2. These electrodes showed 75% capacity retention after 130 cycles at C/10. The material loading in this study, however, was too low for commercial applications, reported at under 1 mg/cm^2 [52].

Altering the chemistry of the electrolyte can also be advantageous, usually by promoting a more stable SEI layer. Two common electrolyte additives are vinylene carbonate (VC) and fluoroethelyne carbonate (FEC). VC has been shown to give an irreversible capacity increase of

more than 70% after 200 cycles when added to an ethylene carbonate/dimethyl carbonate (EC:DMC) based electrolyte in as small a quantity as 1% wt. The same researchers showed that this is due to a thin, stable SEI layer formation with the addition of VC. Cells using no VC formed an ever-thickening SEI layer which increased in impedance with every cycle, while the impedance of the cells with VC remained constant [60]. The same effect was observed by Etacheri et al. with the use of FEC: the impedance of cells using no additive was significantly higher after 30 cycles than those with FEC added to the EC:DMC electrolyte. Consequently, they found that the FEC cells retained over 70% more capacity than those without after 30 cycles [61].

Ref #	Publication Date	Particle Size	Structure	Loading	C-rate and Highest Capacity	Cycle Life
[39]	2011	Not specified	3D; Silicon decorated CNT posts	1 mg/cm^2	1958 mAh/g	Tested over 20 cycles; loss per cycle of .3%
[41]	2012	100 nm	"Yolk-shell" structure with carbon shell; applied as a slurry	not reported	630 mAh/g at 4C	Capacity retention after 500 cycles: 88%, 750 cycles 81%, 1000 cycles 74%
[62]	2008	N/A	Silicon Nanowires	not reported	2100 mAh/g at 1 C	"little fading" up to 10 cycles
[44]	2003	N/A	Silicon pillar array	N/A	260 μAh/cm^2	Not reported
[44]	2003	12 nm	Nanocrystalline silicon	not reported	2400 mAh/g	Capacity retention after 50 cycles: 50%, mean capacity loss 20 mAh/g per cycle
[44]	2003	film thickness 100 nm	Thin film	not reported	3500 mAh/g	Mean capacity loss 8 mAh/g per cycle
[40]	2009	tube diameter 200 nm	Silicon Nanotubes	10 mg/cm^2	2878 mAh/g at 5C	Capacity retention after 200 cycles: 89% (1C)

[48]	2010	50 nm	Hybrid Silicon/Carbon Nanotubes	not reported	~900 at 2.5C	Capacity fade for 1st 25 cycles: 0.15%/cycle, next 25 cycles 1.3%/cycle, next 50 cycles .4%/cycle
[47]	2010	21-22 nm	Silicon nanoparticle & graphene paper composite	not reported	2700 mAh/g	Capacity retention after 300 cycles: 50%
[42]	2012	N/A	Double walled Silicon nanotubes	.02-.1 mg/cm^2	940 mAh/g at 12C	Capacity retention after 6000 cycles at 10C: 88%
[49]	2011	Not specified	Si nanoparticles in a graphene sheet scaffold	not reported	1100 mAh/g at 8C	Capacity retention after 150 cycles: 83%
[61]	2012	N/a	Silicon Nanowires with FEC electrolyte additive	not reported	~2200 mAh/g at 1C	Capacity fade after 30 cycles: 4.5%
[46]	2008	20-50 nm	Carbon coated silicon nanoparticles	not reported	Reversible capacity: 1100 mAh/g	~50% capacity fade in first cycle, "no further" fade for 60 cycles
[57]	2007	325 mesh size	Crystalline silicon powder	1-2 mg/cm^2	Reversible capacity: 1100 mAh/g	Capacity retention after 80 cycles: ~60%
[52]	2013	micro	Silicon microparticles with SHP binder	0.5-0.7 mg/cm^2	1400 mAh/g at C/2	~75% capacity retention after 130 cycles at C/10

Table 2: Comparison of selected capacity fade mitigation strategies for silicon anodes

2.3.3 Nanoscale Materials

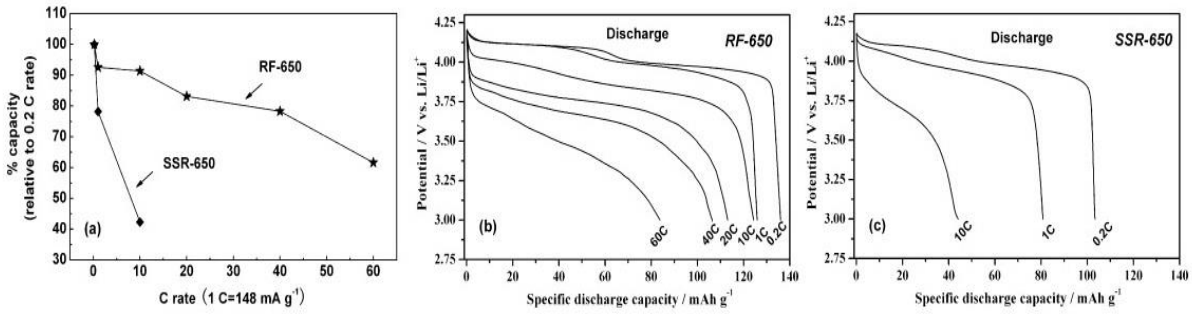

Figure 11: Comparison of cycling performance of nanoscale (RF-650) and microscale (SSR-650) LMO. (a) Rate capability of nanoscale LMO and microscale LMO. (b) Voltage versus capacity curves for nanoscale LMO. (c) Voltage versus capacity curves for microscale LMO. Figure Source: [63]

Commercial batteries currently rely mainly on micro-sized active material particles, however, as can be seen in Figure 11, nanoscale materials have a clear advantage over microscale. There are many reasons that reducing the particle size to the nanoscale results in better performance in lithium-ion batteries. One of the most important reasons is clearly represented in the following equation for lithium ion diffusion time:

$$\tau = \frac{L_{ion}^2}{D_{Li}}$$

Here, τ is the characteristic ion diffusion time, L_{ion} is the ion diffusion length, and D_{Li} is the ion diffusion coefficient, which is dependent on the material used. The diffusion time is proportional to the square of the ion diffusion length, and since nanomaterials have significantly smaller diffusion lengths due to the smaller particle size, this has a very large impact on the diffusion time. This improves both the power density and rate capability of the cell since lithium ions can be inserted and extracted faster than cells using microscale active material [16]. The decreased ion diffusion length of the nanoparticles also makes new ion storage sites accessible within the charging time, resulting in better utilization of the active material [64, 65].

Nanoparticles also have a large surface area to volume ratio as compared to micro or macroscale materials, and this enhanced surface area gives better contact between the electrolyte and the active material. This makes new interfacial ion storage sites more easily available, which further improves the material utilization, but also results in better rate capability and cycle life for the cell because the storage of lithium ions in surface sites is highly reversible [16].

Another major advantage of nanoscale materials is their structural integrity. It is much more difficult to crack or break apart nanoscale particles than micro- or bulk material. This results in better cycle life especially in the case of materials such as silicon, which expand considerably upon lithium insertion [16].

The use of nanomaterials also has its disadvantages. Due to the inherent porosity of nanomaterial layers, the packing density is low, making the volumetric energy and power densities low as well. In addition, the high surface area of nanoparticles, while in some ways an advantage as discussed above, also increases unwanted reactions with the electrolyte, such as the buildup of an overly-thick SEI layer. Another drawback is the manufacturing of nanomaterials. Many require complicated and costly synthesis procedures and require the use of hazardous materials. The nanomaterials themselves can also be a health hazard and many have not been thoroughly studied for long-term health and environmental impacts. Some of these disadvantages could be addressed using composite material electrodes. The packing density issue, for example, could be lessened by using both micro- and nanoparticles, wherein the nanoparticles would fill in the small gaps between the microparticles. Conductive carbon coating over the nanoparticles could mitigate the problem of detrimental surface interactions with the electrolyte, while still maintaining the ion storage enhancement provided by the extra surface area. Additionally, it would improve the conductivity of the electrode as a whole, since many electrode materials are insulating or semiconducting [16].

Nanomaterials exist in many forms, each of which can have advantages and disadvantages when used in an electrode. Some of these forms are shown in Figure 12. Nanoparticles (Figure 12 a) are the most common and easiest to fabricate. They offer all the advantages described above as well as being the least expensive due to their relative ease of manufacture. Another common form is nanowires (Figure 12 b), which offer an attractive morphology that does not tend to agglomerate, has a lower electronic resistance, and higher

packing density than plain nanoparticles. They are more complex to synthesize than particles, and the process has some limitations, however, they are a promising candidate for many battery applications [62]. Another structure is the hollow tube or sphere (Figure 12 c). One of the main attractions to this structure is an even shorter ion diffusion length than regular nanoparticles, resulting in excellent rate capability. Additionally, the hollow structure allows expansion into the inner void during charging, which eases mechanical strain on the electrode and leads to a more stable cycle life. This is especially important for materials such as silicon. The drawback to this design is again a more complicated and therefore more costly synthesis [41, 42, 66]. Another approach is to arrange particles into an ordered mesoporous structure (Figure 12 d). Mesoporous materials have short ionic transport lengths, high surface area for reversible lithium ion storage, and the ordered structure facilitates ionic movement well [67, 68].

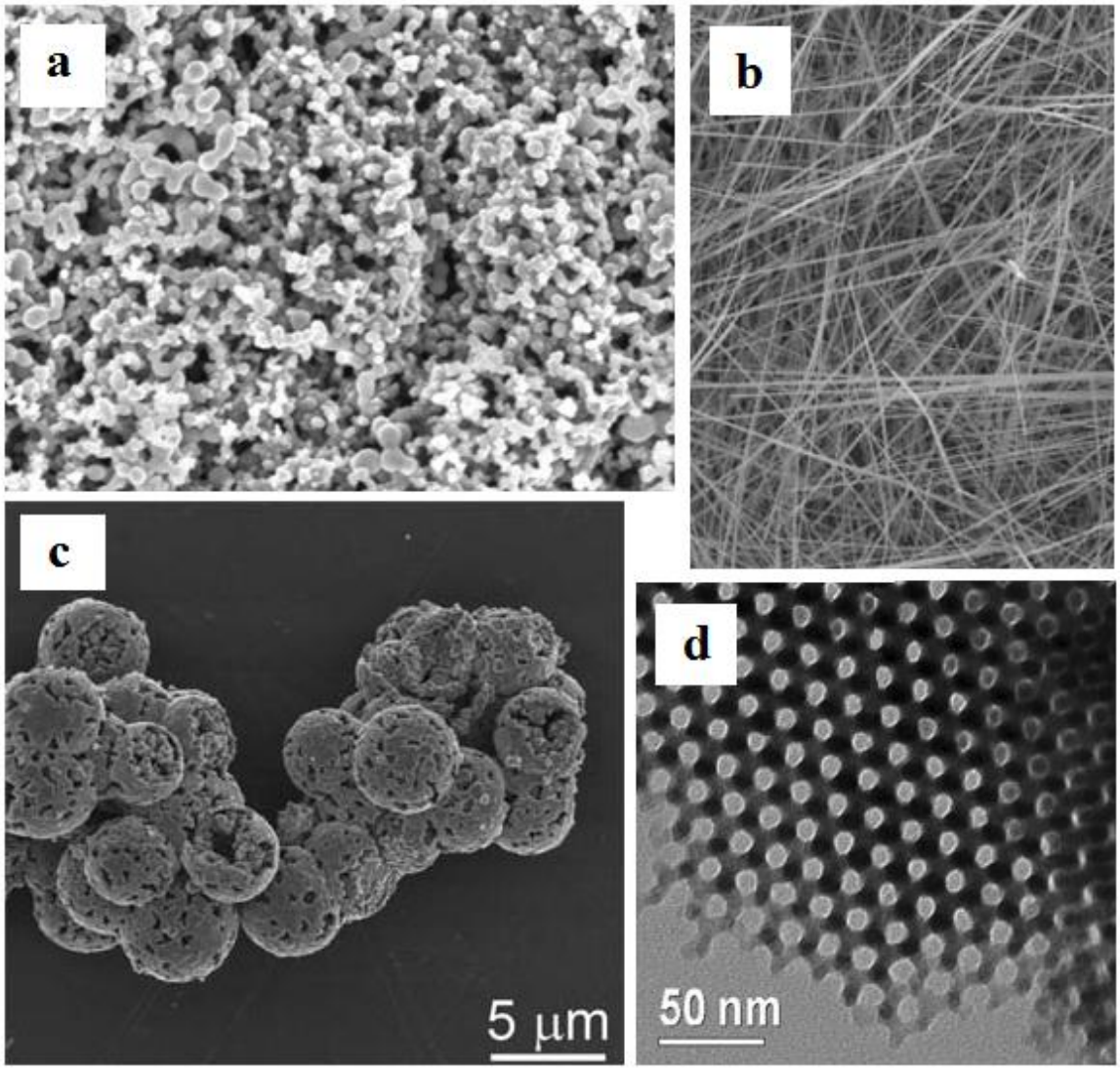

Figure 12: Nanomaterials: (a) nanoparticles, (b) nanowires, (c) hollow spheres, (d) mesoporous array. [Figure sources: (b) 47, (c) 44, (d) 45]

2.3.4 Carbon Nanotubes

Since their discovery in 1991, carbon nanotubes (CNTs) have garnered much attention due to their astounding physical, electrical, and thermal properties. A single wall nanotube (SWNT) can be visualized as a single sheet of graphene rolled into a seamless cylinder. Multiwall nanotubes (MWNT) consist of concentric SWNTs, spaced 0.34 nm apart and held together by Van der Waals forces [69, 70]. The hexagonal lattice of the graphene sheet can be oriented in

different ways, resulting in different nanotube structures. This is known as the chirality of the nanotube and can be described by the equation

$$\vec{C} = n\vec{a}_1 + m\vec{a}_2$$

where C is the chirality vector, n and m are integer steps along the carbon bonds of the graphene, and a_1 and a_2 are the basis vectors of the graphene structure as shown in Figure 12. Two special cases exist, known as armchair and zigzag nanotubes. These are illustrated in Figure 13. Armchair nanotubes occur when m = n, and zigzag occur when m = 0 [70].

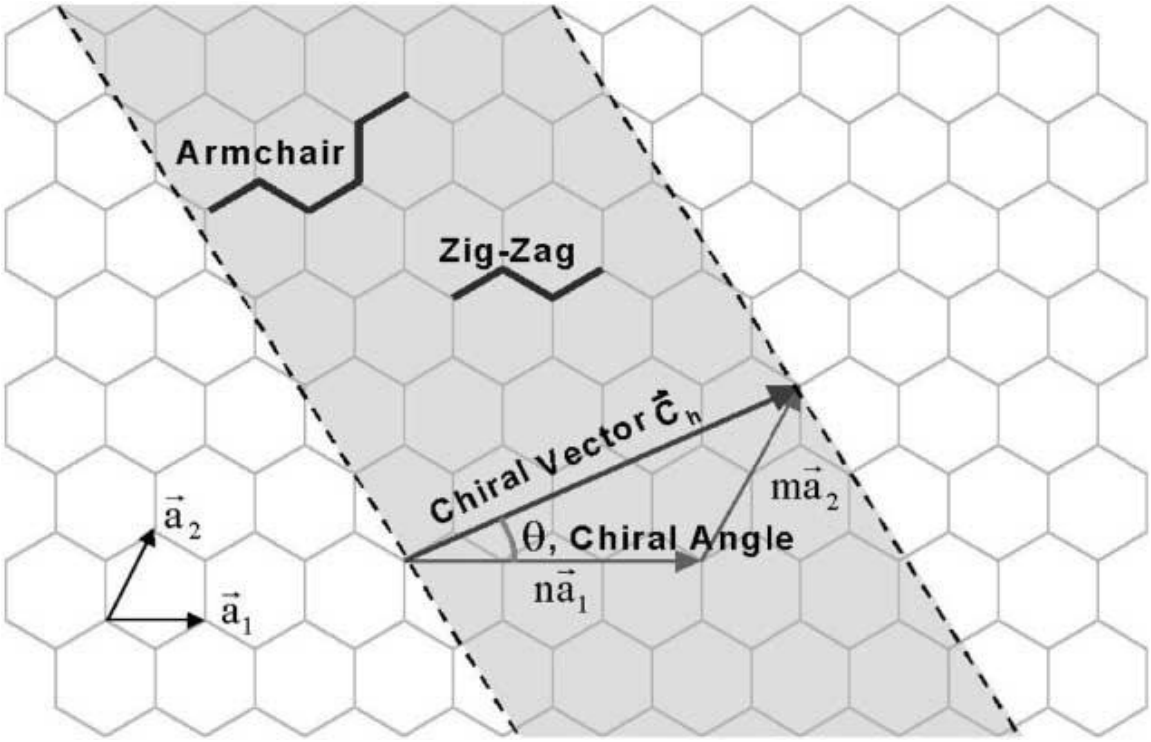

Figure 12: Schematic of carbon nanotube chirality. Figure source: [70]

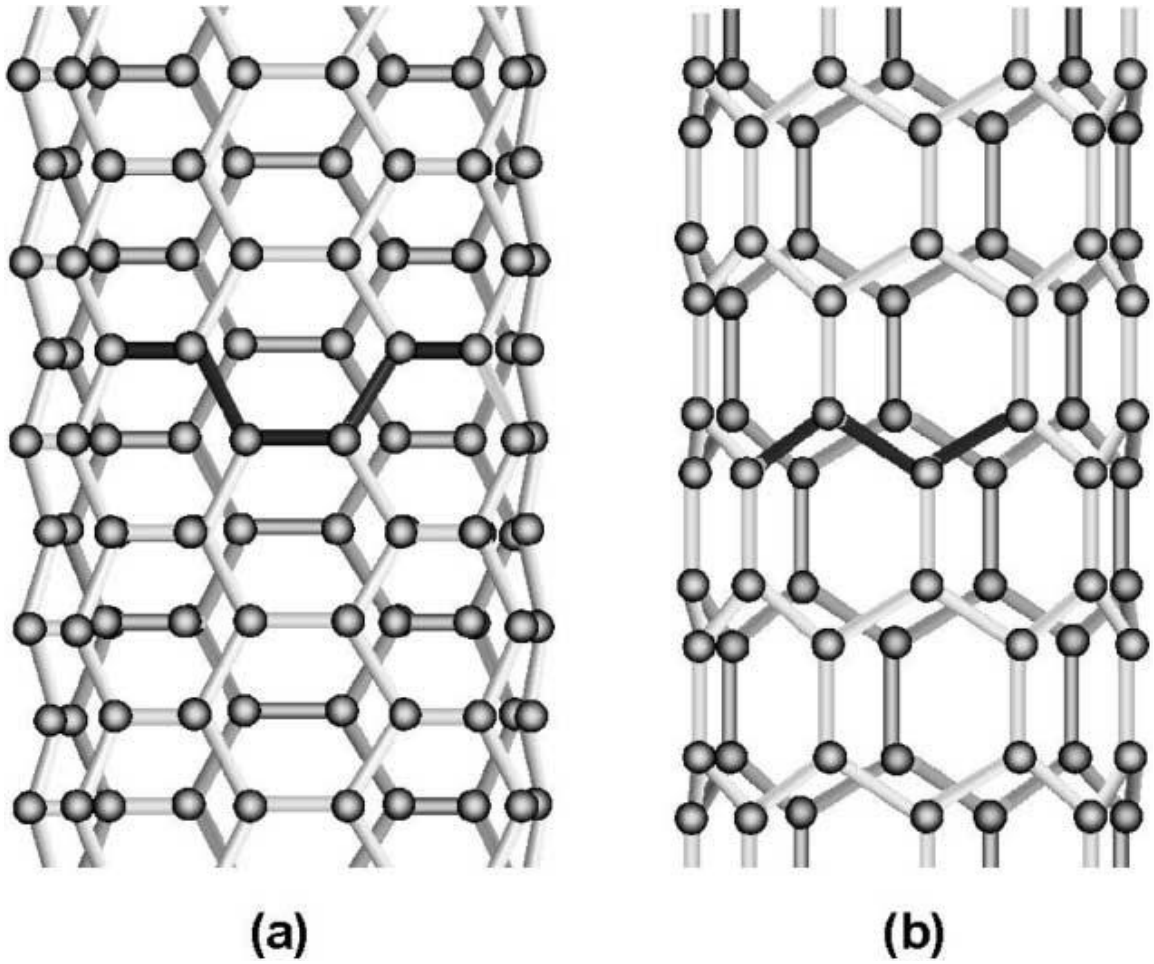

Figure 13: Structure of (a) an armchair carbon nanotube and (b) a zigzag carbon nanotube. Figure source: [70]

The chirality of a carbon nanotube plays an important role in its electrical properties. CNTs can exhibit either metallic or semiconducting properties. A metallic CNT must satisfy the relationship

$$|n - m| = 3I$$

where I is an integer. If this relationship is not satisfied, the CNT will be semiconducting. Because MWNTs can have layers of different chirality, their properties are not so easily categorized, however, they will usually exhibit metallic behavior [71]. The electrical conductivity of CNTs is one of the most appealing traits for their use in batteries. Measurements of electrical conductivity of CNTs have exceeded 5×10^5 S/m, at least an order of magnitude higher than most conventional conductive additives such as carbon black. In addition, the high aspect ratio of

CNTs (on average, greater than 10,000) allows the same conductivity to be obtained with an order of magnitude less mass, because the CNTs can create a much longer range percolation network. Less mass wasted on conductive additive yields higher gravimetric capacity, power density, and energy density. Some studies have shown an improvement of three times the capacity for composite anodes using CNTs versus carbon black [72].

CNTs are also known for their mechanical strength. Papers made from SWNTs exhibit a tensile strength of 80-100 MPa and a Young's modulus of 5-10 GPa [72]. With these properties, a free-standing electrode can be fabricated that would withstand harsh deformations without any permanent damage. Such electrodes are of great interest in the creation of flexible batteries, and also because a free-standing electrode eliminates the weight and volume of the substrate.

The thermal properties of CNTs could also be an asset for batteries because they could allow batteries to operate with greater safety at a wider temperature range, and also allow for higher power applications. Hone et al. measured the thermal conductivity of SWNTs as 1750-5800 W/m-K [73], and Yang et al. measured 200 W/m-K for MWNTs [74]. There are large variations in measurements for thermal conductivities of CNTs due to different methods of synthesis and measurement, however, all results agree that CNTs are comparable in thermal conductivity to graphite or diamond. It has also been reported that at higher temperatures, CNT conductivity exceeds that of diamond and graphite[73].

In addition to their excellent properties as a conductive additive for lithium ion batteries, CNTs themselves can intercalate lithium ions and can be used as an anode material, with the main intercalation plateau occurring at a potential of about 1 V. However, CNTs show a large irreversible capacity in the first cycle due to over-formation of the SEI layer caused by the high surface area of the CNTs. This can be slightly improved with electrolyte additives similar to the ones discussed previously. Despite the large irreversible capacity in the first cycle, reversible capacities approaching 1000 mAh/g have been reported, almost three times that of graphite, as shown in Figure 14 [72].

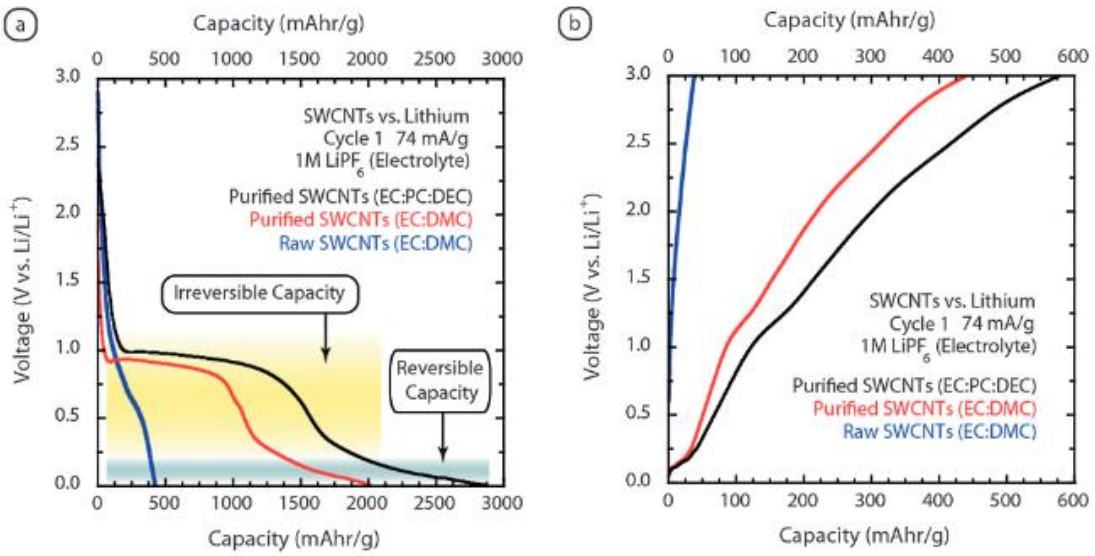

Figure 14: Cycling of SWNTs as an anode material. (a) Charge capacity (b) Discharge capacity. Figure source: [72]

2.4 Electrode Architectures

The way in which the material is arranged within an electrode can have a large impact on a battery's performance. Battery architectures can be classified into three categories based on dimensionality: 1D, 2D, and 3D. One dimensional designs are the simplest in concept: a single layer of active material applied to a current collector for each electrode. The material within this layer can be arranged in a three dimensional manner, such as vertically aligned posts, but they still take on a parallel plate design. Although limited in total active material loading and therefore in capacity, 1D architectures do have value: electron transport is very direct since there is no complicated network of material to navigate through. Many 1D designs are also very physically robust due to their uncomplicated nature, although this is not necessarily true: the aforementioned vertically aligned posts, for example, are more vulnerable than a film.

Two dimensional designs consist of some kind of layered structure or scaffolding on which the active material is deposited. Generally this scaffold is made up of a conducting material such as carbon to enhance the electrical conductivity within the electrode. 2D designs maintain the mechanical robustness of 1D electrodes while allowing for higher active material loading within the same footprint area [75].

Three dimensional architectures integrate the cathode and anode materials within the cell such that the distances between them remain very small, which keeps ion transport time short, yet the maximum amount of material is included within the allowed footprint. Examples of 3D cell arrangements are shown in Figure 15. The major advantage of these configurations is that energy density is increased due to the amount of material present but power density is not sacrificed because of the small separation between the anode and cathode. The main disadvantage of 3D architectures is manufacturing methods: currently there is no way to produce 3D cells cost-effectively on a large scale, which limits commercialization [76-78].

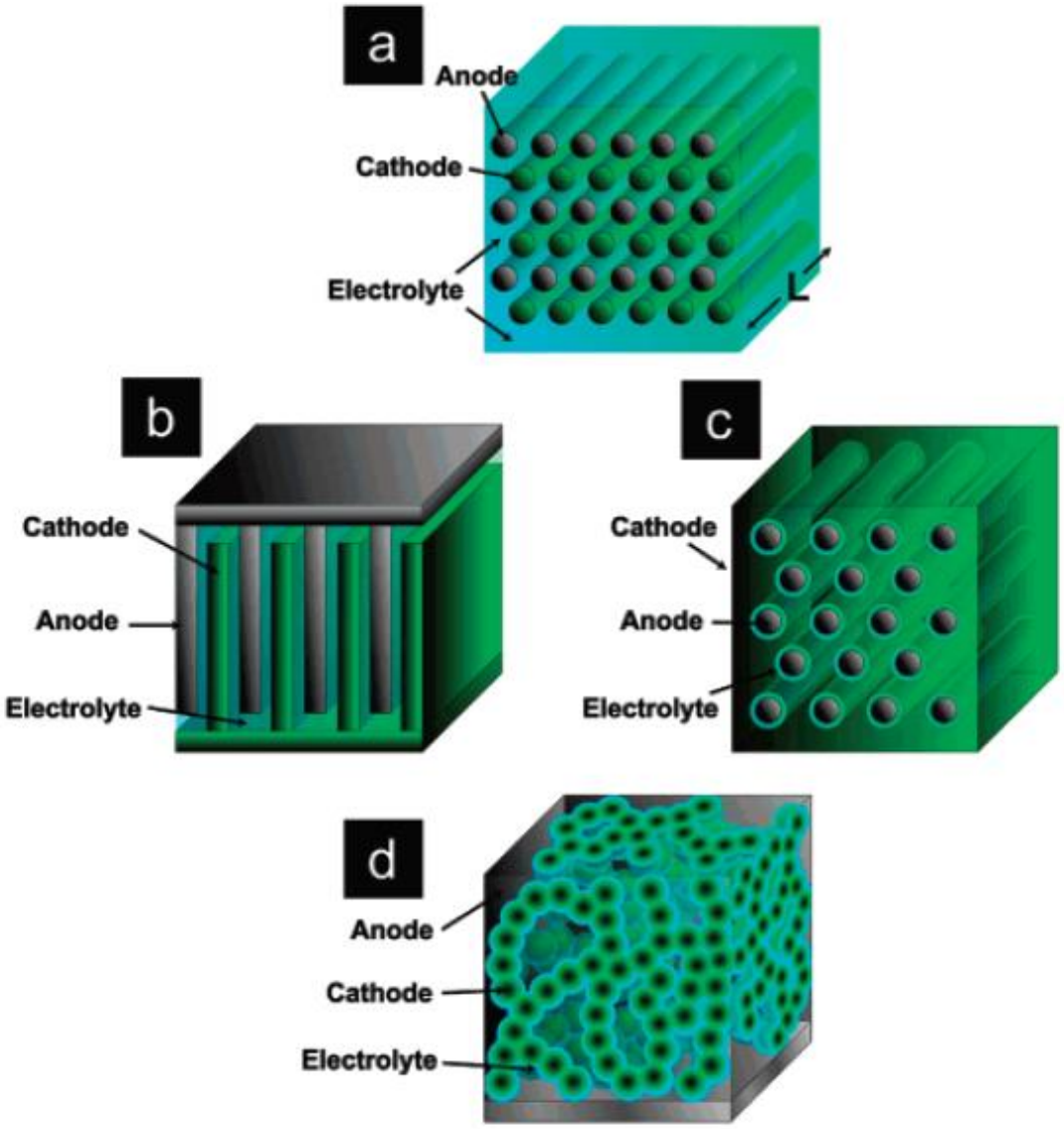

Figure 15: Examples of 3D architectures: (a) Interdigitated rods, (b) Interdigitated plates, (c) Anode rod array coated with thin electrolyte layer and surrounded by cathode material, (d) "sponge" architecture with electrolyte-coated cathode particle network surrounded by anode material. Figure source: [77]

3. Layer-by-Layer Electrode Arcitechture

3.1 The Layer-by-Layer Advantage

In this project, we used a two dimensional architecture consisting of alternating layers of active material and carbon nanotubes. The two dimensional architecture is simple, inexpensive to fabricate, compatible with current manufacturing techniques, and the concept can be applied to any battery chemistry for enhancement. Another advantage of the 2D structure is mechanical robustness; the simple flat design can withstand pressure and physical agitation without losing electrical conductivity or shorting. The carbon nanotube layers enhance the surface area of the electrode without having to increase the footprint, and also do not significantly contribute to the overall volume of the cell, unlike a stacked electrode structure which would waste significant space on extra layers of substrate. Calculations indicate that an approximately 30% increase in surface area can be achieved using a ten layer electrode with 85% active material loading versus a standard fabrication method. This surface area enhancement continues to increase linearly as the number of layers increases, such that the surface area can be doubled (100% surface area enhancement) with approximately 30 layers of CNTs. The CNTs also create a conductive network through the active material layer, allowing for efficient ion transport and ensuring maximum contact between the active material particles and the current collecting substrate so that full contribution of the active material is attained. This increase in ion transport efficiency allows for higher rate charging and higher power density.

3.2 Fabrication Procedure

Figure 16 is a schematic of the basic assembly process for a multi-layer electrode, in this case an anode. We begin with the current collecting substrate; copper for the anode and aluminum for the cathode. The surface is then treated to remove the native oxide layer and make the surface hydrophilic to ensure even material deposition. This treatment consists of first roughening the surface with sandpaper, then cleaning with acetone and isopropyl alcohol (IPA). The first multiwalled carbon nanotube (MWNT) layer is then deposited on the surface,

followed by a layer of the active material. This is repeated until the desired number of layers is achieved, followed by a final layer of MWNTs to ensure that all particles are connected to the CNT network.

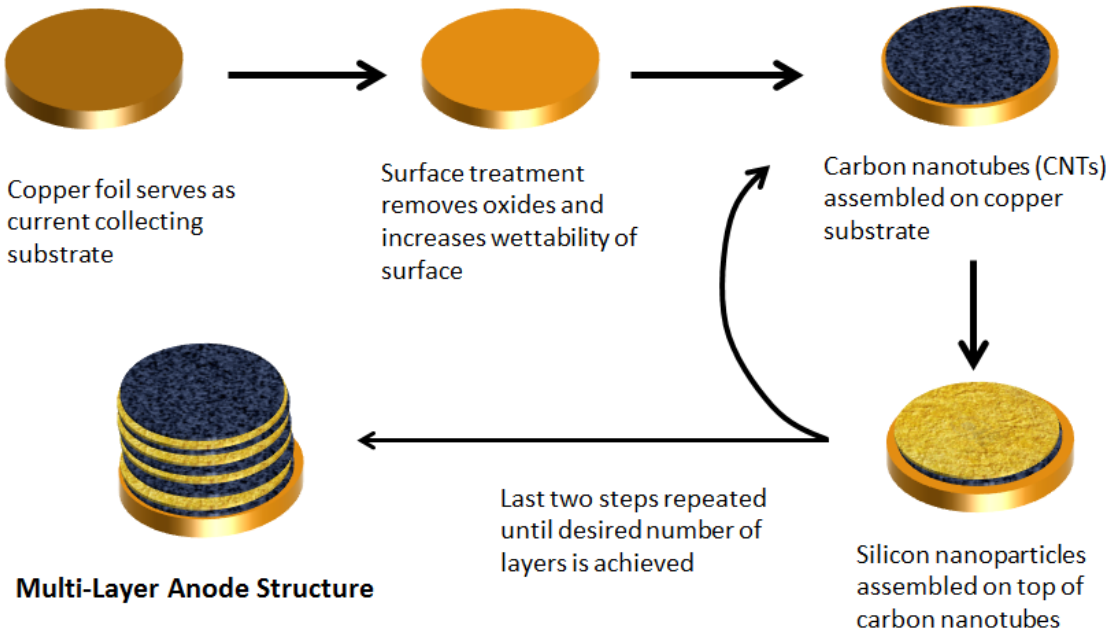

Figure 16: Fabrication process for multi-layer electrodes (shown here specifically for the anode)

After the multi-walled electrode has been made, it is then baked overnight at 80°C to remove any remaining moisture. Next it is pressed in a hydraulic press at 5000 psi to ensure good contact between the layers. Finally, it is made into a half-cell ready for electrochemical testing.

There are several different methods that can be employed to make the multi-layer structure. The doctor blade technique is similar to current manufacturing techniques and yields an even coating of adjustable thickness. Spin casting creates consistent, thin layers in which particle size is very uniform since larger particles and agglomerates tend to be spun off the surface. Spray casting is the fastest technique for creating the multi-layer structure, and can also be readily adapted to current manufacturing techniques.

3.2.1 Doctor Blade

Of the three material deposition methods explored, the doctor blade technique is most similar to conventional calendaring methods used in the battery industry. As shown in Figure 17, a viscous slurry (consisting of active material particles, conductive additive, and binder in solvent) is pipetted onto the surface of the substrate in a tooth-shaped puddle to ensure the sides receive even coating. The doctor blade is adjusted to the desired height, and then the flat blade is passed over the substrate, spreading the slurry into a uniform coating.

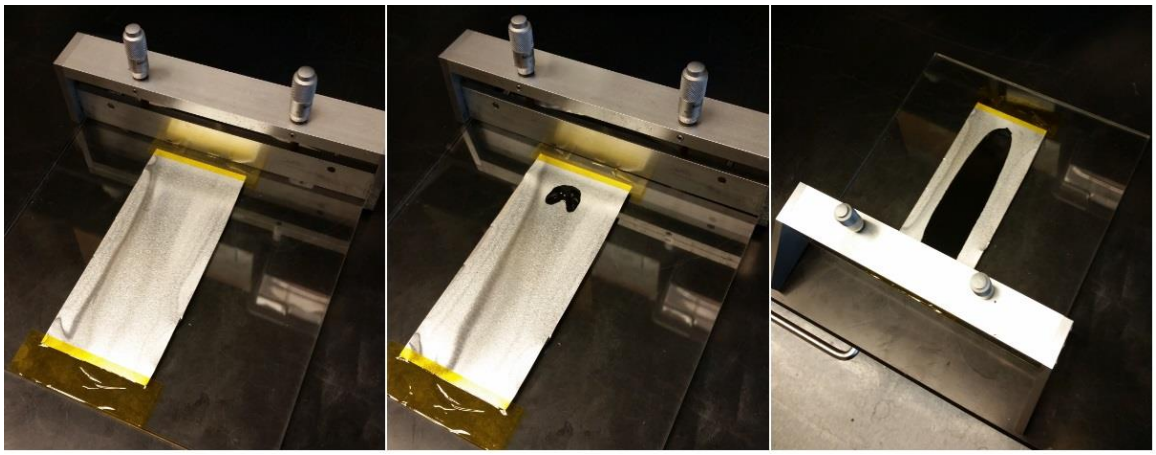

Figure 17: Steps of the doctor blade fabrication process

A study of the loading and thickness was conducted on electrodes made using this technique to investigate the uniformity and density of the active material layer. Tables 3 and 4 show the thicknesses and loadings, respectively, for 10 standard fabrication (no CNT layers) cathodes with a slurry composition of lithium manganese oxide (LMO), carbon black (CB), and polyvinylidene fluoride (PVDF) with a weight ratio of 85:10:5 (LMO:CB:PVDF). The solvent used was N-methyl-2-pyrollidone (NMP), and was mixed with the active material powder at a weight ratio of 1:1. Thickness measurements were made with a micrometer of 1 micron resolution, and mass measurements made with a microbalance set to a resolution of 0.01 mg. When making the thickness measurements, the sample was sandwiched between two sheets of weigh paper to avoid direct contact with the micrometer and the material, so this thickness was subtracted off of the total, along with the thickness of the aluminum substrate to obtain the thickness of

only the LMO layer. The measurements for the weigh paper can also be found in Table 3. The mass of the aluminum was also subtracted from the total mass of the electrode, and then this number was multiplied by the 85% LMO content in order to obtain the LMO loadings shown in Table 4. As can be seen from this data, the standard deviations for both the thickness and mass of the active material layer are comparable to those of the aluminum and weigh paper, indicating that the coating is very even and uniform. The density calculated from the average values is somewhat low, however, at 0.07 mg/µm compared to commercially available electrodes with a density of approximately 0.18 mg/µm [79].

Sample #	Weigh Paper	Aluminum	Active Material Layer
1	70	75	22
2	69	77	26
3	73	79	24
4	73	79	25
5	71	75	28
6	68	75	27
7	72	76	26
8	70	76	28
9	68	75	27
10	71	79	26
Average	**71**	**77**	**26**
Standard Deviation	**1.8**	**1.7**	**1.8**

Table 3: Thicknesses in microns for standard fabrication LMO cathodes made using the doctor blade technique, along with thicknesses of the aluminum substrate and weigh paper used in measurements. The active material layer is composed of LMO, CB, and PVDF in weight ratios of 85:10:5.

Sample #	Aluminum	Active Material Layer
1	20.49	1.53
2	20.56	1.69
3	20.84	1.47
4	20.81	1.70
5	20.81	1.86
6	20.79	1.87
7	20.82	1.86
8	20.81	1.84
9	20.80	1.59
10	20.83	1.79
Average	**20.76**	**1.72**
Standard Deviation	**0.12**	**0.14**

Table 4: Loadings in mg/cm^2 for standard fabrication LMO cathodes made using the doctor blade technique, along with mass of the aluminum substrate. The active material layer is composed of LMO, CB, and PVDF in weight ratios of 85:10:5.

The carbon black is the least dense material included in the slurry, so to determine if reducing the carbon black content would increase the density, electrodes were fabricated with a composition of 90:5:5 (LMO:CB:PVDF). Results are shown in Table 5. From this data, it does not appear that decreasing the carbon black content had a positive effect on the density, since the loadings are similar but the thickness of the 90:5:5 ratio electrodes is consistently higher, even if by only a few microns.

	Thickness		Loading	
Sample #	**85:10:5**	**90:5:5**	**85:10:5**	**90:5:5**
1	26	35	1.53	1.81
2	29	35	1.70	1.13
3	27	39	1.48	2.02
4	27	38	1.70	1.90
5	31	34	1.86	1.84
6	29	32	1.88	1.64
7	26	33	1.86	1.61
8	28	31	1.84	1.51
9	29	37	1.59	1.71
10	30	32	1.79	1.69
Average	29	35	1.72	1.69
Standard Deviation	1.6	2.6	0.14	0.23

Table 5: Thickness (µm) and loading (mg/cm^2) measurements for two active material slurry compositions: 85:10:5 and 90:5:5 (LMO:CB:PVDF).

The previous experiment was repeated but with the doctor blade set higher, to see if the same results would apply with a thicker layer. These results are shown in Table 6, and also graphed in Figure 18. As can be seen from these measurements, increasing the thickness of the layer also resulted in a denser layer, as the thinner layers had a density of 0.06 mg/µm and 0.05 mg/µm for the 85:10:5 and 90:5:5 electrodes respectively, but the electrodes with a thicker layer both had an average density of 0.11 mg/µm, approaching the value for the commercially available electrode mentioned above.

	Thickness		Loading	
Sample #	**85:10:5**	**90:5:5**	**85:10:5**	**90:5:5**
1	67	110	7.61	10.98
2	109	107	10.95	10.97
3	99	79	11.23	10.10
4	72	100	8.81	10.20
5	82	94	8.59	11.12
Average	86	98	9.44	10.67
Standard Deviation	15.9	11.0	1.41	0.43

Table 6: Thickness (µm) and loading (mg/cm^2) measurements for two active material slurry compositions: 85:10:5 and 90:5:5 (LMO:CB:PVDF), doctor blade set higher.

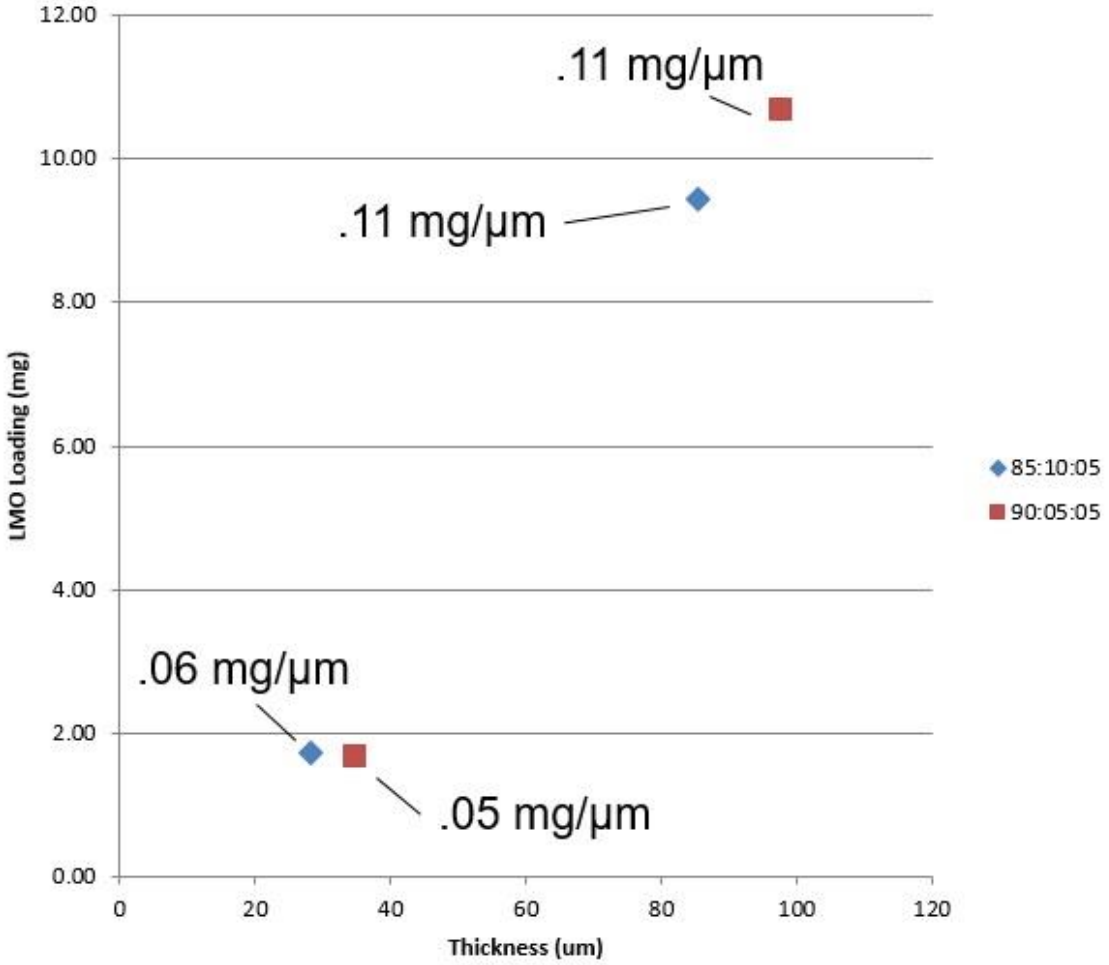

Figure 18: Average loading versus thickness for two slurry compositions and two height settings on the doctor blade.

Table 6 also shows that as the thickness of the layer increases, so does the standard deviation in the measurements, indicating that the surface roughness increases with the thickness. Because of this, the doctor blade technique is ill-suited to the fabrication of multi-layer electrodes, since increasing the number of layers would create increasingly non-uniform layers, and can sometimes remove material from underlying layers. Previous research done at the CHN has shown that as the number of layers increases, the capacity of the cells decreases; this can be seen in Figure 19 [17]. The doctor blade technique was used, however, for making standard fabrication electrodes to compare to layered electrodes made by spin or spray casting.

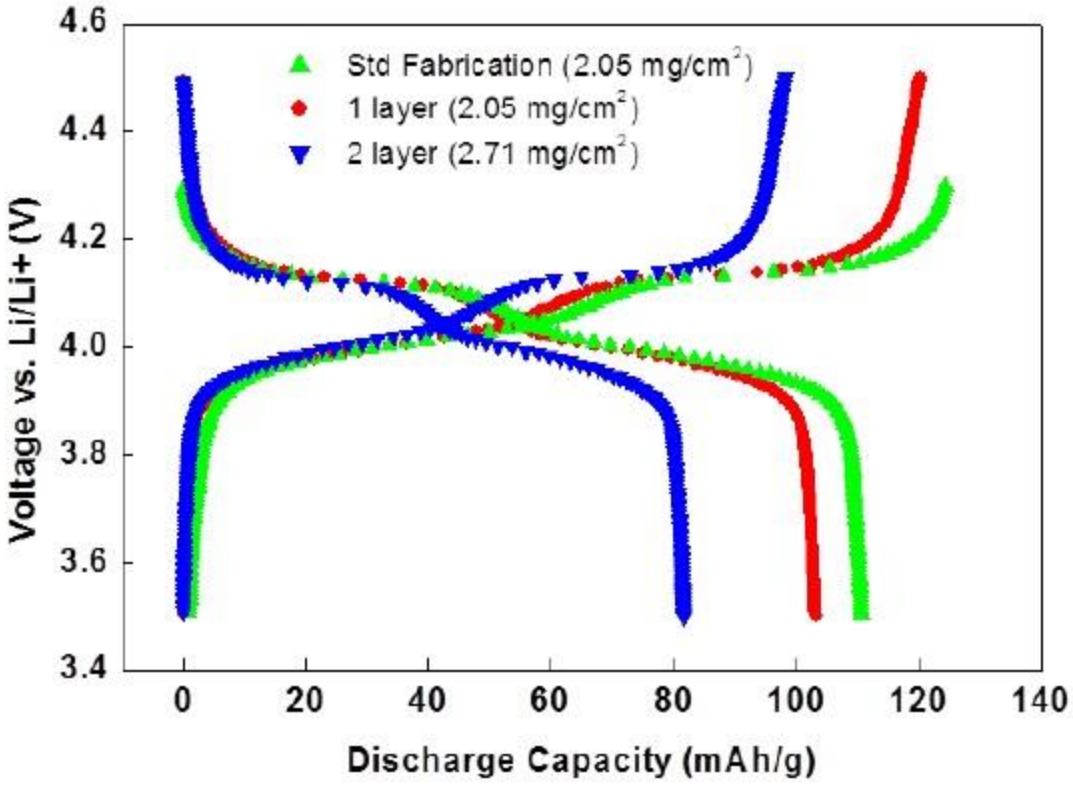

Figure 19: Cycling performance of standard and multi-layered electrodes fabricated using the doctor blade technique. Figure source: [17]

3.2.2 Spin Casting

In the spin casting process, both the MWNT layers and the active material layers are applied using a spin coating machine. After the surface treatment, a suspension of MWNTs in NMP solvent is pipetted onto the substrate. The substrate is then spun at increasing RPM, up to 4000 RPM, shedding excess solvent and material to leave a uniform coating of MWNTs. The electrode is then heated on a hot plate at 100°C to evaporate any remaining solvent, leaving behind only the MWNT layer. To obtain the desired MWNT loading, this must be repeated several times before moving on to the active material layer step. Once the MWNT coating is satisfactory, the active material slurry is pipetted on top of the CNT layer. This slurry contains a mixture of active material particles (e.g. LMO particles for the cathode, silicon particles for the

anode), polyvinylidene fluoride (PVDF) binder, and carbon black (CB) conductive additive, all suspended in NMP to make an ink-like slurry. The same process of spinning and heating is repeated until the desired loading is attained.

Although this method is consistent because it is precisely controlled and yields desirably thin layers, it has several disadvantages. The first is the time it takes to produce a single electrode. The spin program takes approximately two minutes. Each layer requires running this program several times to get full coverage of the electrode, which means creating just a single active material layer sandwiched between two CNT layers can take over 20 minutes. Another drawback is the uniformity of the coverage. Unless the substrate is perfectly centered in the spinner every time, there will be an unevenness in the coating. The spinner is also only capable of making a circular coating pattern, which makes spinning an impractical method for fabricating rectangular or irregular shaped electrodes. Lastly, spin casting is not scalable. Only one electrode can be made at a time, which is not acceptable for commercialization.

3.2.3 Spray Casting

The spray casting process follows the same general procedure outlined in Figure 16. After the surface treatment, the electrode is taped to a heated glass panel and propped nearly vertically. A suspension of MWNTs in IPA is then sprayed onto the surface using an airbrush. The IPA evaporates very quickly because of the heated plate, and the active material layer may be immediately applied without any intermediate heating step. The active material solution contains the same ingredients as that used in the spin casting process, but is suspended in IPA and diluted more to prevent blockage of the airbrush nozzle. Figure 20 shows the spray casting setup. Each layer (either CNT or active material) takes approximately five minutes to apply. At this rate, a single layer of active material between two CNT layers takes about 15 minutes. This is less time than the spin casting, and the 3” x 3” substrate can yield over 40 electrodes, whereas spin casting yields only one at a time. After the electrode is made, the same procedure of baking and pressing is followed before constructing the cell.

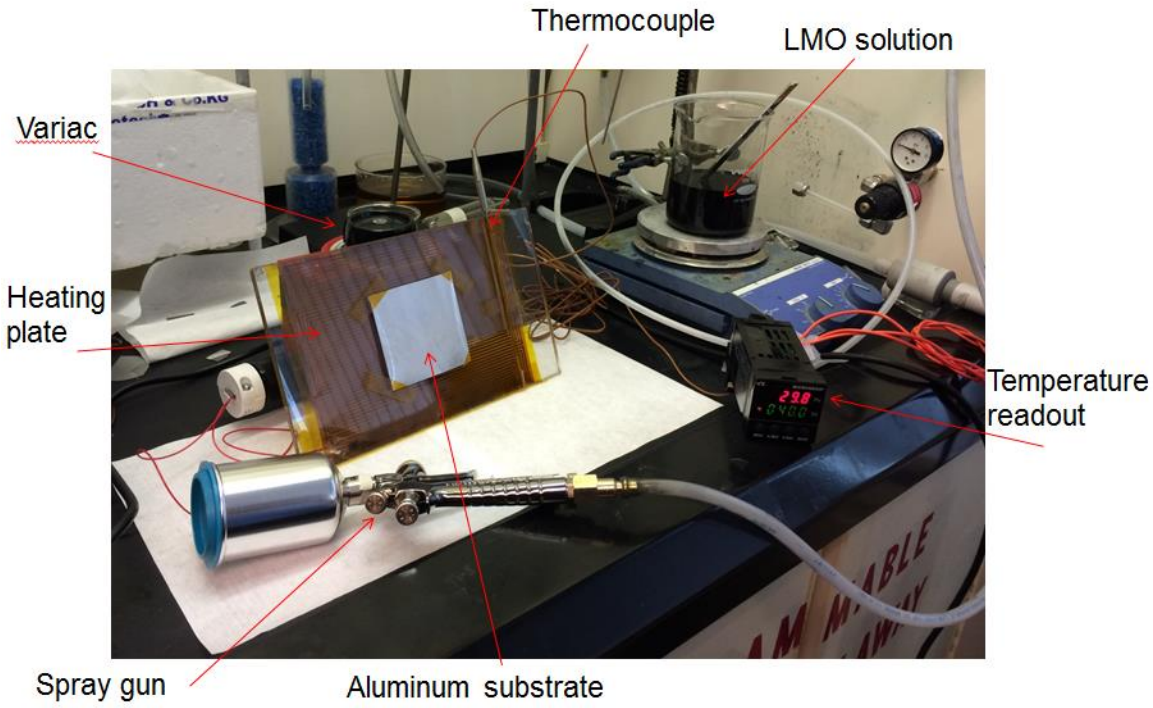

Figure 20: Spray casting setup

Figure 21a is a comparison of spray cast (left) and spin cast (right) electrodes. From this, it can be seen that spray casting yields a more uniform electrode. The dark patches on the spin cast electrode are areas of high carbon black content, indicating that during spinning, the carbon particles and silicon particles tend to separate, which is likely to give a less conductive electrode. Figure 21b shows the uniformity that can be achieved on a spray cast LMO cathode.

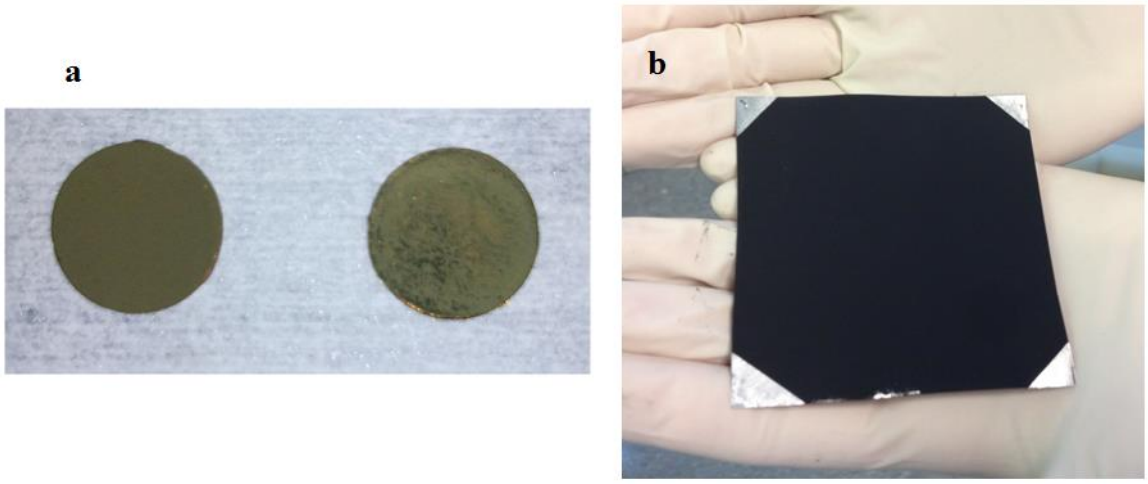

Figure 21: (a) Comparison of spray cast (left) and spin cast (right) silicon anodes, (b) LMO spray cast cathode

Figure 22 shows an SEM comparison of spray cast (a) and spin cast (b) silicon anodes. Both are taken at 10,000 times magnification. The spray cast electrode shows many more large particles, which is to be expected since large particles tend to be flung off the substrate during spinning, leaving only the smallest particles behind, however this does not seem to have any impact on cycling performance.

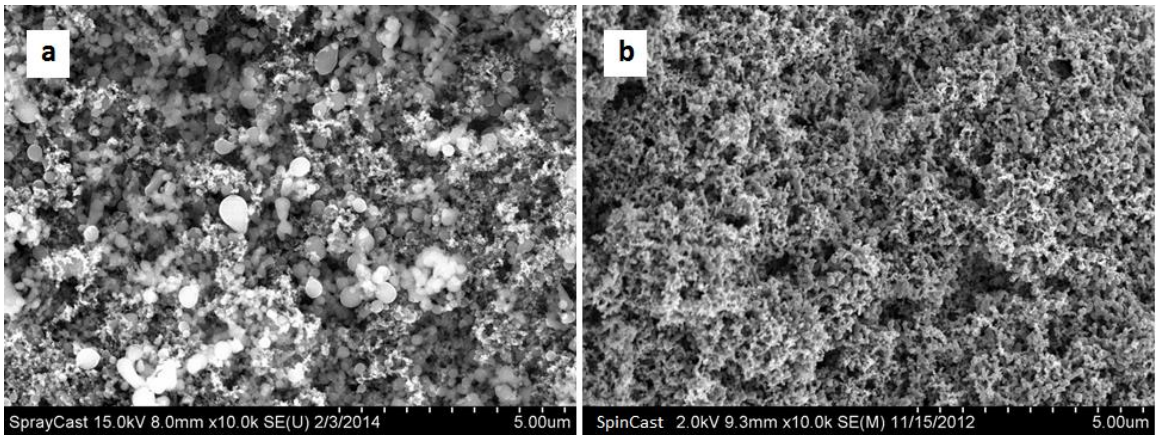

Figure 22: SEM comparison of spray cast (a) and spin cast (b) silicon anodes

To quantitatively determine the uniformity of the spray cast electrodes, several 3”x3” electrodes were fabricated and then circular samples of area 1 cm^2 were cut from each corner

and the center and the loading for each of those measured. The sample locations were consistently numbered as shown in Figure 23 so that any trends in loading could be identified. Four electrodes could be prepared from one 500 mL beaker of active material solution, and the order in which those electrodes were fabricated was recorded to see if the concentration of the solution changes as it gets used. Lastly, two beakers, labelled A and B, were used (for a total of eight electrodes) to increase sample size. Results are shown in Table 7. The overall standard deviation for all samples was 0.17, comparable to that of the doctor blade samples previously discussed, therefore it can be concluded that the spray casting technique yields a similarly uniform coating. From the data in Table 7, it can be seen that there is no consistent trend in loading versus fabrication order between the two beakers. There may be a slight tendency for sample locations 3 and 4 to have marginally higher loading. Since they are located at the bottom, there may be a little bit of liquid flow in that direction before it evaporates, however this effect is not very pronounced, with a maximum discrepancy of only 0.21 mg.

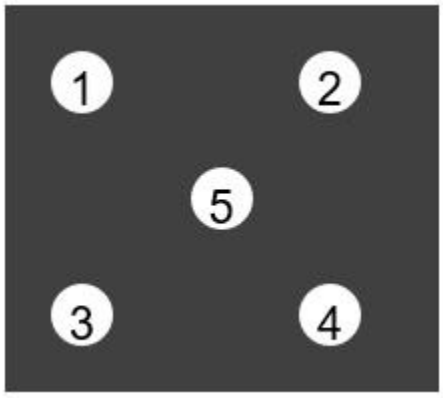

Figure 23: Schematic of sample locations for spray casting uniformity study

Beaker	A				B				
Fabrication Order	1st	2nd	3rd	4th	1st	2nd	3rd	4th	Average
Sample 1	0.35	1.11	1.33	1.19	0.90	1.02	1.05	0.76	0.96
Sample 2	0.67	1.11	1.32	1.28	1.15	0.45	1.05	0.77	0.98
Sample 3	1.02	1.12	1.67	1.56	0.92	1.00	1.19	0.85	1.17
Sample 4	0.91	0.93	1.09	1.04	1.10	1.72	0.95	0.96	1.09
Sample 5	0.62	1.37	0.69	1.06	0.82	0.93	1.35	0.82	0.96
Average	0.71	1.13	1.22	1.23	0.98	1.02	1.12	0.83	

Table 7: Loading (mg) data for spray casting uniformity study. The active material layer is composed of LMO, carbon black, and PVDF in weight ratios of 85:10:5, and the solvent is IPA.

There are several variables in the spray casting setup, and these were investigated to determine their effect on the loading of the resulting electrode: plate angle, plate temperature, solution concentration, and solvent used. In investigating the plate angle, a similar experiment to the previous uniformity study was conducted, with samples taken from a large 3”x3” electrode taken in the same locations as shown in Figure 23. The plate was propped at 30°, 45°, 60°, and 85° relative to the table, and two electrodes were fabricated at each angle. Figure 24 shows the average loading for each electrode versus plate angle. From the graph, it can be seen there is no discernable trend in loading versus plate angle.

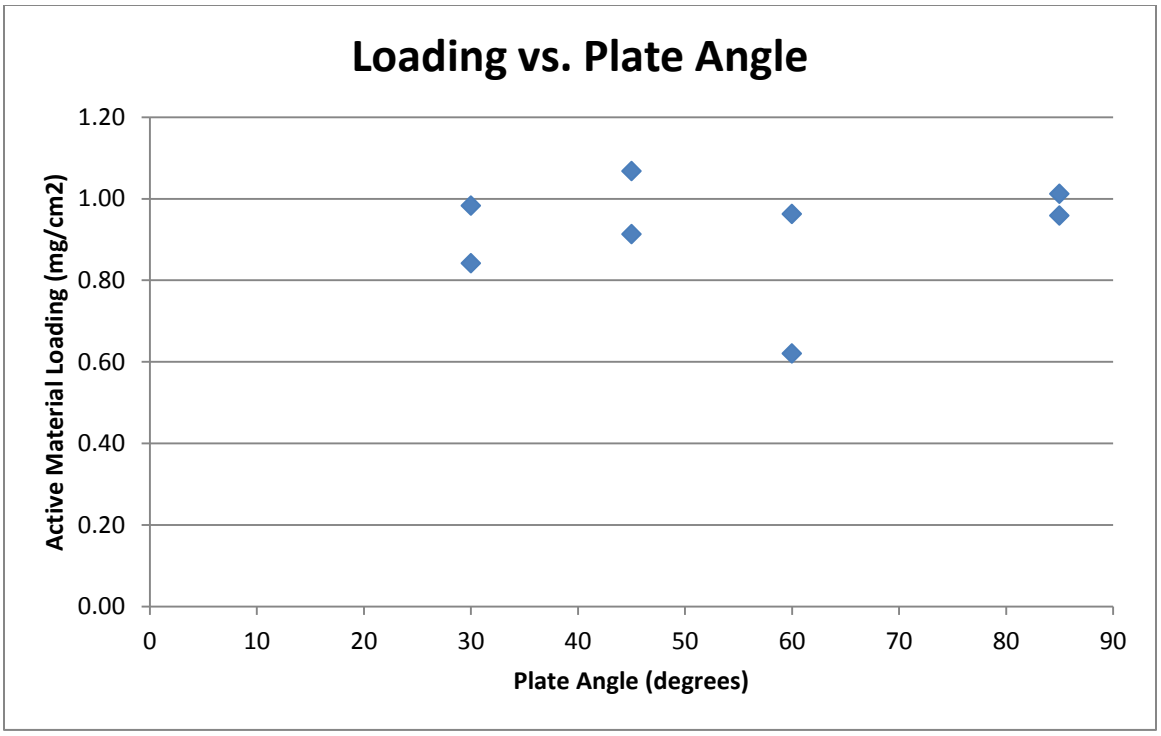

Figure 24: Loading versus plate angle for spray cast electrodes. The active material layer is composed of LMO, carbon black, and PVDF in weight ratios of 85:10:5, and the solvent is IPA. The concentration of the solution is 6.67 mg/mL, and the temperature of the plate is 60°C.

A nearly identical experiment was conducted to investigate plate temperature. Here, the plate angle was kept at 85°, and the temperature of the plate varied from 30° C to 75° C. The results, shown in Figure 25, indicate that there is no consistent trend as the temperature is varied either.

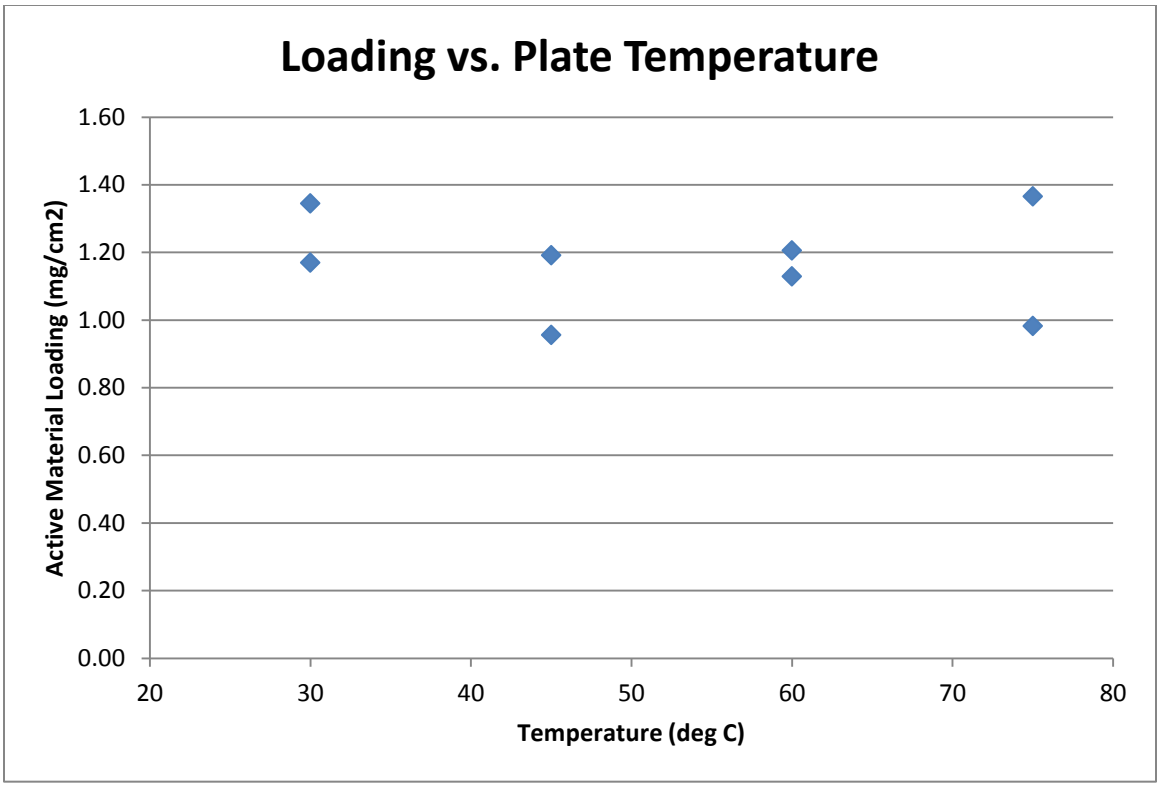

Figure 25: Loading versus plate temperature for spray cast electrodes. The active material layer is composed of LMO, carbon black, and PVDF in weight ratios of 85:10:5, and the solvent is IPA. The concentration of the solution is 6.67 mg/mL, and the angle of the plate is 85°.

The experiment was repeated again, this time holding angle and temperature constant, and varying the concentration of the active material powder mixture in the solvent. Concentrations of 6.67 mg/mL, 10 mg/mL, and 13.33 mg/mL were tested, and results displayed in Figure 26. As would be expected, the loading increases linearly as the solution concentration increases. It does not, however, increase with a 1:1 relationship. The loading increases at a rate of approximately 0.14 mg/cm^2 per 1 mg/mL increase in concentration. This is because much of the material is lost in the spray casting process, some into the air, and some because the solution is sprayed off the edges of the substrate to ensure even coating over the whole area.

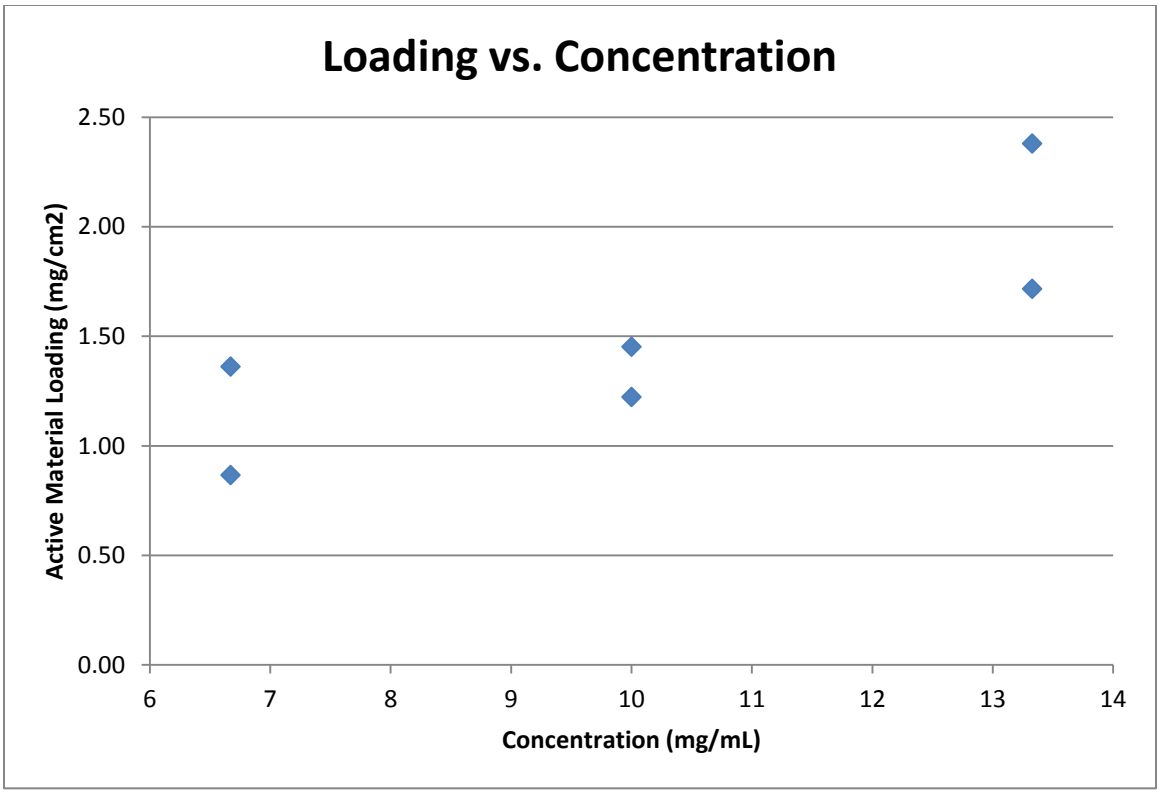

Figure 26: Loading versus solution concentration for spray cast electrodes. The active material layer is composed of LMO, carbon black, and PVDF in weight ratios of 85:10:5, and the solvent is IPA. The angle of the plate is 85° and the temperature is 60°C.

All of the experiments discussed so far have utilized IPA as the solvent, however, IPA does contain some water, which can be detrimental to battery performance. In addition, IPA does not yield the most stable suspension of CNTs. NMP has been shown to produce the best dispersion for CNTs [80], and this is confirmed by the zeta potential results shown in Figure 27. A good, stable dispersion will have a more extreme (in this case, lower negative) zeta potential, and a narrow distribution about that zeta potential peak. It is clear from these results that NMP fits these criteria best. Because of this, spraying using NMP as the solvent was attempted. Due to NMP's high boiling point, however (~200°C compared to IPA's ~80°C boiling point), the equipment was unable to safely produce a temperature at which the NMP would evaporate immediately and significant liquid running occurred, resulting in extreme non-uniformities and poor adhesion. A comparison of the NMP electrode of only five layers to an IPA electrode of 20 layers is shown in Figure 28.

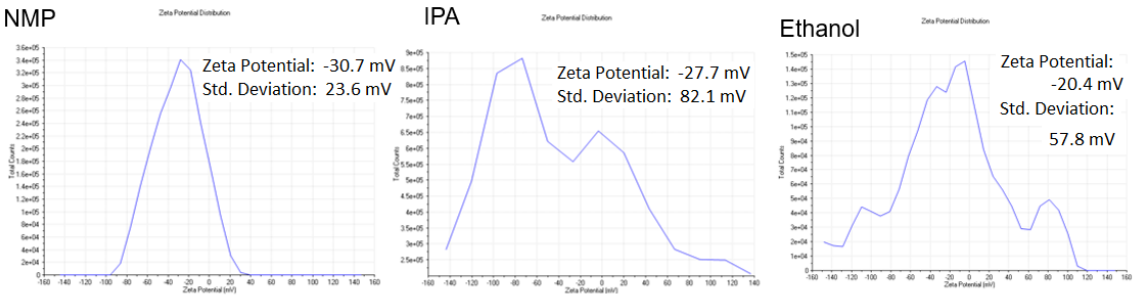

Figure 27: Zeta potential distributions for MWNTs in NMP, IPA, and ethanol

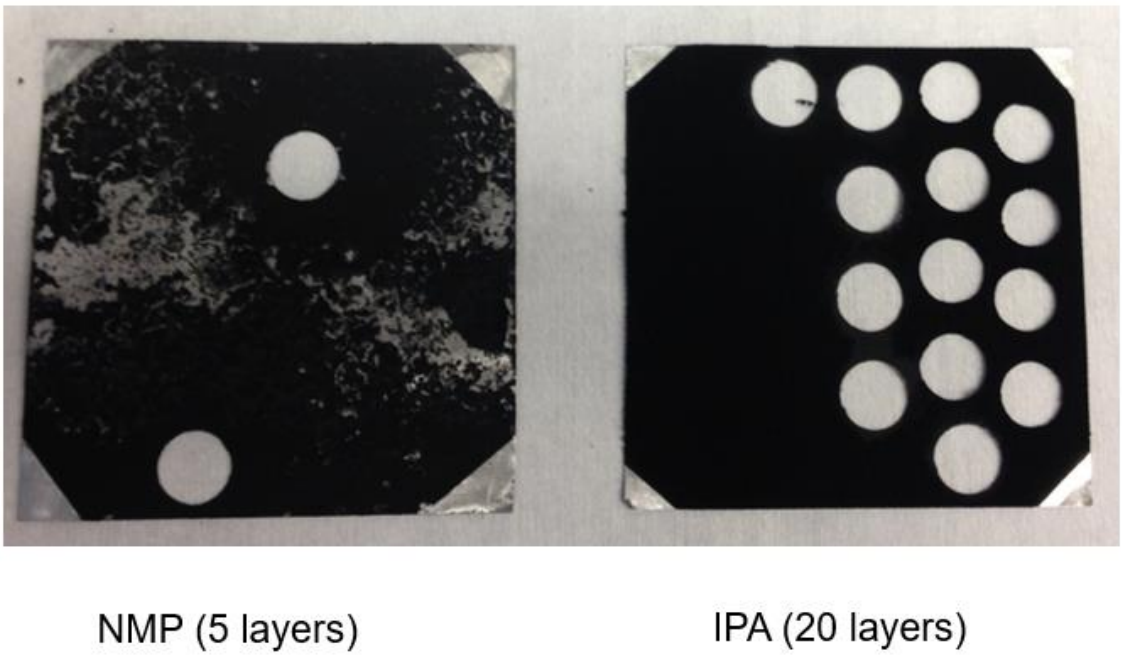

Figure 28: Comparison of electrodes made with NMP versus IPA as the solvent

Despite the difficulty in fabrication, cells were made with the NMP electrodes to compare to electrodes made with IPA and determine if there was a significant difference in cycling performance. The graph of these results (Figure 29) shows that both the NMP and IPA cells had nearly the same capacity at a charge/discharge rate of C/20. Because the performance was similar, but the NMP electrodes came out so poorly, all further spray cast electrodes were made using IPA.

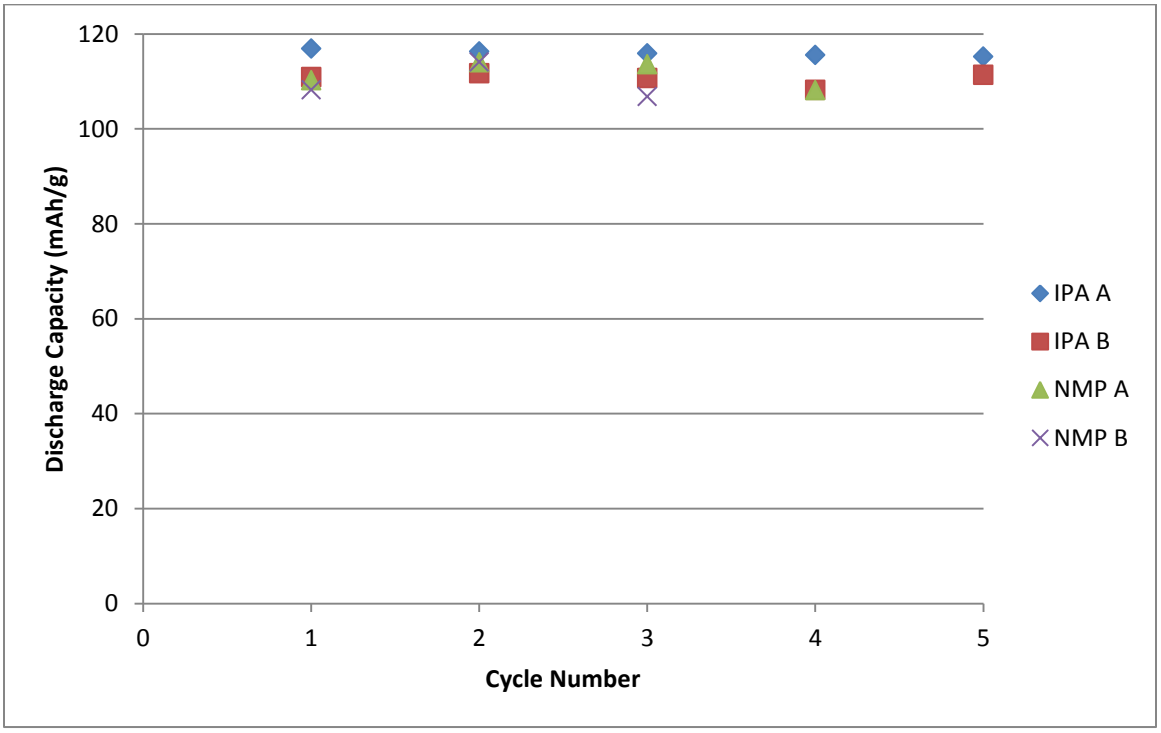

Figure 29: Capacity versus cycle number of NMP and IPA based spray cast electrodes at C/20. The active material composition is LMO:CB:PVDF (85:10:5).

3.2.4 Conclusions and Future Directions for Fabrication

The fabrication process for multi-layer electrodes has been developed and adapted to several different methods: doctor blade (standard) casting, spin casting, and spray casting. The uniformity and consistency of the electrodes made using these techniques have been examined, and it has been determined that both the doctor blade technique and spray casting technique yield electrodes with similar standard deviations in mass and thickness to the substrate itself, therefore they are as uniform as could be expected. The spray casting technique is favorable for multi-layer electrodes because the doctor blade technique is not well adapted to adding new layers on top of existing coatings. The fabrication parameters for spray casting were further investigated, and it was demonstrated that the only factor which significantly affects the loading of active material is the sprayed solution concentration.

Future applications for these batteries may include large-scale, thin structural batteries: batteries that could be sprayed onto the walls of a vehicle or aircraft. This would require uniform spraying over a much larger area, and adaptation of the process to include a solid electrolyte instead of liquid because a vertical or curved battery cannot use liquid, as gravity would cause the electrolyte to sink to the bottom of the battery.

3.3 Electrochemical Testing of Half Cells

The half-cell consists of an electrode (either anode or cathode) cycled with pure lithium foil as the counter-electrode. The lithium foil provides a stable, non-polarizable anode, thereby allowing for the isolation of just the electrode being tested. Measurements in a half cell configuration have been carried out in two formats: a T-cell (Figure 30 a), and a coin cell (Figure 30 b). In the T-cell, the electrodes and separator reside at the junction of the T and are pressed together by the stainless steel bars, which also act as the electrical contacts for current and potential measurements. One of the bars is spring loaded to maintain a slight pressure on the electrodes. Electrolyte is added from the middle opening of the T-cell, and then the cap is sealed. The coin cell used is a CR 2025 cell, and is configured in the same way as commercial button cells. The electrodes and separator are housed in the steel casing filled with electrolyte. The coin cell is also spring loaded to maintain pressure on the electrodes. Coin cells are the preferred format because the automated crimping process ensures consistent pressure, whereas the hand-tightened T-cells do not have that guarantee. Both formats accommodate and electrode of area 1 cm^2. All cells use a polypropylene separator and an electrolyte composed of lithium hexafluorophosphate ($LiPF_6$) dissolved in a 1:1 mixture of ethylene carbonate (EC) and dimethyl carbonate (DMC).

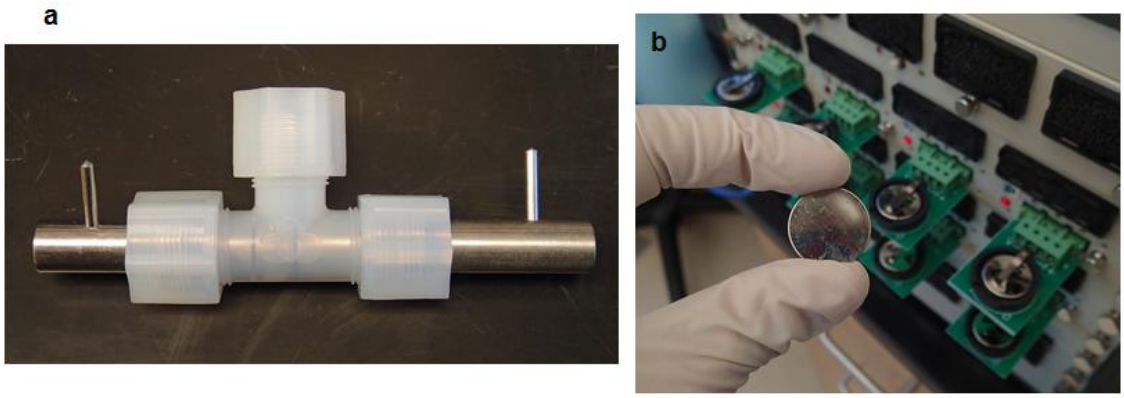

Figure 30: Cell configurations for testing: (a) T-cell, (b) coin cell

3.4 Silicon Anode Half Cells

3.4.1 Galvanostatic Testing

Figure 31 shows the charge/discharge curves for a silicon anode with loading of 0.44 mg/cm^2 at a rate of C/10, meaning full charge or discharge in 10 hours. The first (blue), second (green), and third (orange) cycles are shown. This shows the cumulative capacity of the cell (versus lithium foil) as the voltage changes, and the plateaus in voltage correspond to the intercalation of lithium ions. There are several notable features of this graph: one is the plateau seen at about 0.7 V in only the first discharge. This is attributed to the formation of the SEI layer, and therefore represents an irreversible capacity loss. This is not seen on subsequent cycles because the SEI layer is only formed in the first cycle. The first cycle also shows a long plateau at 0.1 V, which corresponds to the conversion of crystalline silicon into amorphous silicon. The sloping profiles of the subsequent cycles are consistent with the de/lithiation of the newly formed amorphous silicon [81-83]. The increasingly sloping profiles are characteristic of capacity fade, as evidenced by the decrease in capacity from about 4000 mAh/g in the first cycle to 2500 mAh/g in the second, and 1800 mAh/g in the third.

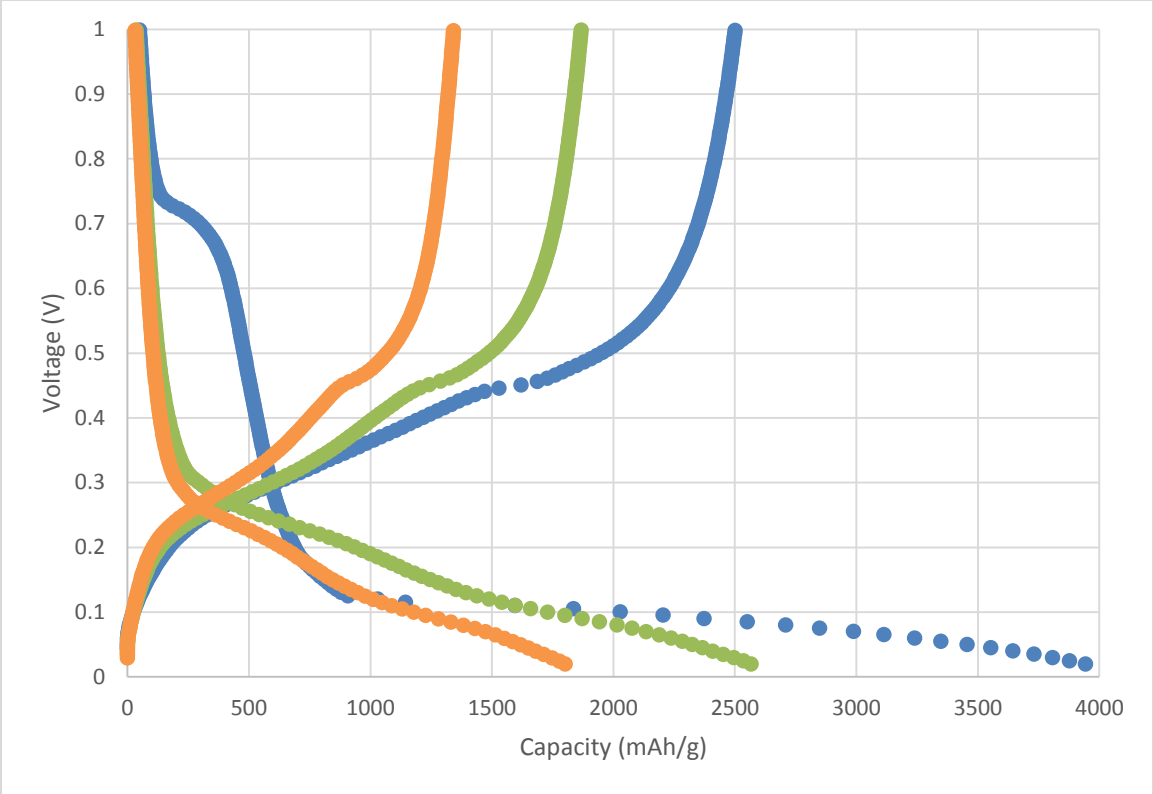

Figure 31: Charge/Discharge curves for silicon anode of loading 0.44 mg/cm^2. The blue curve is the first cycle, green is the second, and orange is the third. Active material composition is Si:CB:PVDF (70:20:10). C-rate: C/10.

Figure 32 shows a comparison of a 1-layer spin-cast silicon anode to a standard fabrication silicon anode and a standard fabrication graphite anode, each 1 cm^2 in area. Cells were cycled between 0.02 Volts and 2 Volts at a rate of C/20. For silicon, this corresponds to a current of 210 mA/g; for graphite, it is 18.6 mA/g. A one-layer silicon anode made using the spin casting process described above was compared to a standard fabrication silicon anode as well as a standard fabrication graphite anode. The graphite anode, as anticipated, shows a capacity between 300-400 mAh/g and remains fairly constant with only minor capacity fade over the five cycles shown. The standard silicon anode has an initial capacity over 3000 mAh/g (around 75% of silicon's theoretical capacity), but fades rapidly over just five cycles, as expected for silicon. The one-layer silicon anode shows an initial capacity higher than theoretical. This is because the mass of the CNTs is not included in the normalization calculation, even though they do intercalate lithium at the voltage range used. It has been found that CNTs have a very large irreversible capacity in the first cycle, so while they do intercalate lithium, their contribution is

only significant in the first cycle and they are therefore excluded from the mass calculations. This gives results that seem too high for the first cycle, but are within the expected values for subsequent cycles [72]. These results confirm the expected outcomes that silicon performs better than graphite, at least for the first several cycles, and that silicon is subject to severe capacity fade. They also show that the layered architecture offers a significant capacity enhancement over standard fabrication techniques, even though it is still subject to the same capacity fade.

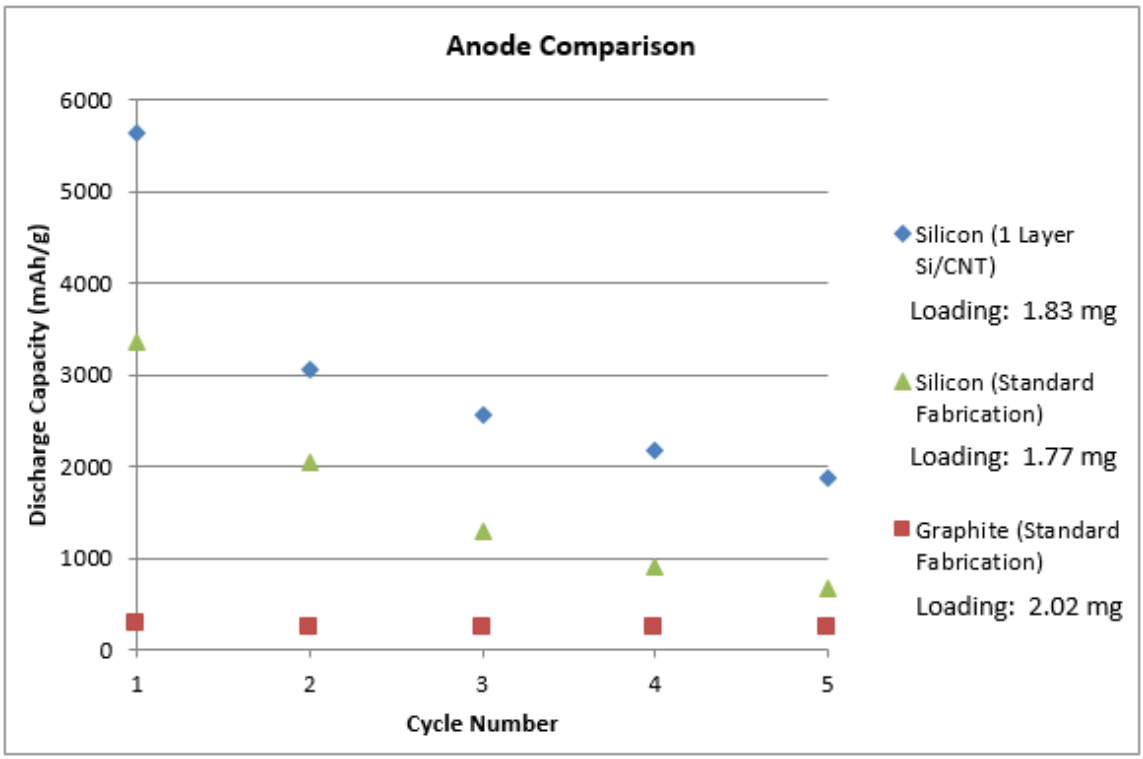

Figure 32: Comparison of electrode performance for a layered silicon anode, standard silicon anode, and standard graphite anode at C/10. Active material layer composition for silicon anodes: Si:CB:PVDF (70:20:10); for graphite anode: graphite:CB:PVDF (90:5:5).

Testing at higher C-rates has also been performed on layered silicon anodes, as shown in Figure 33, the capacity versus cycle number for a one-layer CNT/Si anode with loading of 0.78 mg. Each step up in C-rate is accompanied by an expected small decrease in capacity, and the return to C/10 in the final five cycles shows a corresponding increase in capacity. Because of the

extreme capacity fade, however, it is difficult to make a useful determination of the rate capability of these cells.

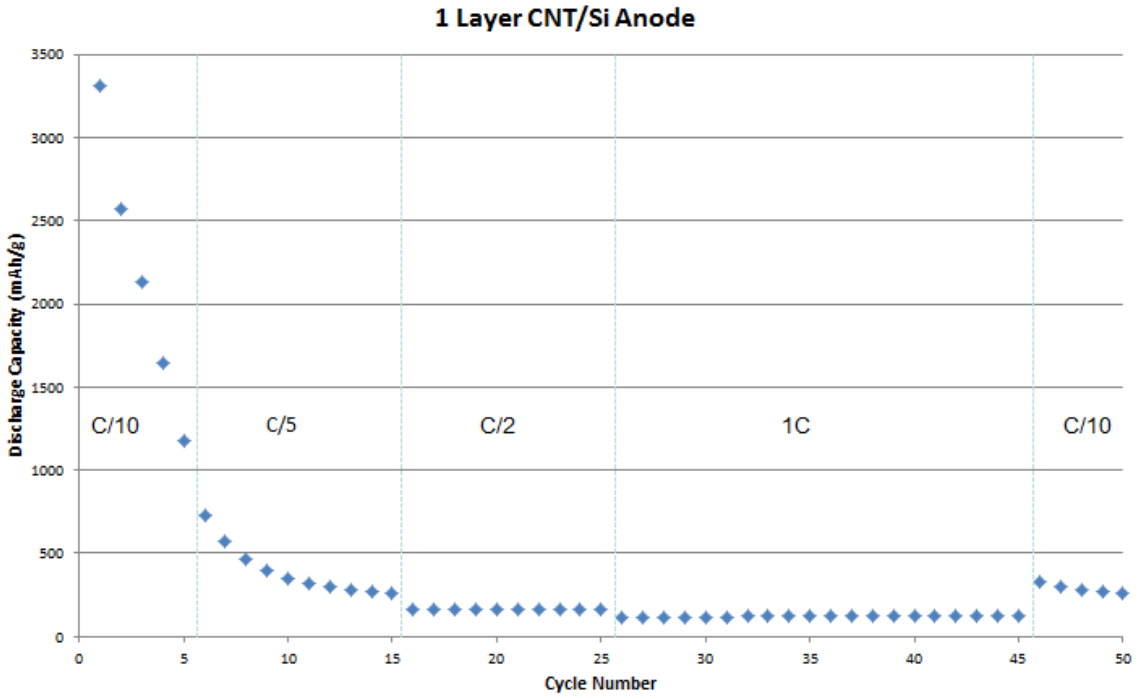

Figure 33: Galvanostatic testing of a one-layer silicon anode at different C-rates. Active material loading: 0.78 mg, composition: Si:CB:PVDF (70:20:10).

3.4.2 Physical Characterization

Electrodes were examined using SEM imaging before, during, and after cycling in order to characterize the surface morphology of the layered architecture and also get a sense of the physical changes occurring on the surface of the electrode during cycling. Figure 34 is an SEM image of the surface of a one-layer silicon anode before cycling. Ideally, the CNT network would be in contact with every silicon particle to provide a conducting path to the substrate, and this is generally true: most silicon particles seen here are contacted by at least one CNT. The CNTs are randomly oriented, creating a tangled network which allows for contact between neighboring CNTs, thus ensuring that all silicon particles can be accessed through this network. It can also be

seen that the active material layer is porous, allowing the top CNT layer to connect to the bottom CNT layer, and providing a conductive path through the whole electrode.

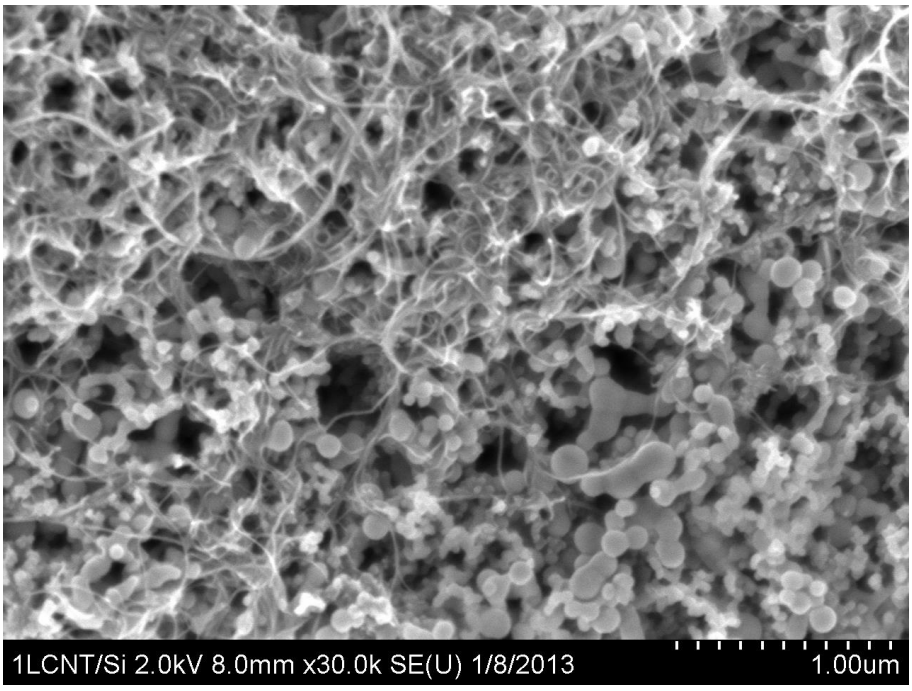

Figure 7: SEM image of the surface of a one-layer silicon anode. Magnification is x30k.

To better understand the structural changes happening within the cell, images were taken of a standard fabrication anode before cycling and after one charge. These images, taken at the same magnification, are shown in Figure 35. As expected, the silicon particles display extreme expansion in the charged state. Because of this expansion, all pores seen in the uncharged silicon layer are filled, and it is hard to see any of the carbon black particles (the smaller, irregular shaped particles in the uncharged image).

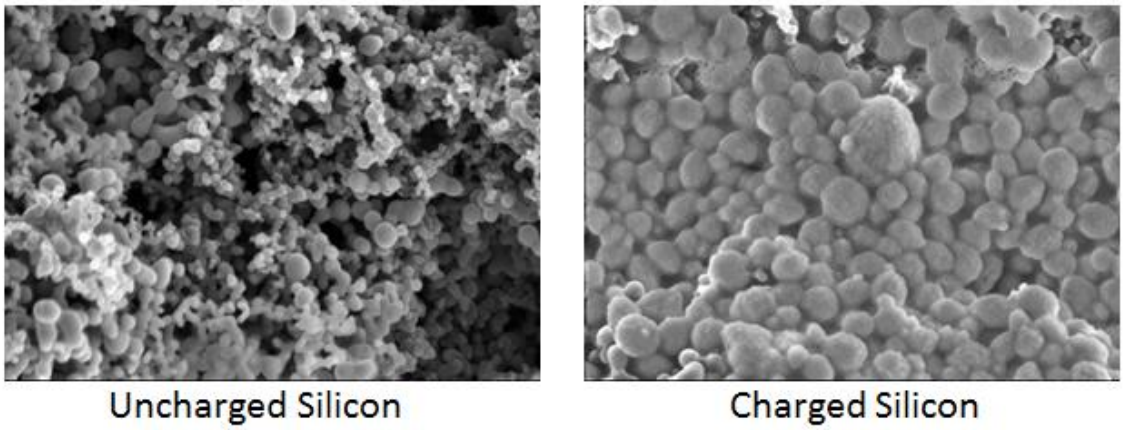

Figure 8: SEM images of uncharged and charged silicon nanoparticles Magnification for both is x30k.

Continuing this study, images were taken after one full cycle and after 20 full cycles, and compared to an image of the same electrode before cycling. Again, these images were taken at the same magnification, and are shown in Figure 36. The electrode used was made using the standard fabrication process to better show the effects of cycling on the silicon particles. The image taken before cycling shows a porous layer of distinct particles, carbon black interspersed with silicon. After one cycle, the individual particles become less distinct and it is hard to distinguish any carbon black particles. After 20 cycles, the silicon particles have pulled together into large masses sitting atop a bed comprised mainly of the remaining carbon black particles. Because of silicon's insulating properties, there is no access to the silicon material on the inside of these large masses, and there also does not appear to be any access to the tops and sides of the masses either, since there is no carbon black surrounding those areas. This could be a very large factor in the capacity fade of these anodes.

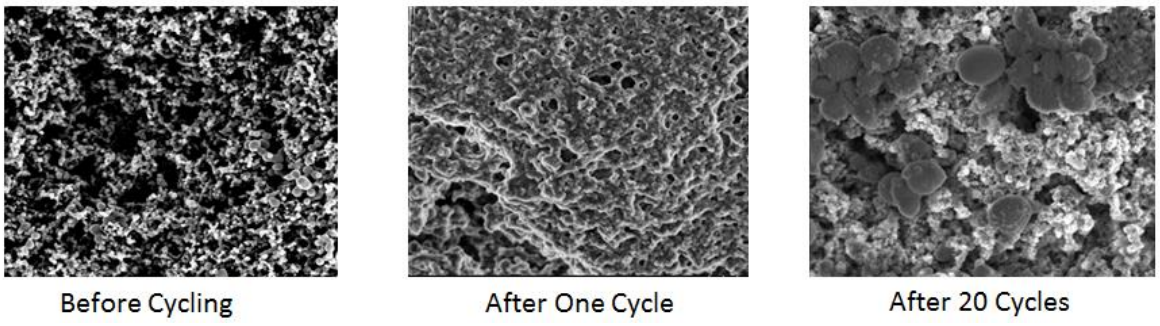

Figure 9: Physical effects of cycling a silicon anode. Magnification for all three is x10k.

3.4.3 Active material layer composition

The active material slurry for a silicon anode is made of three basic components: the silicon particles, a binder, and conductive additive(s). The type and quantity of each can have a large impact on the performance of the battery, therefore each of these components must be evaluated. Figure 37 shows cycling results for silicon nanoparticles from three different companies. Each company claims the particles have a purity of at least 98% and a size between 20-50 nm. Different fabrication processes, however, can lead to varied performance as seen here. From this, it can be concluded that particles obtained from US Research Nanomaterials, Inc (US Nano) give the best initial capacity, but fade slightly faster than particles from Nanostructured and Amorphous Materials, Inc (Nano Amorphous), and particles from Nanoshel did not perform as well in any area. Particles from US Nano were selected for all further experiments due to their high initial capacity and comparatively low cost.

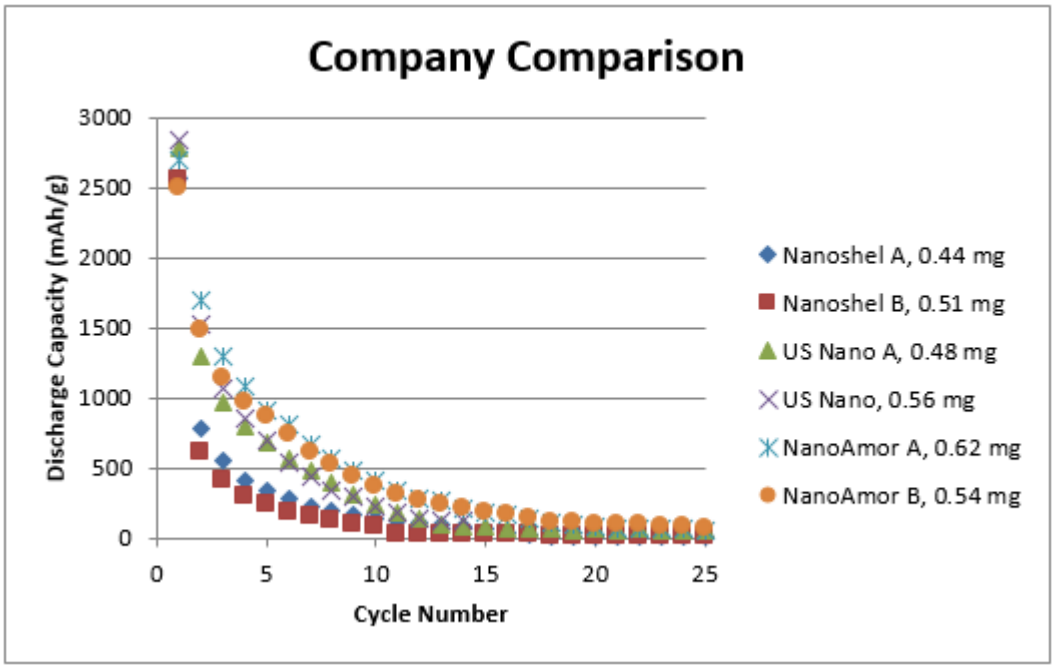

Figure 37: Discharge capacity vs. cycle number for electrodes made with silicon nanoparticles from three different companies. C-rate: C/10.

Two conductive additives were studied: carbon black and carbon nanotubes. Carbon black is the most common conductive additive, although CNTs are rising in popularity due to their high aspect ratio, which allows for lower weight loading while still maintaining conductivity [72]. Figure 38 gives the results of a carbon black content study: anodes made with 10%, 20%, and 45% weight carbon black. Although all cells showed similar performance, anodes with 20% weight carbon black gave the highest initial capacity. This indicates that increasing the carbon content from 10% to 20% did result in a better performance, but increasing the content further to 45% did not give any further enhancement. In order to maximize the amount of active material, therefore, 20% was chosen as the ideal carbon content.

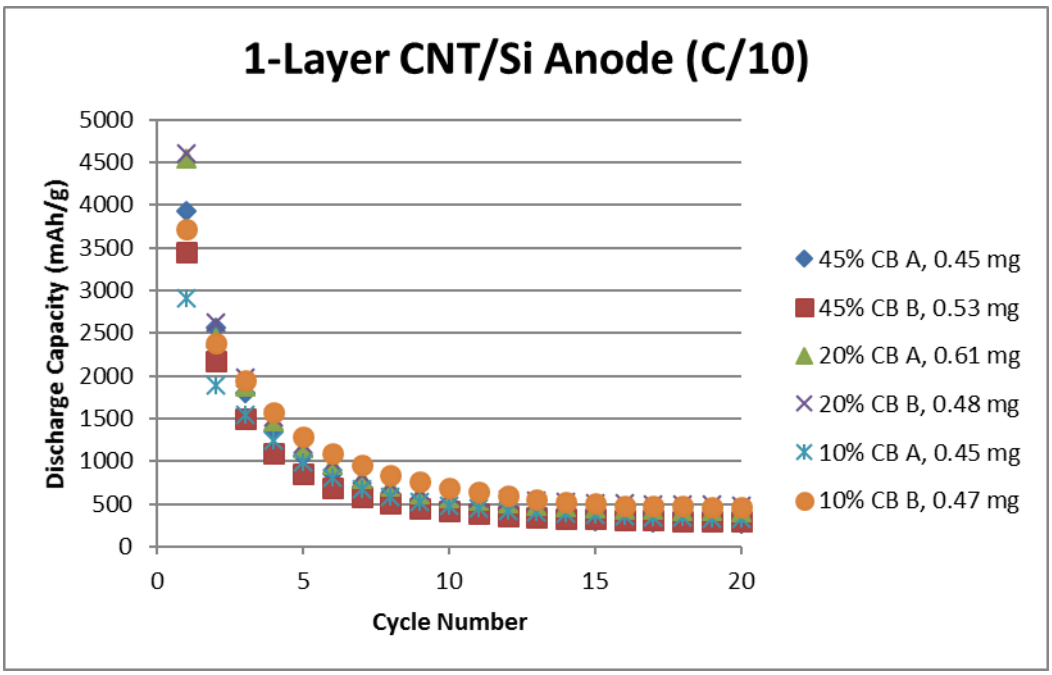

Figure 38: Carbon black content study results

The amount of CNTs as a conductive additive was also investigated. This does not include the CNTs comprising the conductive scaffold, but refers only to CNT additive within the active material layer itself. There were two approaches to this study: a low-loading approach, wherein the CNTs were simply used as a supplemental conductive additive (results shown in Figure 39 a), or a high-loading approach, using the CNTs as both a conductive additive and also a porous network into which the silicon particles could expand (results shown in Figure 39 b). Electrodes were fabricated in a standard fashion with no CNT scaffold. The results from the low-

loading CNT study show that the addition of CNTs at 1,2, or 3% weight slightly improved the capacity retention of the cells: those cells with 0% CNT faded fastest and those with 3% weight CNT faded slowest, although the difference is very small between 3% and 2%. It can be concluded that there is a maximum CNT content above which performance of the cell is not enhanced, and for the silicon anode, this quantity is 2% weight. The results of the high CNT loading study, in which 30, 40 or 50% weight CNTs were added further support this conclusion, showing only a minor improvement in initial capacity as compared to the low-loading, and no improvement to the capacity retention. Because it is always preferable to use more active material than additives to keep the total capacity and energy density high, the high loading method was ruled out and 2% weight CNTs selected as ideal.

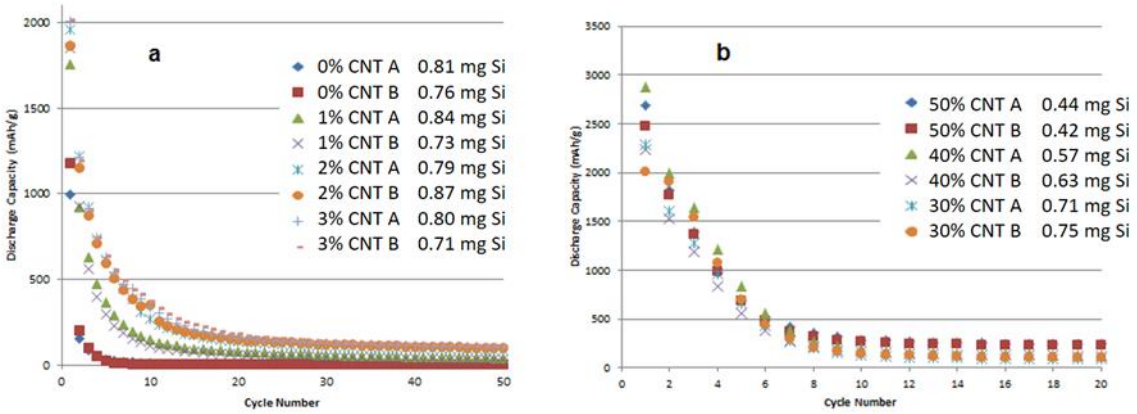

Figure 39: CNT content study results for (a) low CNT loading and (b) high CNT loading. PVDF content is constant at 10%; CB content is constant at 20% for (a), 10% for (b); remainder is silicon particles. C-rate: C/10.

3.4.4 Capacity Fade Mitigation Strategies

From all the results shown so far, it is obvious that capacity fade is still a major issue for the silicon anodes, whether standard fabrication or layered. Several methods of mitigating the capacity fade were attempted, based on the theories presented in the literature review section.

The first method was to give the particles a thin carbon coating, which ensures that each particle is in contact with the conductive network [16, 46]. Carbon coated silicon particles were fabricated by mixing silicon with a glucose solution, which was then carbonized by heating to

750°C under nitrogen flow. These particles were then used in place of bare silicon particle in the active material slurry. Results are shown in Figure 40. Figure 40a is a thermogravimetric analysis (TGA) of the particles, showing that the process resulted in particles that were 4% weight carbon. Cycling was carried out using two electrolytes: the usual EC/DMC mixture and the same mixture with an additive of vinylene carbonate (VC), which has been shown to enhance the performance of carbon coated particles [46]. Results of cycling are shown in Figure 40b. From this, it can be seen that the carbon coated particles actually performed much worse than the bare silicon particles, with an initial capacity below 500 mAh/g. The likely explanation for this is that the carbon coating actually restricted the expansion of silicon, prohibiting full lithiation. This theory is supported by Liu et al., who reported that without a void space in between the silicon and carbon coating, the initial capacity is reduced by about 60% and continues to fade from there [41]. A side result of this study, however, is the effect of using VC in the electrolyte: the bare silicon particles show slower capacity fade with VC versus without. It is thought that this is because it enables the formation of a more stable SEI layer.

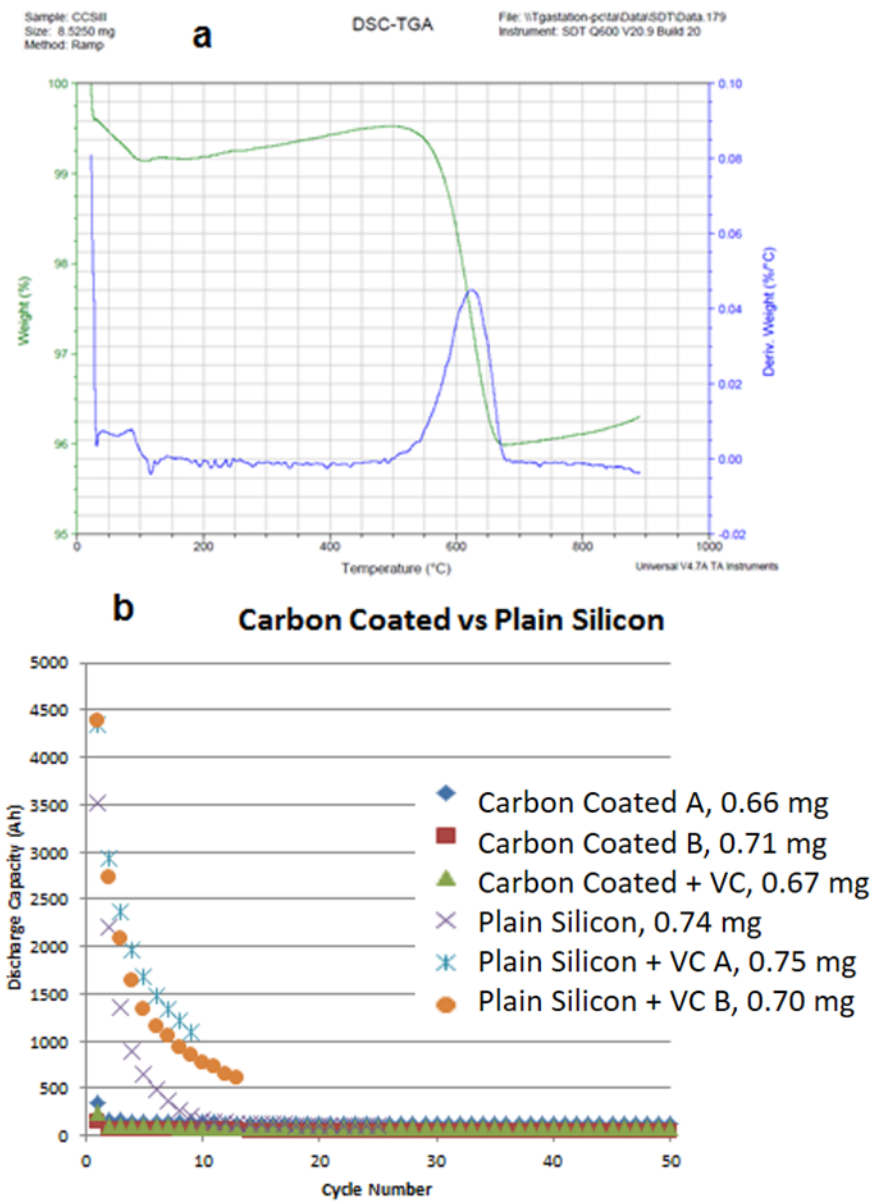

Figure 40: Carbon coated silicon particles: (a) TGA results, (b) discharge capacity vs. cycle number for carbon coated particles (with and without VC electrolyte additive) compared to plain silicon particles (also with and without VC). C-rate: C/10.

Another electrolyte additive shown to have a positive effect on silicon anodes is fluoroethylene carbonate (FEC). Like VC, FEC is thought to work by promoting the formation of a thinner, more stable SEI layer [61]. Results are shown in Figure 41 a for cells using 3%, 5%, and 10% weight FEC added to the electrolyte, as well as cells prepared with no FEC. From these, it

can be seen that the cells with FEC actually fade faster initially, but end up with a marginally higher capacity than cells without FEC. Looking at the voltage profile of the first sample (3% wt. FEC, 0.06 mg loading) shown in Figure 41 (b), the reason for the rapid capacity fade in the first cycle can be ascertained: the first discharge shows an enormous irreversible capacity in the voltage plateau seen at approximately 1 V. This plateau is associated with the formation of the SEI layer, so it is seen that the FEC does alter the formation of the SEI layer, however this data does not show it to be a favorable effect. In the voltage profiles shown in section 3.4.1 for a silicon anode with no electrolyte additive, the SEI layer formation represented about 500 mAh/g worth of capacity, while the capacity consumption here is over 1500 mAh/g worth, three times as much.

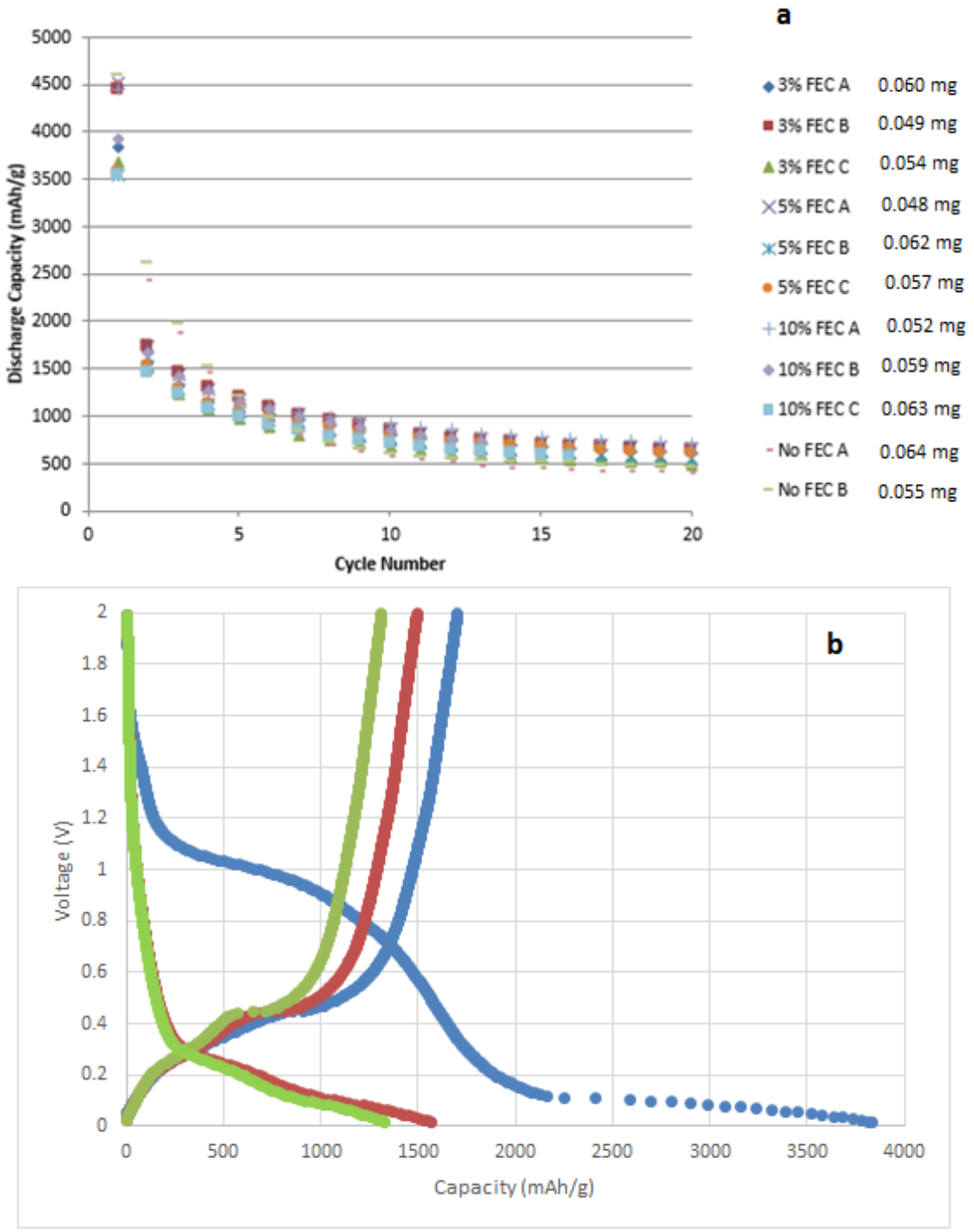

Figure 41: (a) Cycling results for cells with varying FEC concentration: 0%, 3%, 5%, and 10% weight. C-rate: C/10. (b) Voltage profile for sample with 3% wt. FEC in electrolyte, 0.060 mg loading. The first (blue), second (red), and third (green) cycles are shown. C-rate: C/10.

The use of alternate binders was also investigated. Sodium carboxymethylcellulose (CMC) has a higher electronic conductivity than the traditional PVDF, and has been researched as a potential binder for silicon anodes [57]. Results for three electrodes made with CMC instead of PVDF are shown in Figure 42, and indicate that the capacity fade problem is not reduced by the use of CMC. This is consistent with previous results (in section 3.4.3) showing that simply increasing the conductivity (increasing the carbon black or carbon nanotube content, for example) may give an advantage in initial capacity but does not prevent capacity fade. The SEM images shown in section 3.4.2 showed that the silicon forms large agglomerates, and this process was not hindered by the PVDF binder, so it is unsurprising that CMC, which has been shown to be more brittle than PVDF [57], is also incapable of preventing the agglomeration of silicon during cycling.

Another possible binder combines conductivity with an ability to overcome the expansion and contraction experienced during cycling through the use of a self-healing polymer (SHP). This polymer is an amidoamine with the ability to reform bonds after they have been broken, which allows for the binder to break apart during expansion but then seal back together after the material has contracted again, which, in theory, maintains better contact between the silicon particles and the conductive additive during cycling. Results for cells made with this binder are also shown in Figure 42. From this, it can be seen that not only is capacity fade still an issue, but the initial capacity is diminished greatly as well. The cause of this is likely due to lack of sufficient cross-linking in the polymer bonds, which caused the polymer to not cure properly during fabrication. This was evidenced by an excessively sticky, viscous texture that caused the active material to stick to the separator in the cell rather than to the substrate, and the lack of connection between the current collector and the silicon drastically reduced the capacity. It is clear that for this technique to work, significant optimization of the polymer fabrication process is required.

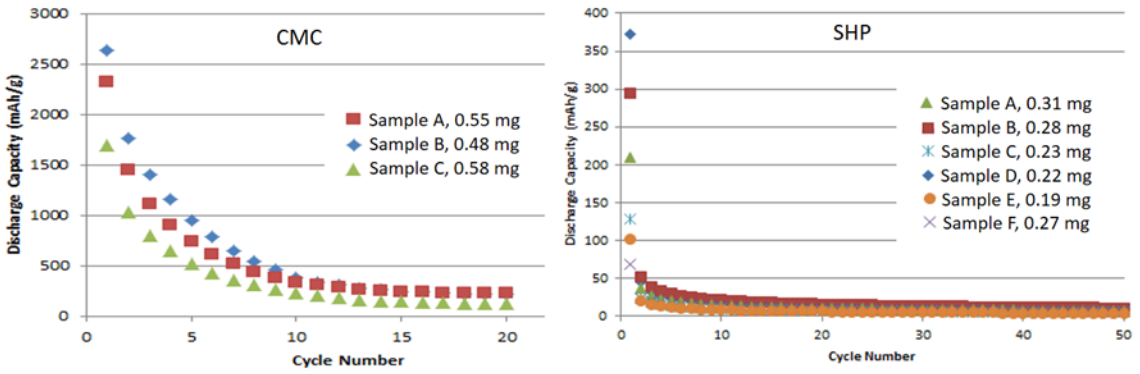

Figure 42: Cycling results for alternative binders: (left) Carboxymethylcellulose; (right) Self-healing polymer. C-rate: C/10.

The next strategy attempted was to increase the vacant space in the electrode. All electrodes are pressed in a hydraulic press before being tested to ensure good contact between the active material layers and the substrate. Silicon, however, requires room for expansion and the pressure may be detrimental to that. To test this theory, electrodes were made using standard fabrication procedures and then either not pressed (0 psi) or pressed at 1000, 3000, or 5000 psi, which is the usual pressure for electrodes. Cycling results are shown in Figure 43. The 5000 psi electrodes show the highest capacity, followed by the 3000, then 1000 and finally 0 psi electrodes, and all fade at about the same rate. This clearly indicates that reducing the pressure does not help the capacity fade and leads to lower overall capacity. Measurements of thickness before and after pressing show that the thickness of the active material layer is not significantly reduced (<1 micron difference), so it is apparent that the pressing step is not efficient at removing vacant space in the electrode, and this is why there was no notable change in the capacity fade for these electrodes. It is clear, however that the pressing step is essential to ensuring good contact between the substrate and material since the capacity is reduced without this step.

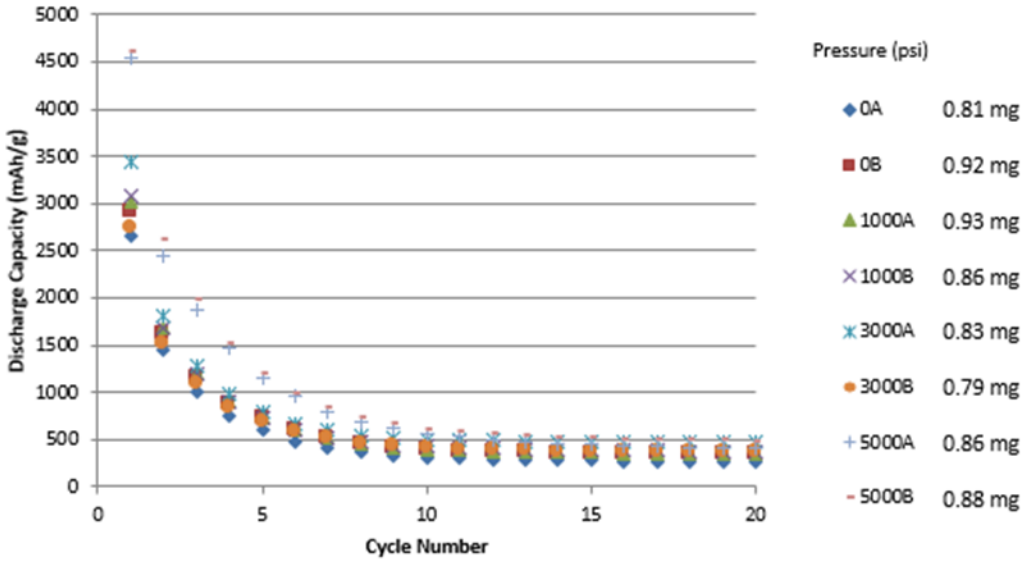

Figure 43: Cycling results for electrodes not pressed (0 psi) or pressed at 1000, 3000, or 5000 psi. C-rate: C/10.

An alternative to making the active material layer more conductive with additives is to make the particles themselves more conductive, which was attempted in the next strategy, using doped silicon particles. As discussed in the literature review, n-type doping with phosphorus can make silicon particles more conductive, so particles of this type were purchased and used to make standard fabrication anodes. The results, found in Figure 44 a, show very low capacity as well as a capacity fade of about 65% in the first cycle. The voltage profiles for the first (red) and second (blue) cycles in Figure 44 b show that these cells exhibit practically no voltage plateaus, indicating that very little lithium has been intercalated, accounting for the low capacity. The plateau at 0.1 V, normally the most prominent, is notably absent. Because this plateau corresponds with the formation of amorphous silicon from crystalline silicon, it may be that the doping process disrupts the crystalline structure of the silicon, rendering that mechanism useless, and removing any reversible capacity associated with it.

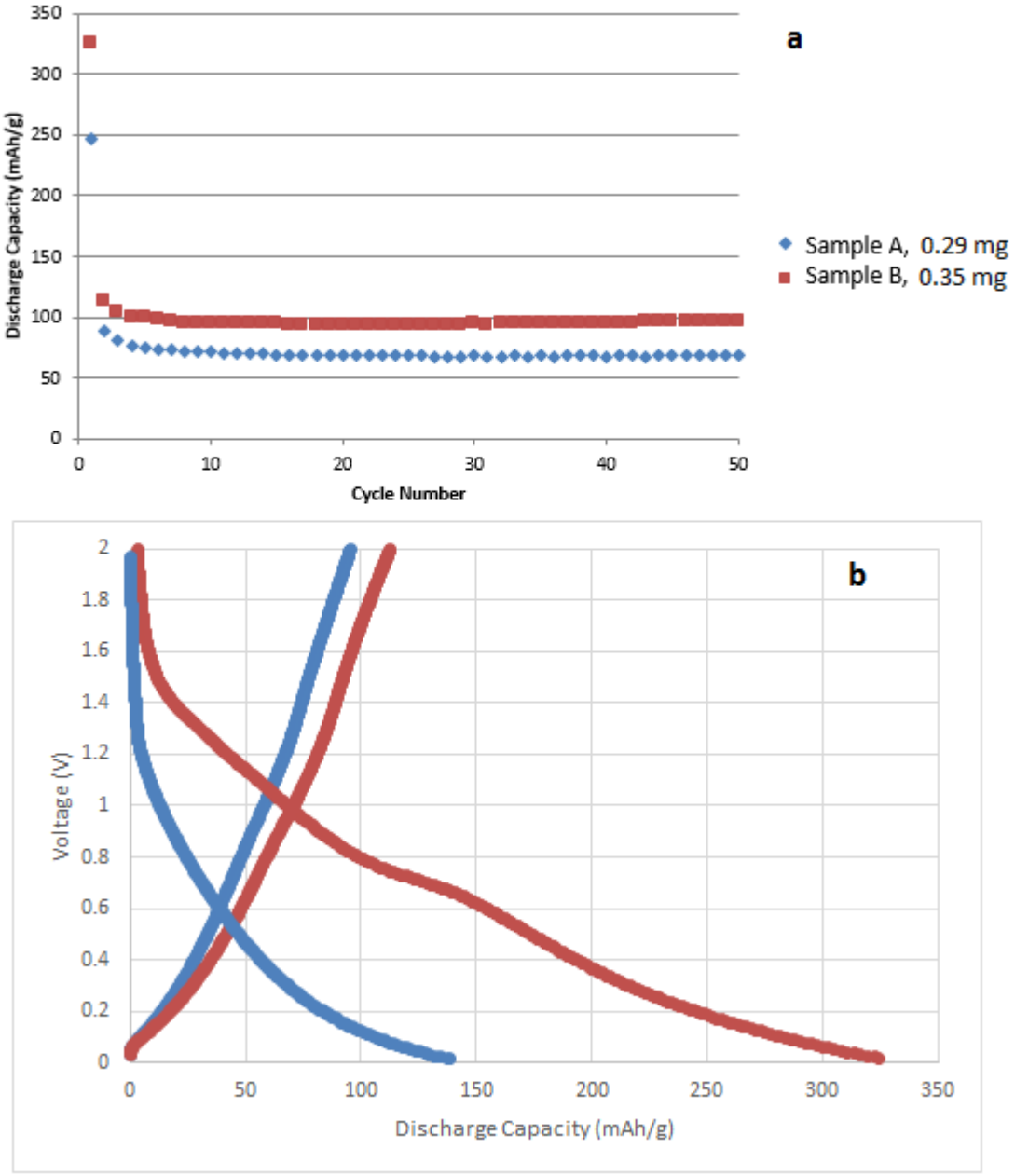

Figure 44: (a) Cycling results for two electrodes made with n-doped silicon nanoparticles, C-rate: C/10. (b) Voltage profile for first (red) and second (blue) cycles of n-doped silicon Sample A (0.29 mg), C-rate C/10.

It has been suggested that limiting the initial capacity of a cell will limit the irreversible capacity loss and overgrowth of SEI layer. To test this, cells were cycled as usual, but charging or discharging was cut off at a specific capacity value, either 2000 mAh/g or 1000 mAh/g. The

results of this test are shown in Figure 45. The flat start to the curves of cells A and B (limited to 1000 mAh/g) seemed to suggest this method might have merit, however, the curves quickly begin to slope down as usual after the first few cycles. It can be seen that this downturn occurs where the other two cells, C and D (limited to 2000 mAh/g), intercept at around 1000 mAh/g in cycle number two. This indicates that the cells would naturally have a capacity of at least 1000 mAh/g in this second cycle, and the two steady cycles of cells A and B at 1000 mAh/g only remain steady because of this. They then continue their natural degradation, just as if no capacity limitation had occurred, indicating that the SEI layer forms as usual.

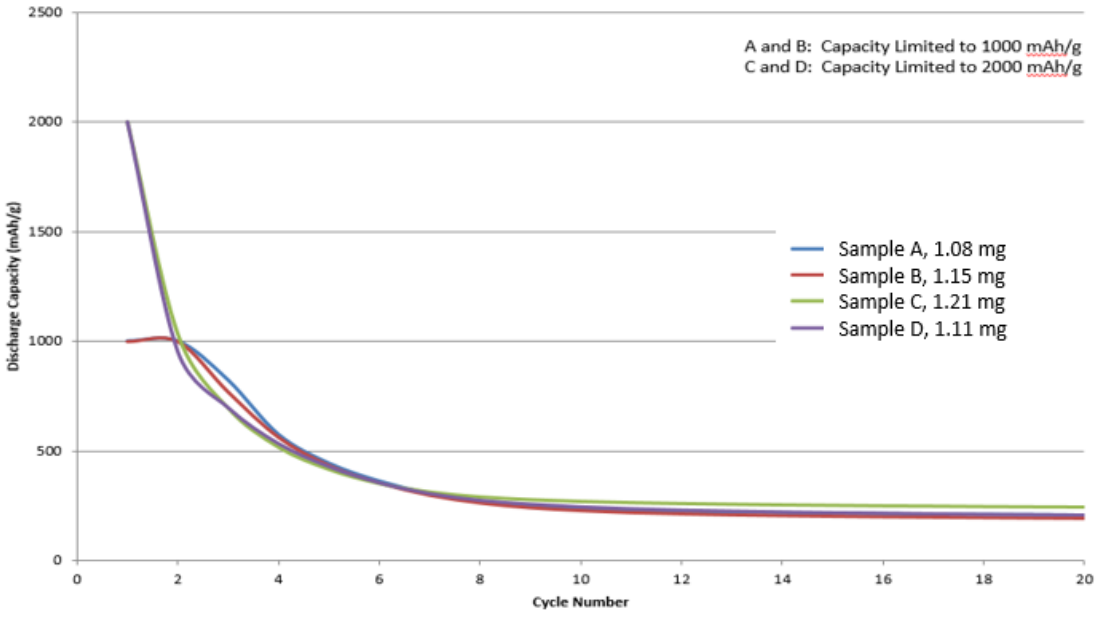

Figure 45: Cycling results for electrodes with limited initial capacity: A and B were limited to 1000 mAh/g, C and D were limited to 2000 mAh/g. C-rate: C/10.

3.4.5 Conclusions and Future Directions for Silicon Anodes

The silicon anode clearly requires further improvements before it can be made useful. As expected, the silicon nanoparticles show severe capacity fade in the first few cycles, however no solution to this problem has yet been identified which is also inexpensive, high-yield, and easily commercializable. Techniques explored here include increasing the conductivity of the electrode with carbon additives, carbon coatings, alternative binders and doped particles, controlling SEI formation with electrolyte additives and by limiting the initial capacity, and retaining vacant space by reducing the pressure on the electrode during the pressing step of fabrication. Despite the lack of positive results for these capacity mitigation strategies, it has been demonstrated that the capacity, power, and energy density are all improved by the multi-layer architecture. Future work should therefore focus on continuing to address the capacity fade issue, and when that is solved, the architecture will offer further performance enhancement.

3.5 Lithium Manganese Oxide Cathode Half Cells

Previous research conducted at the CHN investigated the effect of the layered architecture on the cathode. Selected results of this project are shown in Figure 44. Cells were found to demonstrate good capacity (>100 mAh/g) at C/10 (Figure 46 a), and have a higher power and energy output than standard fabrication cathodes (Figure 46 b). The layered architecture also enhanced the rate capability (Figure 46 c) The impedance spectra in Figure 46 d indicates that the charge transfer resistance (the difference between the first and second x-intercept) is dramatically reduced for the multi-layer structure and this is the reason behind the improved rate capability of the multi-layer electrodes [17]. The maximum active material loading reached during these experiments was about 10 mg/cm^2. This is not sufficient for commercial cells, which typically contain at least 20 mg/cm^2, therefore the next step with these cathodes was to attempt to increase the loading without sacrificing performance.

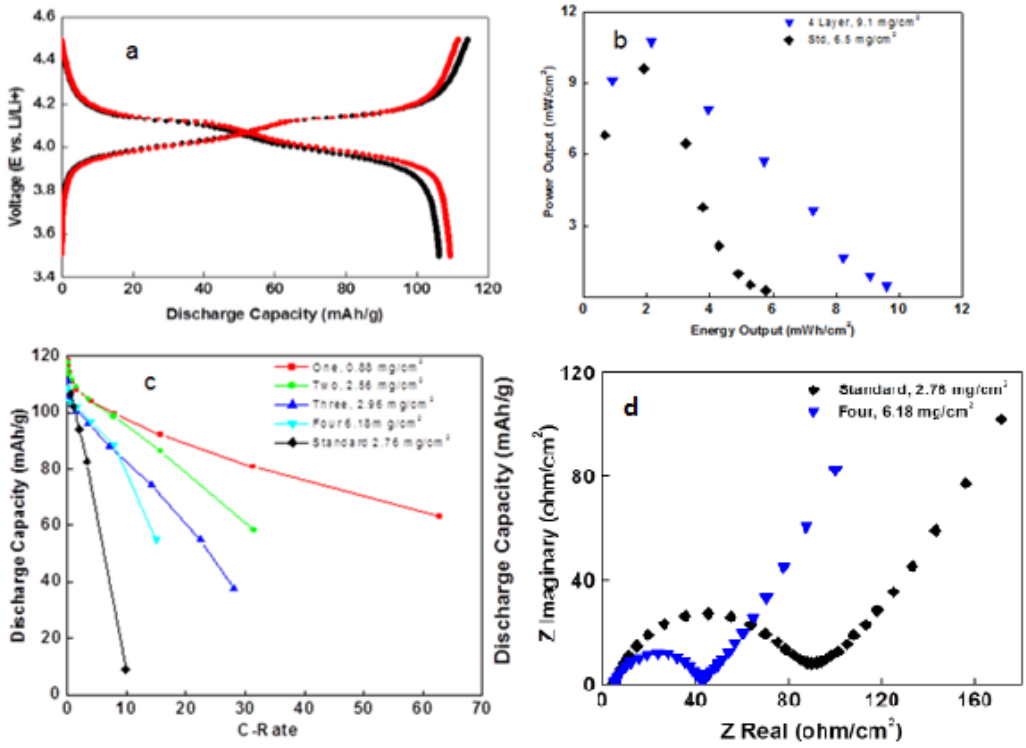

Figure 46: Cycling data for LMO half cells: (a) galvanostatic charge/discharge profile, (b) energy and power output of a four-layer and standard cathode, (c) rate capability of layered cathodes compared to standard, (d electrochemical impedance spectra of a 4-layer electrode compared to a standard cathode. Figure source: [17]

3.5.1 Increased Loading of LMO

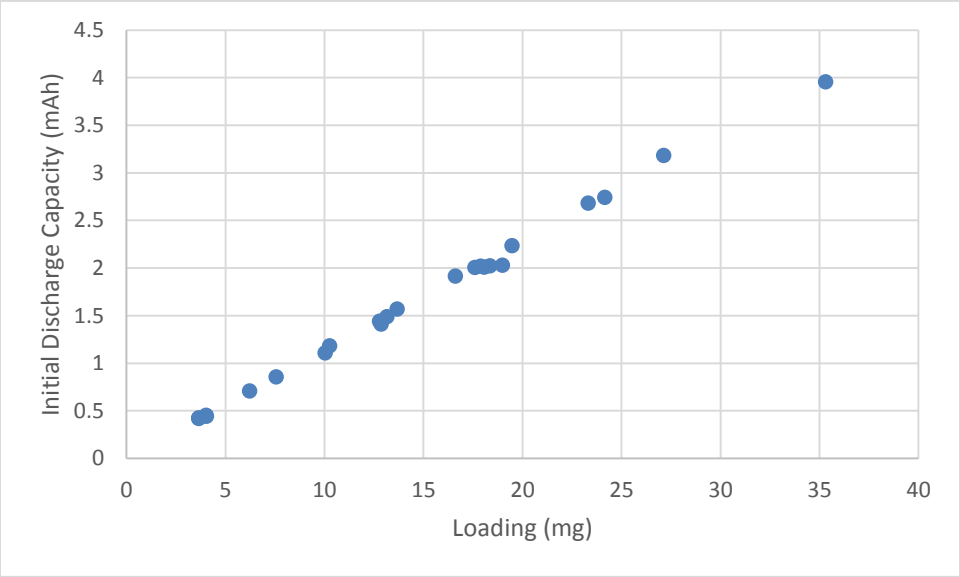

Figure 47: Capacity (mAh) versus active material loading (mg). Active material layer composition for all samples is LMO:CB:CNT:PVDF (85:9:1:5).

Figure 47 is a graph of initial discharge capacity (at a rate of C/20) versus active material loading for 23 different spray-cast multi-layer LMO half cells. The trend is nearly perfectly linear, indicating that full utilization of the material is attained at all loadings. In fact, a linear fit to this data gives a slope of about 114 mAh/g, which is 95% of the maximum attainable capacity for LMO. In addition, one might expect an upper limit on the amount of material that could be loaded onto the substrate and still get full capacity from it. If this limit had been reached, the data would start to flatten out at higher loadings, as the loading increased more than the capacity. Because no such flattening is observed, we can conclude that even at 35 mg/cm^2, the limit has not yet been reached. Figure 48 shows the performance of a multi-layer cell with extremely high loading (64.58 mg). The curve for the cycle at a rate of C/5 shows the characteristic two-phase lithium insertion centered at 4 V (each phase showing a voltage plateau at about 3.9 and 4.1 volts). The more sloping profile seen at the higher rate of 1C and the corresponding lower capacity is consistent with the increase in charge/discharge rate. This

cell shows 81% of maximum capacity at a rate of C/4, and 52% of theoretical capacity at 1C, demonstrating that reasonable cycling can be achieved even at loadings much higher than typical commercial batteries.

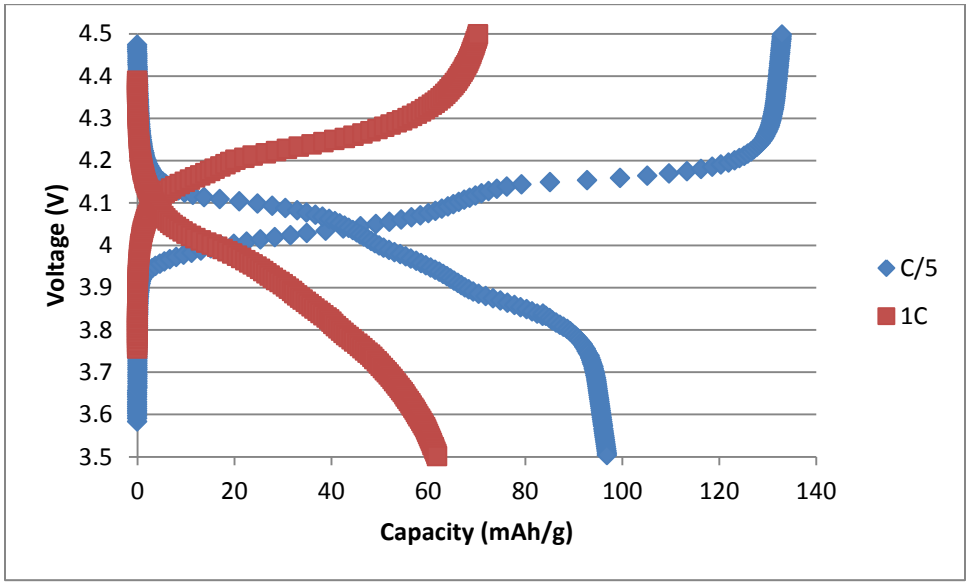

Figure 48: Capacity of a cell with very high active material loading (64.58 mg) at C/5 and 1C rates. Active material layer composition is LMO:CB:CNT:PVDF (85:9:1:5).

Figure 49 shows the rate capability of several higher-loading electrodes, from 4.05 mg/cm^2 to 35.32 mg/cm^2. It was seen in Figure 46 that the rate capability was heavily dependent on the active material loading, but the layered structure allowed significantly more active material loading than the standard electrodes while maintaining superior rate performance. Here it can be seen that even at high material loading, the multi-layer architecture allows for good rate capability, with cells up to 20 mg/cm^2 delivering more than 70% of full capacity at a rate of 2C. As expected, the rate capability drops as the loading increases (because the thickness and therefore ion transport distance are also increased). Also shown on this graph is a standard fabrication electrode for comparison. Although the loading of this electrode was 8.40 mg, its performance most closely resembles the multi-layer electrode with a loading of 24.17 mg, indicating that it is possible with the multi-layer structure to achieve equivalent rate performance with three times the loading of standard. The multi-layer cell with

the most similar loading (7.57 mg) to the standard (8.40 mg) had a capacity of 95.4 mAh/g at a rate of 2C, while the standard cell only had a capacity of 50.5 mAh/g. This is nearly double the capacity for a similar loading. As stated previously, this improved rate capability is due to the decreased charge transfer resistance achieved with the multi-layer structure.

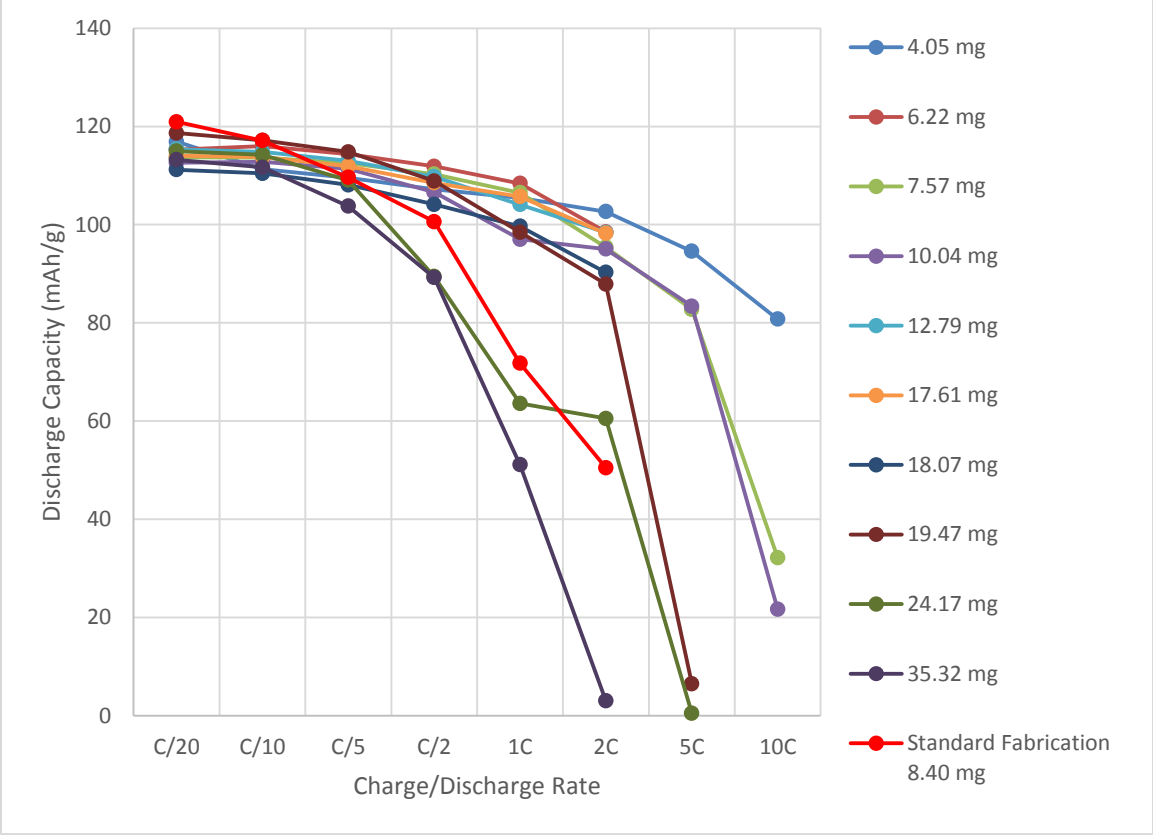

Figure 49: Rate capability of spray-cast LMO cathodes with high active material loading compared to a standard fabrication cell (red line). Active material layer composition for all samples is LMO:CB:CNT:PVDF (85:9:1:5).

Figure 50 is a Ragone plot for selected cells from Figure 47, showing the energy density versus power density. As the C-rate increases, we expect cells to provide less energy since the charge and discharge time is shorter, but greater power for the same reason. Furthermore, it is expected that the energy and power densities will decrease with higher loading (although raw power and energy will be higher with higher loading) because of the increased thickness of the active material layer, and therefore increased ion diffusion distance and time. This behavior is

observed in all cells, except that the standard fabrication cell performs much worse than the multi-layer cells. With a loading of 8.40 mg, directly in between the multi-layer cells with 6.22 mg and 10.04 mg loadings, the expected performance would also be between these two cells, however the standard cell performs closer to the 35.32 mg multi-layer cell. This clearly indicates that the CNT network does decrease ion diffusion time as hypothesized. In fact, the multi-layer architecture allows for the loading to be more than quadrupled while still maintaining equivalent energy and power densities.

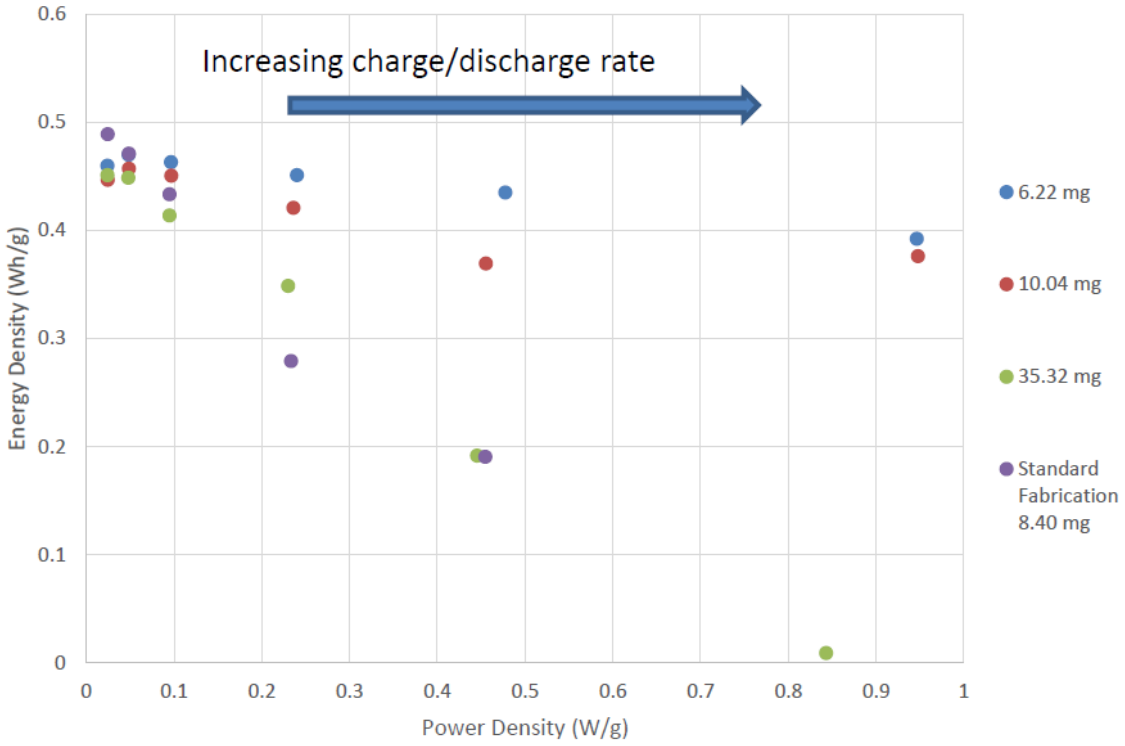

Figure 50: Ragone plot of LMO cathodes versus lithium foil. Active material layer composition for all samples is LMO:CB:CNT:PVDF (85:9:1:5).

These cells also demonstrate resiliency after failure. Figure 51 shows cycling data for a cell with active material loading of 17.89 mg/cm^2. At a rate of 2C, this cell began to abruptly fade, at 5C it holds a minimum capacity level, and at 10C it shows no capacity at all. However, in between each of these rate changes, the cell was allowed to charge and discharge at C/20 for

two cycles, and for these cycles the capacity returned to over 100 mAh/g, showing that it was still capable of cycling at lower rates even after failure at high rate.

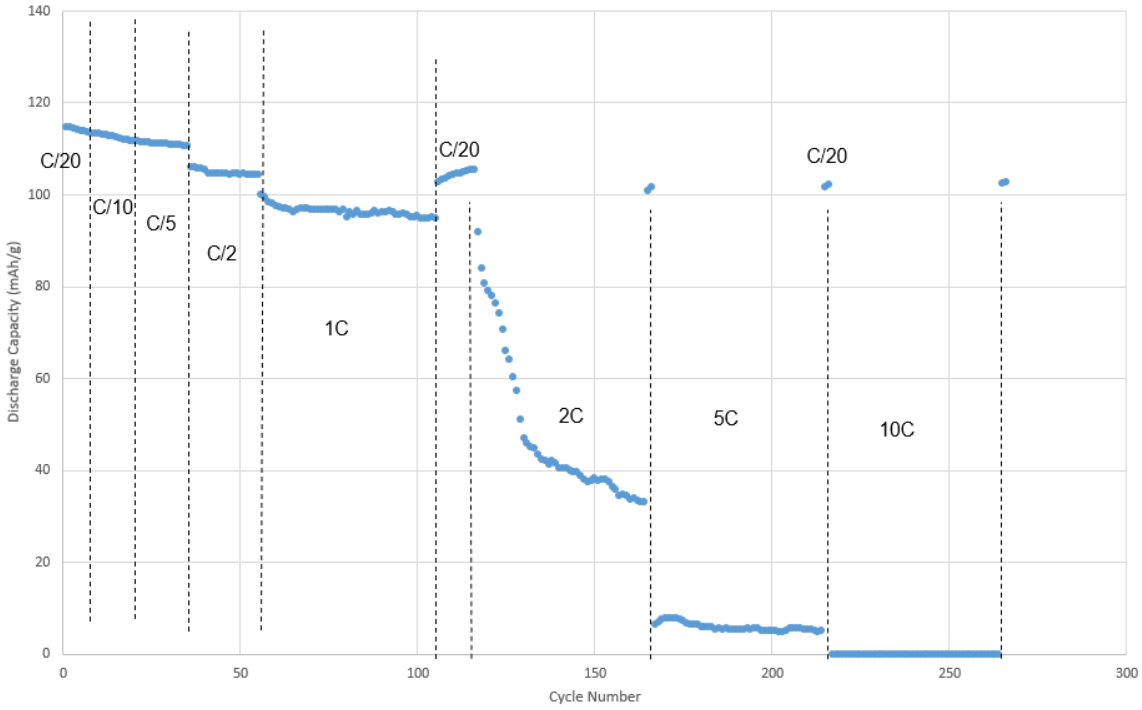

Figure 51: Cycling data for a cell with active material loading of 17.89 mg showing resiliency after failure.

3.5.2 Connectivity of CNT Layers

A major advantage of the layered architecture is the connectivity of the CNT layers. It is assumed that the porosity of the layers allows each CNT layer to be connected to the ones above and below, creating a conducting network through the electrode. To test that this is, in fact, the case, an electrode with deliberate connections between layers was fabricated and compared to a multi-layer electrode. The first steps in making this interconnected electrode were identical to a normal multi-layer, spray-cast electrode. Ten layers of the active material mixture were sandwiched between eleven CNT layers on an aluminum substrate. Material was then removed from the electrode, exposing the aluminum in three stripes as shown in the schematic in Figure 52. These areas were then filled in with CNTs, creating a direct connection through the electrode, making contact with each of the eleven CNT layers, and leading to the aluminum current collector. If the multi-layer structure was already connected as it was

hypothesized to be, this would not be necessary, and no performance advantage would be observed. Figure 53 shows the cycling results for the interconnected electrode compared to a ten-layer electrode without the extra interconnects. The two electrodes show nearly identical behavior across all charge/discharge rates, therefore it can be concluded that the multi-layer architecture is sufficiently connected throughout the bulk of the material.

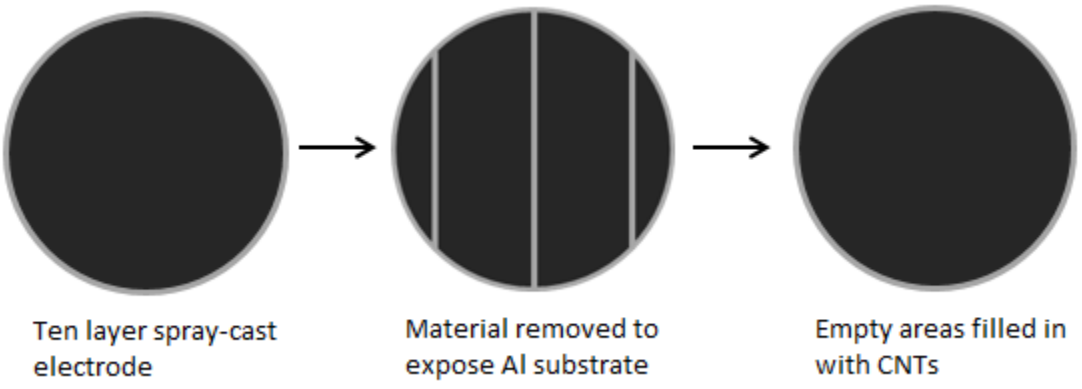

Figure 52: Schematic showing method of creating interconnected ten-layer LMO electrode

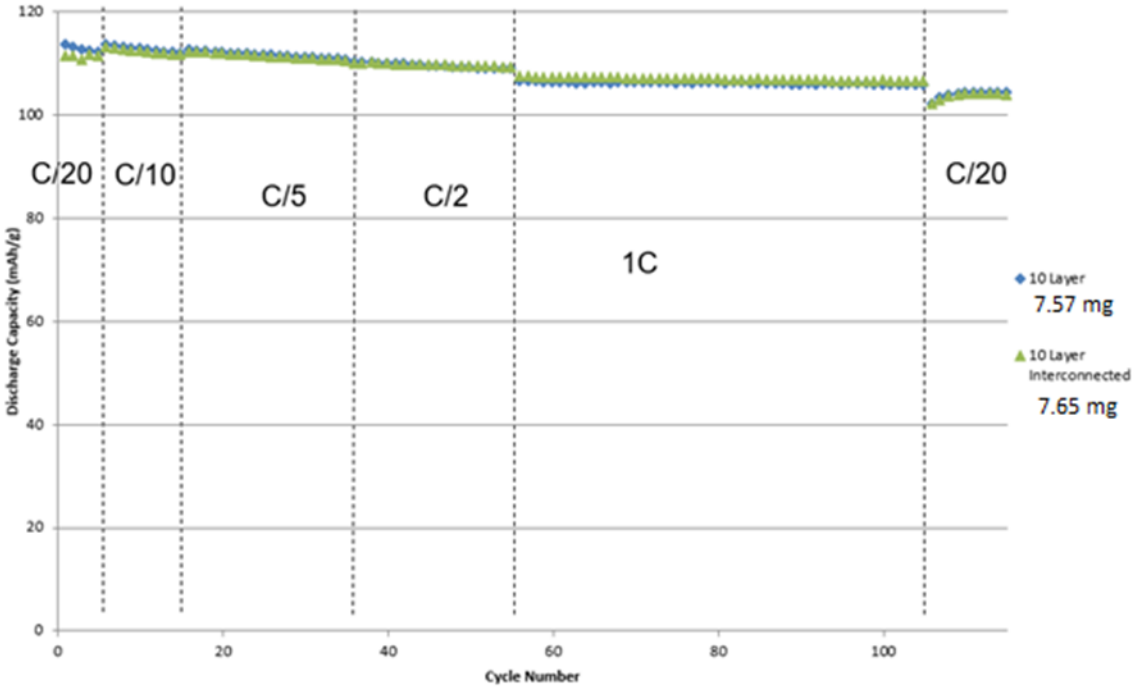

Figure 53: Comparison of normal ten-layer electrode and interconnected ten-layer electrode. Active material layer composition for both samples is LMO:CB:CNT:PVDF (85:9:1:5).

3.5.3 Density of CNT Layers

The density of the CNT layers was also investigated to determine if an ideal existed. The average density for spray-cast electrodes was 0.08 mg/cm^2 of CNTs per each layer. To determine the effects of altering this density, electrodes were fabricated to have fewer CNTs: 0.04 mg/cm^2, and more CNTs: 0.12 and 0.16 mg/cm^2. Top-view SEM images of the CNT layers were taken (Figure 54) for visual comparison, and cycling results are shown in Figure 55. There is a clear difference in the SEM images, as it is easier to see through the less dense CNT layers to the LMO layers below. The cycling results, however, show no clear performance advantage to having either less dense or more dense layers, with no significant difference in capacity, power or energy density (shown in Figure 56). It can be concluded that the CNT layers need not be very dense in order to provide the necessary conductive pathways for lithium ions and electrons. Since it is always preferable to minimize non-active materials in order to maintain high gravimetric and volumetric capacity, power, and energy density, the density of the CNT layers was henceforward kept to a minimum.

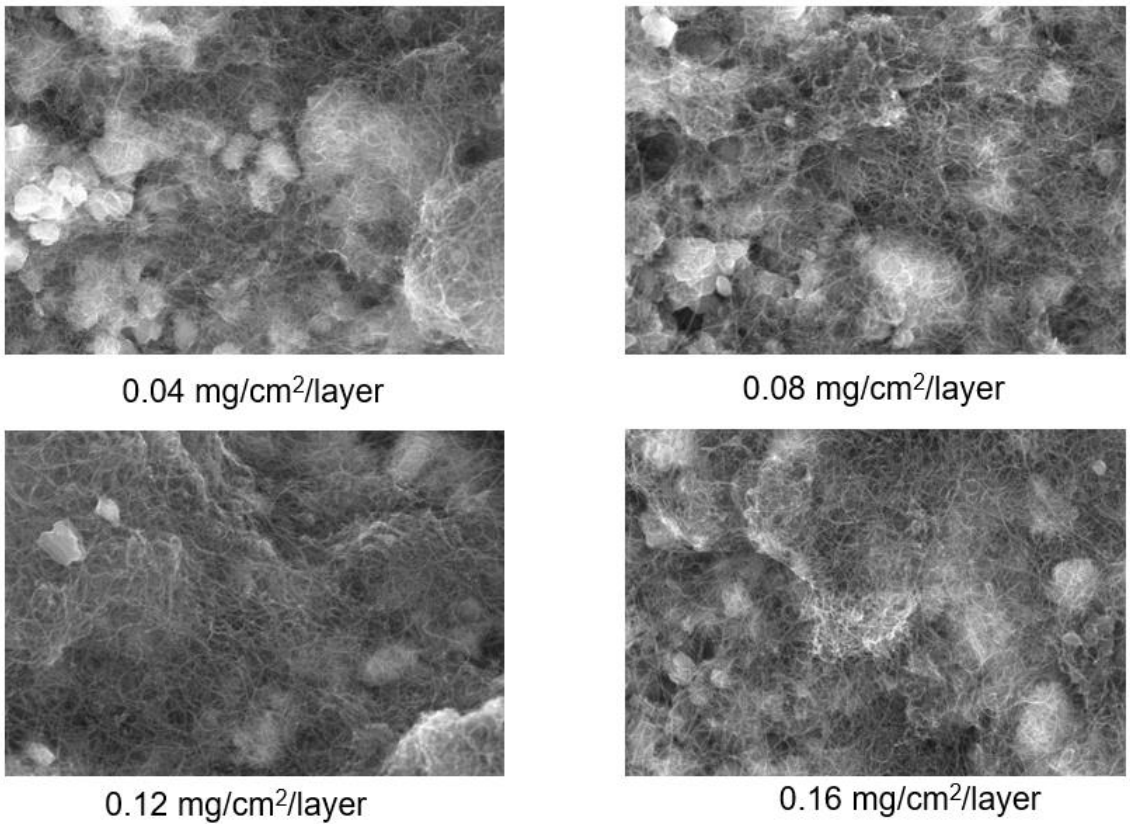

Figure 54: SEM images of CNT layers of varying densities

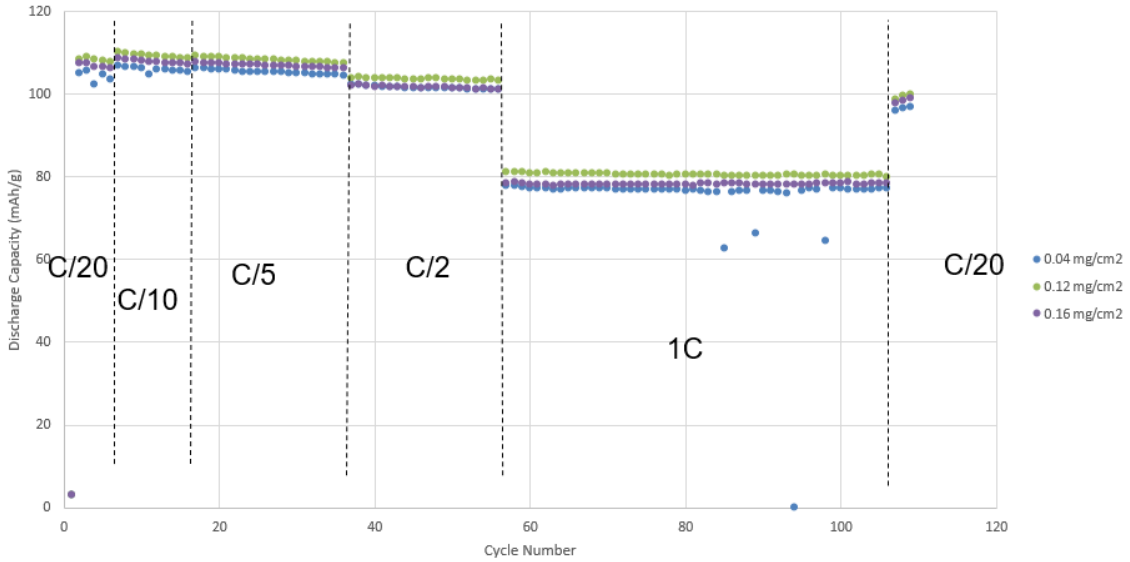

Figure 55: Cycling of electrodes with varied CNT layer densities. Active material layer composition for all samples is LMO:CB:CNT:PVDF (85:9:1:5).

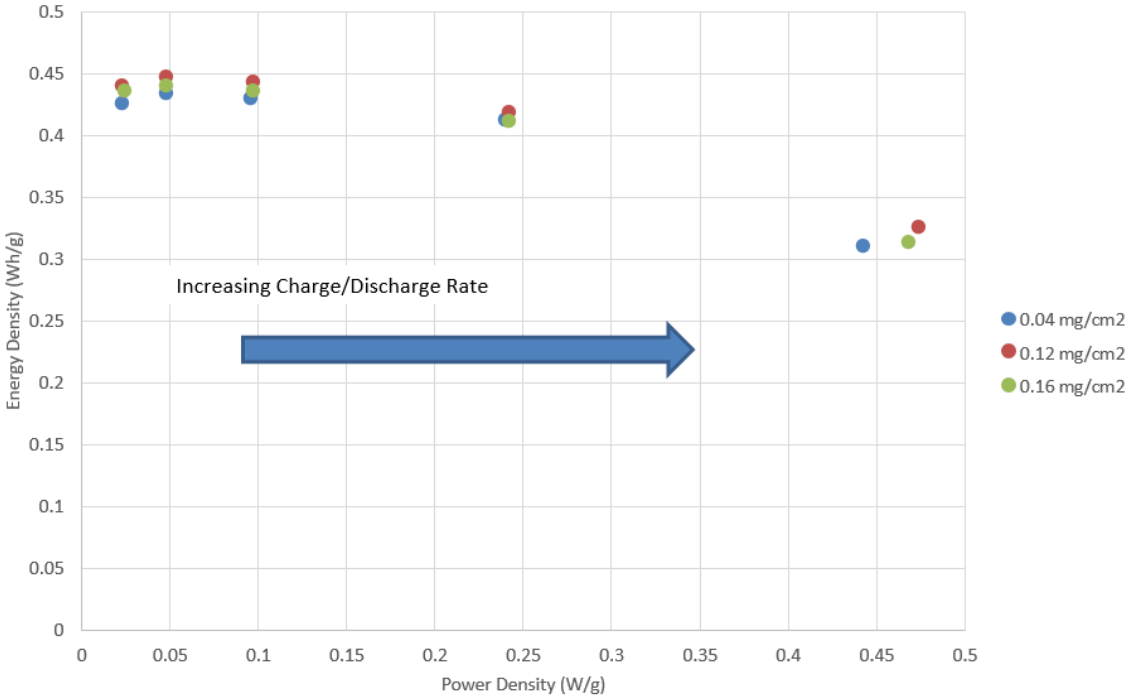

Figure 56: Ragone plot of electrodes with varied CNT layer densities versus lithium foil.

3.5.4 High-Power Applications

The data presented so far was for cells cycled at the same charge rate as discharge rate, however for most applications, this is not the case. In high-power applications, for example, the charge rate is much slower than the discharge rate. To demonstrate the multi-layer architecture's ability to perform well under these conditions, a five layer spray-cast electrode was compared to a single layer standard fabrication electrode. These cells were cycled with the charge rate held constant at C/20 for all cycles while the discharge rate was increased incrementally from C/20 to 5C. The loading of the five layer electrode was 11.26 mg and the loading of the standard electrode was 6.99 mg. Despite having higher loading, the five layer electrode performed substantially better, as can be seen in Figure 57. While the standard cell's capacity drops noticeably with each increase in discharge rate, the five layer cell's capacity drop is barely perceptible each time, and when the standard cell finally fails, showing zero capacity at

5C, the five layer cell is still cycling steadily with a capacity exceeding 110 mAh/g, 92% of maximum.

It is also worth comparing this to the previous data for cells that were cycled with charge and discharge kept at the same rate. A similarly loaded electrode from section 3.5.1 showed a discharge capacity of about 98 mAh/g at 5C, while this electrode has a capacity of 112 mAh/g at the same rate. This is to be expected because of the slower charge rate for this cell, and indicates that batteries cycled under these high-power application conditions will perform even better than the previous data suggests.

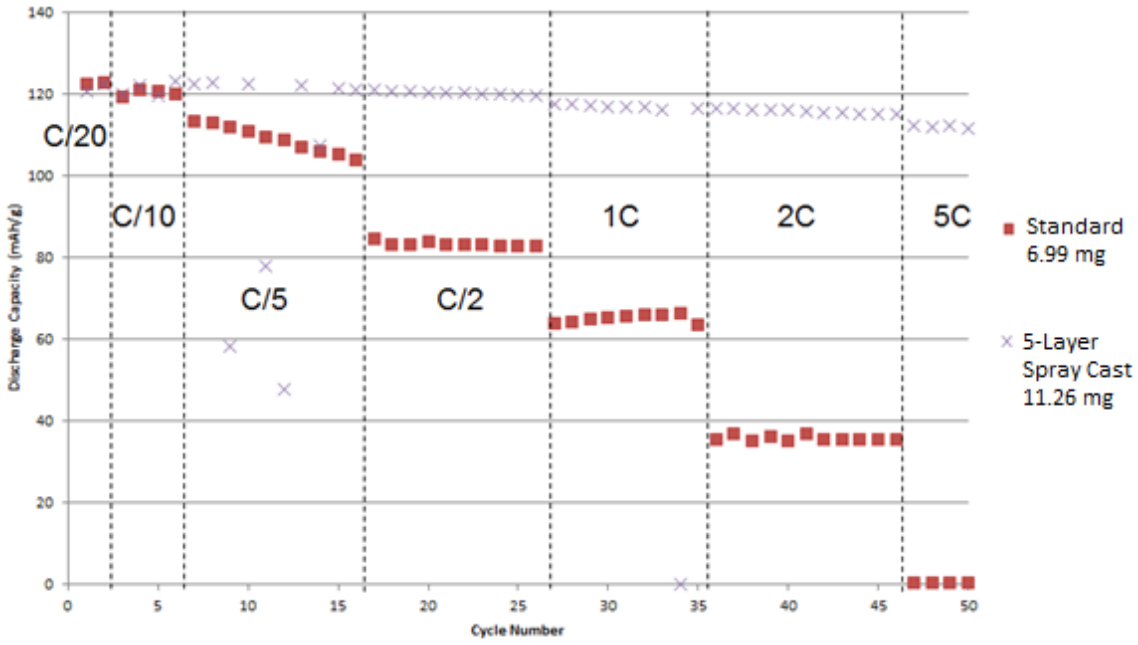

Figure 57: Cycling of a five layer spray-cast cell compared to a standard fabrication cell simulating a high-power application: charge rate was held at C/20 for all cycles while the discharge rate varied from C/20 to 5C. Discharge rate is displayed on the chart. Active material layer composition for both samples is LMO:CB:CNT:PVDF (85:9:1:5).

Figure 58 shows the power and energy density for the same cells as Figure 57. With each increase in discharge rate, the power increases, however, the five layer cell shows slightly higher jumps in power density each time. An even more significant difference is the energy density, which decreases with each step up in discharge rate. The energy of the standard cell

rapidly decays until it hits nearly zero at 5C, while the five layer cell maintains a high energy density even as the power increases. This demonstrates that the multi-layer architecture can substantially lessen the tradeoff between power and energy density.

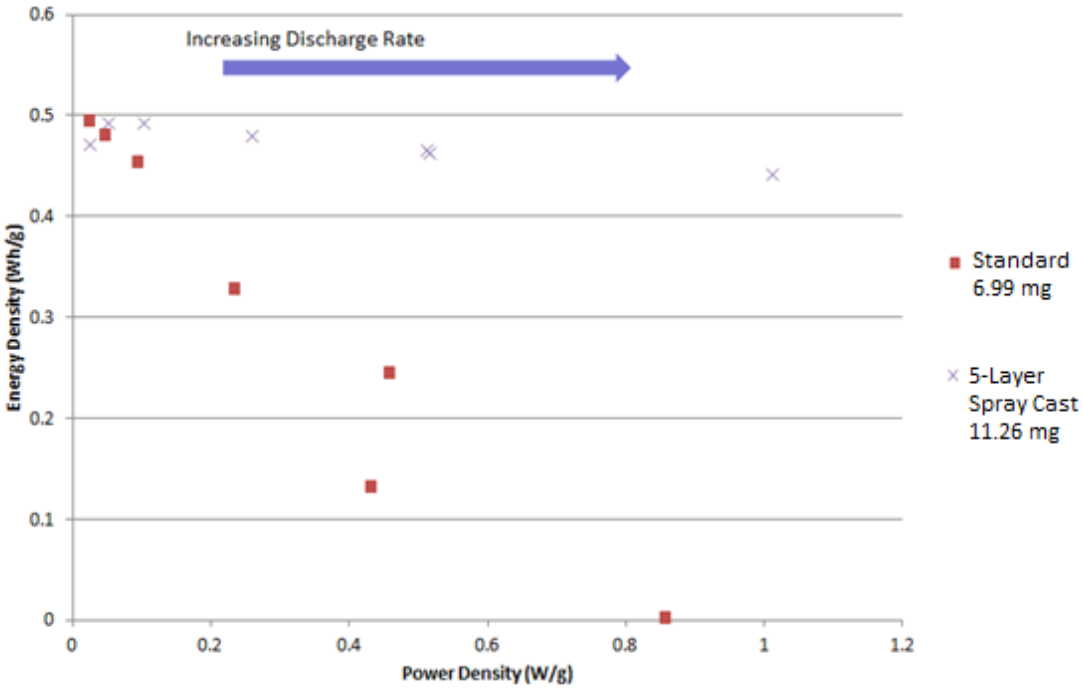

Figure 58: Ragone plot (versus lithium foil) of a five layer spray-cast cell compared to a standard fabrication cell simulating a high-power application: charge rate was held at C/20 for all cycles while the discharge rate varied from C/20 to 5C.

3.5.5 Carbon Nanotube Paper Electrodes

An alternative method of fabrication is to use carbon nanotube paper in place of the assembled CNT layers. The CNT paper, provided by Nanocomptech Inc. and shown in Figure 59, is made from a network of >1 mm long CNT bundles, held together only by the tangled nature of the CNT bundle deposition; no binders or fillers are used [84]. An advantage of this is the structural integrity of the CNT sheets: because they are self-supporting, no substrate is needed. This eliminates a significant portion of dead weight from the electrode: for a typical coin cell

electrode (1 cm^2) with 20 mg/cm^2 loading, the total electrode mass is approximately 44 mg, 47% of which is the aluminum substrate. It does add extra mass to the CNT layers, with a density of 0.5-0.8 mg/cm^2, rather than the previously mentioned 0.08 mg/cm^2 per layer for sprayed CNT layers. It would take at least 20 layers, however, before the added CNT mass equaled the aluminum mass. In addition, the CNT paper electrodes are extremely flexible, which could open up pathways to new applications, as the field of flexible batteries is growing.

These electrodes were fabricated by spreading the active material slurry (LMO:CB:PVDF 85:10:5) onto a glass plate, and then alternatingly placing a sheet of CNT paper on top and spreading a new layer of slurry. Spraying was not successful for more than one layer because the structure relies on the wet slurry to hold the sheets together until they are dried in the oven, but the sprayed solution dries nearly instantly. It may be possible to come up with an adapted spraying process in the future.

Much like in the previous section, the density of the CNT layers was investigated, this time by using three different CNT sheets of varied density and thickness. SEM images of the three samples are shown in Figure 60. Sample 1 was least dense with a density of 5.52 g/m^2 and average thickness of 6 µm. Sample 2 had a density of 8.85 g/m^2 and average thickness of 14 µm. Sample 3 was thickest and densest, with a density of 11.24 g/m^2 and average thickness of 71 µm. They do not show any significant physical differences in the SEM images.

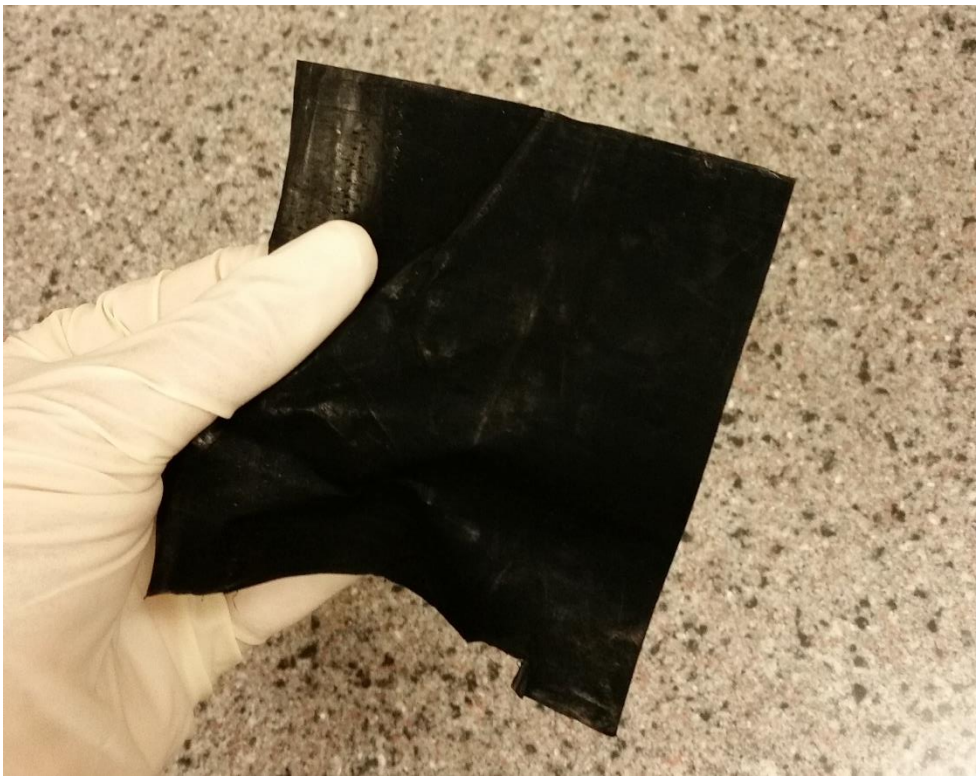

Figure 59: Carbon nanotube paper sheet

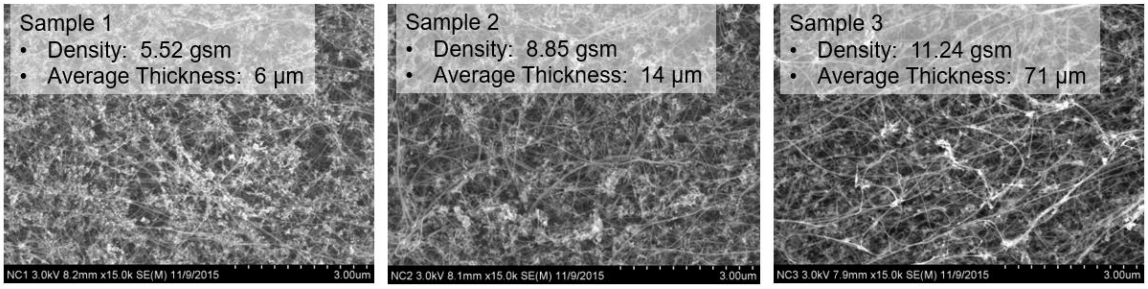

Figure 60: SEM images of CNT paper samples of varying densities and thicknesses. Magnification for all three is x15k.

Theoretically, CNTs should not intercalate lithium ions in the voltage range used for the LMO cathodes (3.5-4.5 V), however, to ensure the CNT paper was not making a contribution to the capacity, circles of blank (no LMO) CNT paper were put into coin cells and cycled as they would be if they contained active material. These results, shown in Figure 61 alongside a comparison LMO electrode, show that, as expected, the CNT paper does not contribute to the

capacity, and the mass of the CNT layers was therefore left out of the capacity normalization in future experiments.

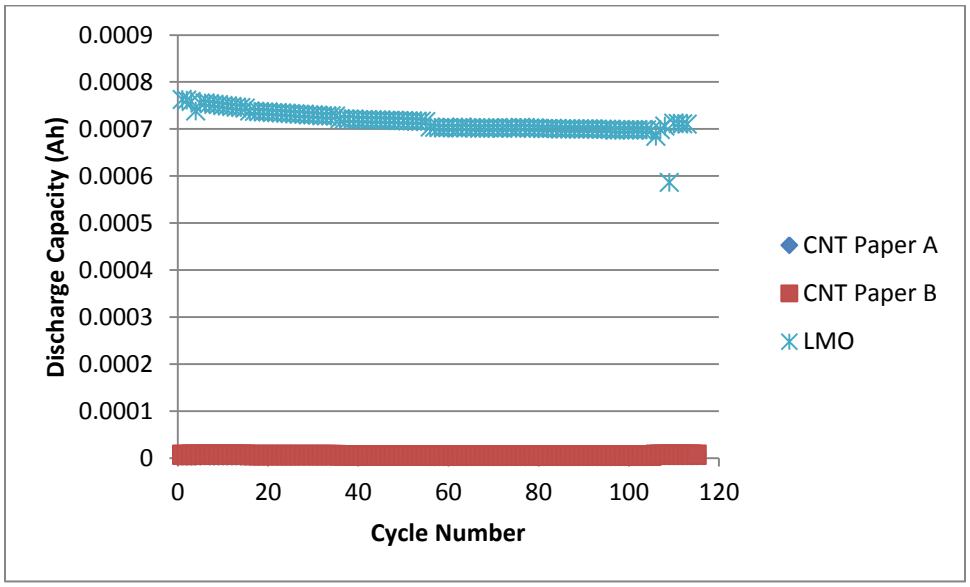

Figure 61: Cycling of blank CNT paper samples compared to an LMO electrode.

Electrodes were then fabricated using Samples 1,2, and 3 with loadings 3.36 mg, 3.87 mg, and 6.44 mg respectively. The process for making all three electrodes was identical; loadings increase as the density and thickness of the CNT paper sample increases because the thicker paper soaks up more active material slurry. Galvanostatic cycling results are shown in Figure 62. Like the experiment in the previous section, it can be seen that there is no appreciable performance difference between the different density samples. All show stable cycling over different charge/discharge rates and similar rate capability. Therefore, for the same reason of minimizing extra weight and volume in the cell, the thinner, less dense CNT paper is preferred.

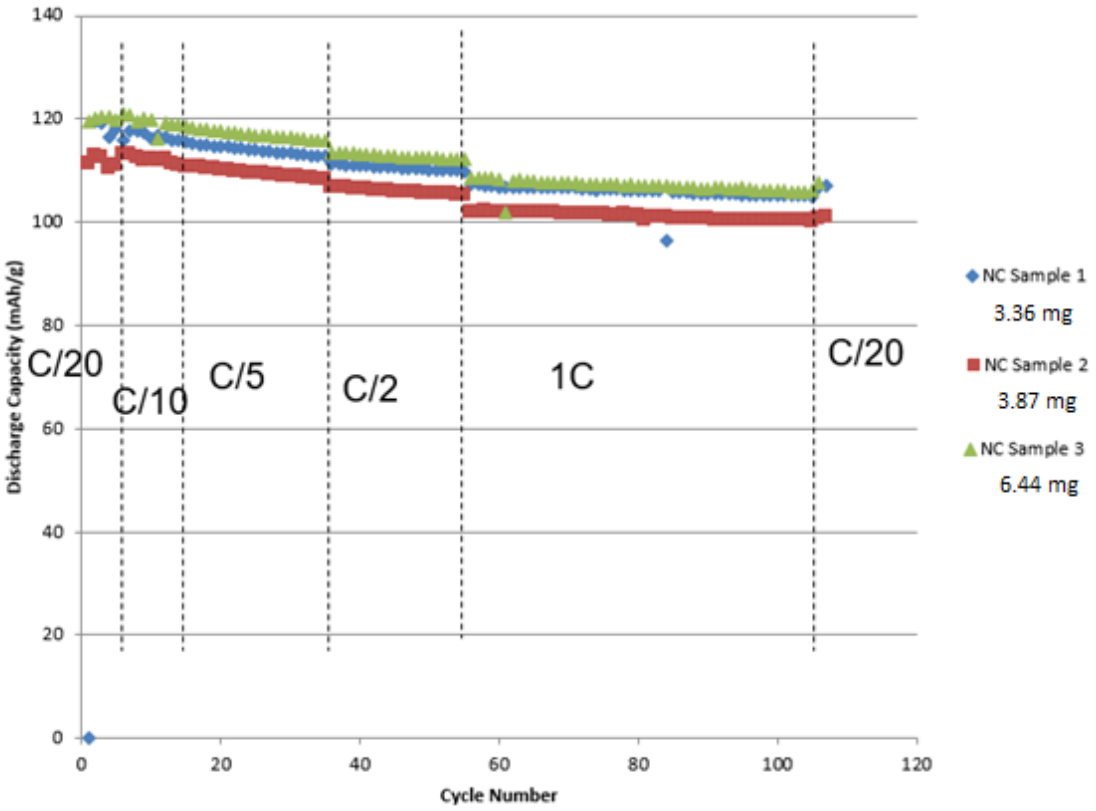

Figure 62: Cycling of CNT paper electrodes using CNT paper samples of varied density. Active material layer composition for all samples is LMO:CB:CNT:PVDF (85:9:1:5).

Figure 63 shows a comparison of a CNT paper electrode to a spray cast electrode of similar active material loading. Figure 63 a shows the galvanostatic cycling data, and Figure 63 b shows the energy and power density data for the same two cells. It is clear that both methods yield very similar performance, and so these two techniques can be used interchangeably depending on the application.

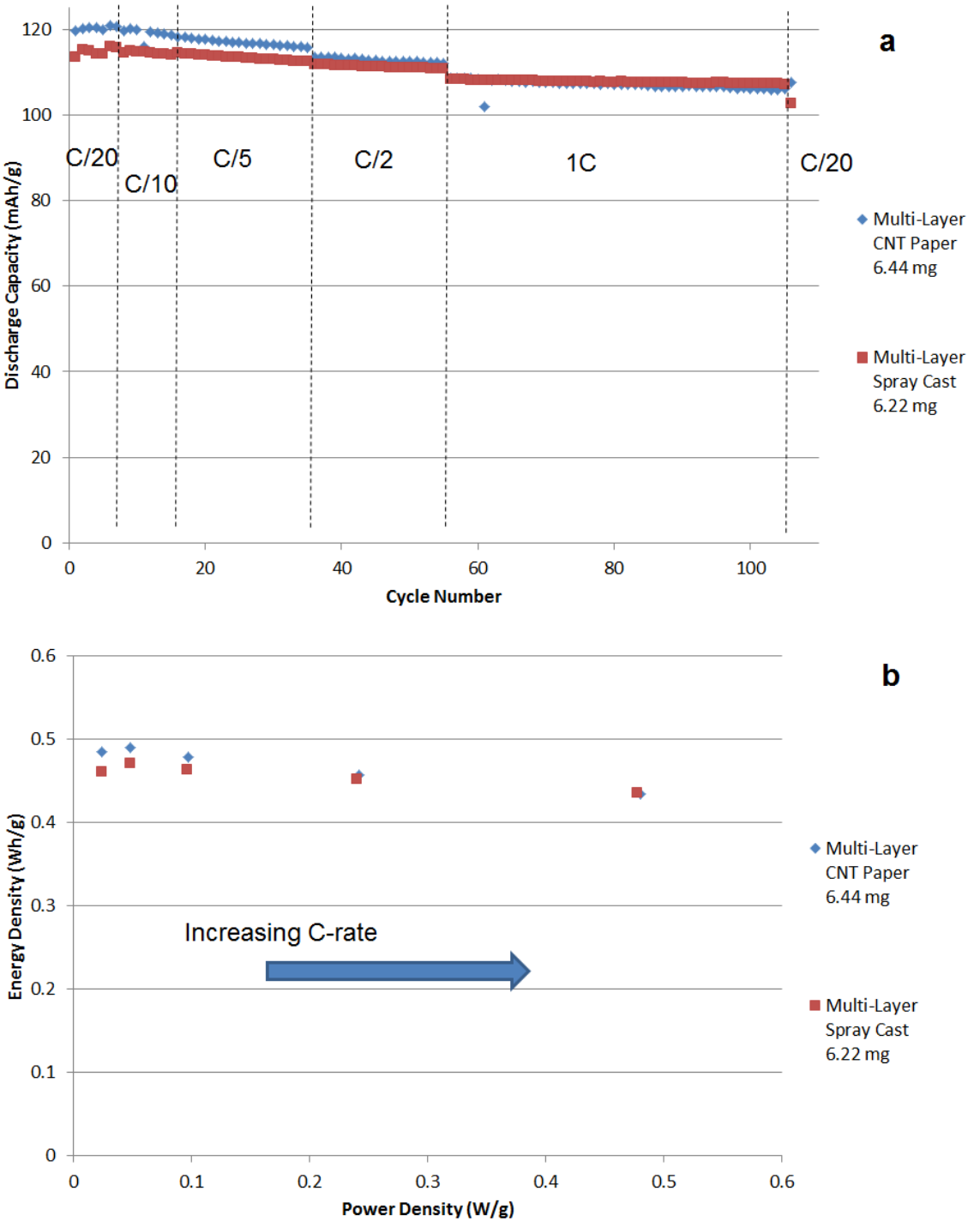

Figure 63: CNT paper electrode compared to a spray cast electrode with similar loading: a) Galvanostatic cycling results, b) Ragone plot. Active material layer composition for all samples is LMO:CB:CNT:PVDF (85:9:1:5).

3.5.6 Conclusions and Future Directions for LMO Cathodes

In this section it has been demonstrated that the performance enhancements originally seen in multi-layer LMO cathodes with low loading are also seen in multi-layer cathodes with higher loading, up to 65 mg. Compared to a standard fabrication LMO cathode of similar loading, a multi-layer cathode shows:

- 1.9 times the capacity at a rate of 2C
- 2 times the energy density at a rate of 2C
- 2.1 times the power density at a rate of 2C

In addition, the CNT layers were investigated to determine whether they supply adequate connectivity through the electrode and to identify an ideal density for peak performance. No change in performance was observed between a regular ten layer cathode and an interconnected ten layer cathode, therefore it can be concluded that the CNT layers already provide ample connection of the bulk material to the substrate. Likewise, no significant difference in performance was observed in electrodes with differing CNT layer densities, so it can be concluded that the presence of a CNT layer of any density is sufficient. In the interest of limiting the amount of inactive material in the cell, a low density CNT layer is preferred.

The multi-layer cells also substantially outperformed standard cells under the conditions required for high-power applications: slow charge rate and fast discharge rate. Under these conditions, the cells even performed better than the multi-layer cells previously mentioned. Compared to the standard cell, a five layer cell with higher loading shows:

- 3.2 times the capacity at a rate of 2C
- 3.5 times the energy density at a rate of 2C
- 1.2 times the power density at a rate of 2C

An alternative fabrication method was also demonstrated in which the sprayed CNT layers were replaced with a CNT paper sheet. Different sheet densities were tested and, like the sprayed CNT layers, there was no significant change in performance between electrodes with lower density, thin CNT sheets and higher density, thick CNT sheets. The thin sheets would

therefore provide favorable volumetric and gravimetric capacity, power, and energy. Electrodes made using this fabrication method showed very similar performance to the sprayed multi-layer electrodes, so it can be concluded that these methods are interchangeable, and the best method for the application can be chosen. The CNT paper electrodes are well suited to thin, flexible batteries because of their lack of substrate, while the sprayed electrodes have the advantage of adaptability: they can be any size or shape needed with little change to the fabrication process.

3.6 Graphite/Lithium Manganese Oxide Full Cells

Half cells use pure lithium foil as the counter electrode, as it provides an essentially unlimited amount of lithium ions to the system, however, this overabundance of lithium ions can cause plating at the anode, short circuiting, and lead to overheating, fire, or even explosion. Because of these safety concerns, lithium foil is not suitable for commercial anodes. Graphitic carbons are typically used in place of the lithium foil because they reversibly intercalate lithium ions at the low potential of 0.1 V, compatible with the working potential of lithium ion batteries. Ideally, the number of lithium ions being extracted from the cathode should equal the number being inserted into the anode. Too few lithium ions means the anode is not being fully utilized. Too many lithium ions leads to the same problem encountered in the case of lithium foil anodes: plating and shorting can occur. This means that full cell testing presents an extra challenge because the capacity of the anode must match the capacity of the cathode to make a full cell with good performance. The theoretical matching ratio can be obtained from the formula

$$\gamma = \frac{m_+}{m_-} = \frac{\Delta x\, C_-}{\Delta y\, C_+}$$

where m_+ and m_- are the mass loadings of the cathode and anode, respectively, C_- and C_+ are the gravimetric capacities of the cathode and anode respectively, and Δx and Δy are the amounts of cyclable lithium in each electrode. The theoretical value does differ from the practical value due various irreversible processes such as SEI layer formation. It is therefore necessary to use half cell data of the electrodes to be used in the full cell to find the matching ratio. Figure 64 gives

the half cell data for a LMO cathode and a graphite anode. From this data, a matching ratio of approximately 2.5 is obtained, which is in agreement with published data [85].

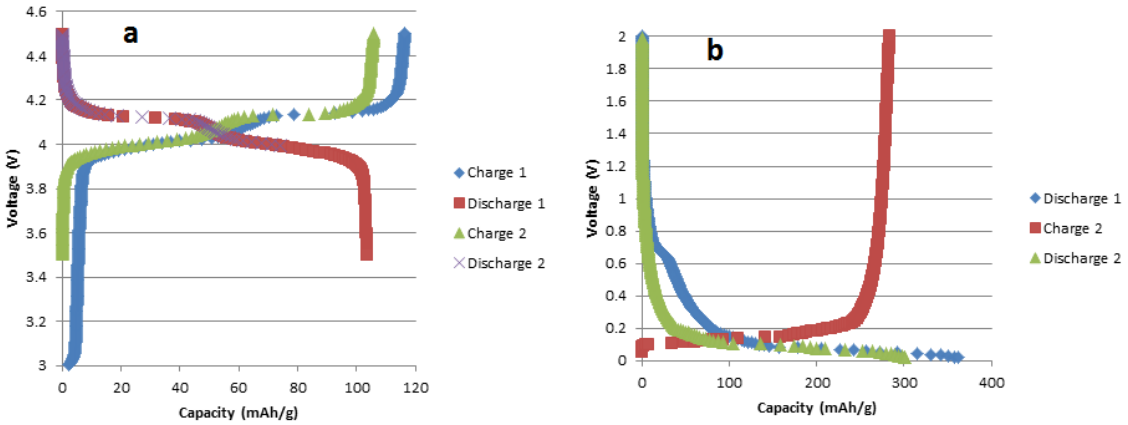

Figure 64: Half cell results for (a) LMO cathode and (b) graphite anode. Loading for the LMO cathode is 5.52 mg, for the graphite anode it is 2.24 mg.

Electrodes fitting this matching ratio were fabricated and assembled into full cells, the results of which are shown in Figure 65. Cells were cycled at C/20 for the first two cycles and then switched to 1C. This data shows fairly stable cycling capability but capacities far lower than expected for all cells. Because the half cells performed well, it is likely not a problem with the electrodes themselves, but an issue with the matching ratio.

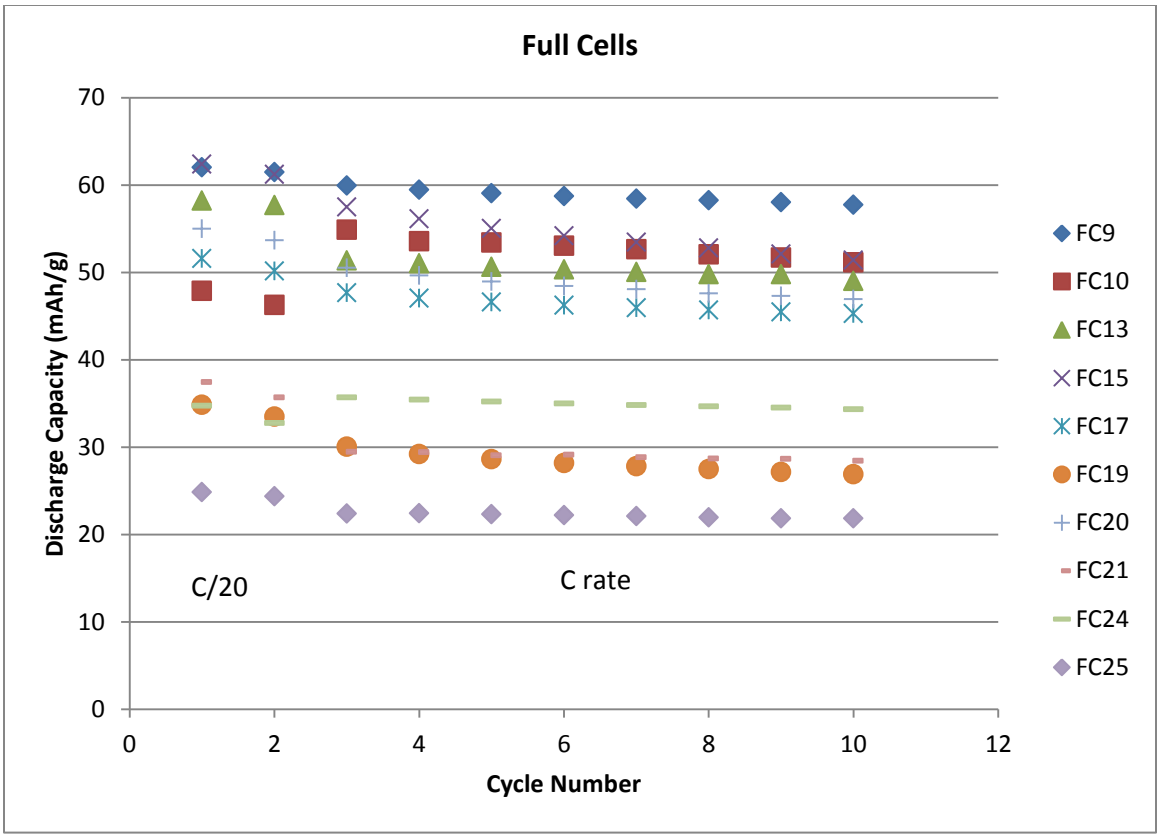

Figure 65: Cycling results for full cells with cathode : anode mass ratio of 2.5.

3.6.1 Determination of Ideal Matching Ratio

To determine a better matching ratio, cells were fabricated with cathode : anode mass ratios ranging from 2.50 to 3.13. Initial discharge capacities for these cells are plotted in Figure 66. From this graph, it can be seen that the matching ratio which will yield the highest capacity is somewhere between 2.75 and 3.00. New full cells were fabricated with cathode : anode mass ratios within this range. Cycling results are shown in Figure 67 a. While these cells clearly performed better than previous attempts, they are still not up to the same standard of performance as their half cell components. The voltage profiles for Full Cell 1 (cathode loading of 28.39 mg) in Figure 67 b show the characteristic two phase lithium intercalation at the rate of C/20 but become increasingly sloping when the rate is increased, indicating that there are side reactions during charging and discharging consuming lithium ions and causing the capacity fade.

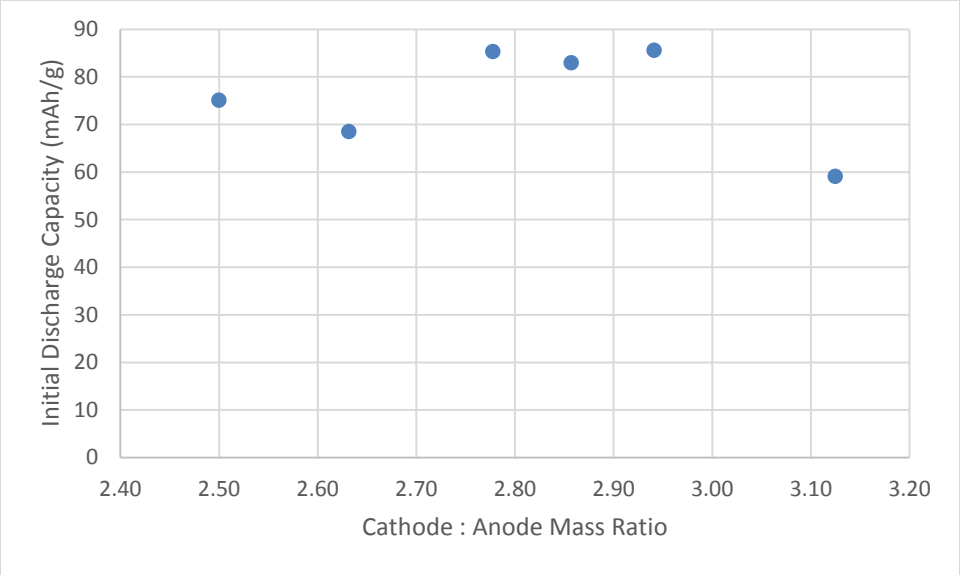

Figure 66: Initial discharge capacity versus matching ratio for graphite/LMO full cells

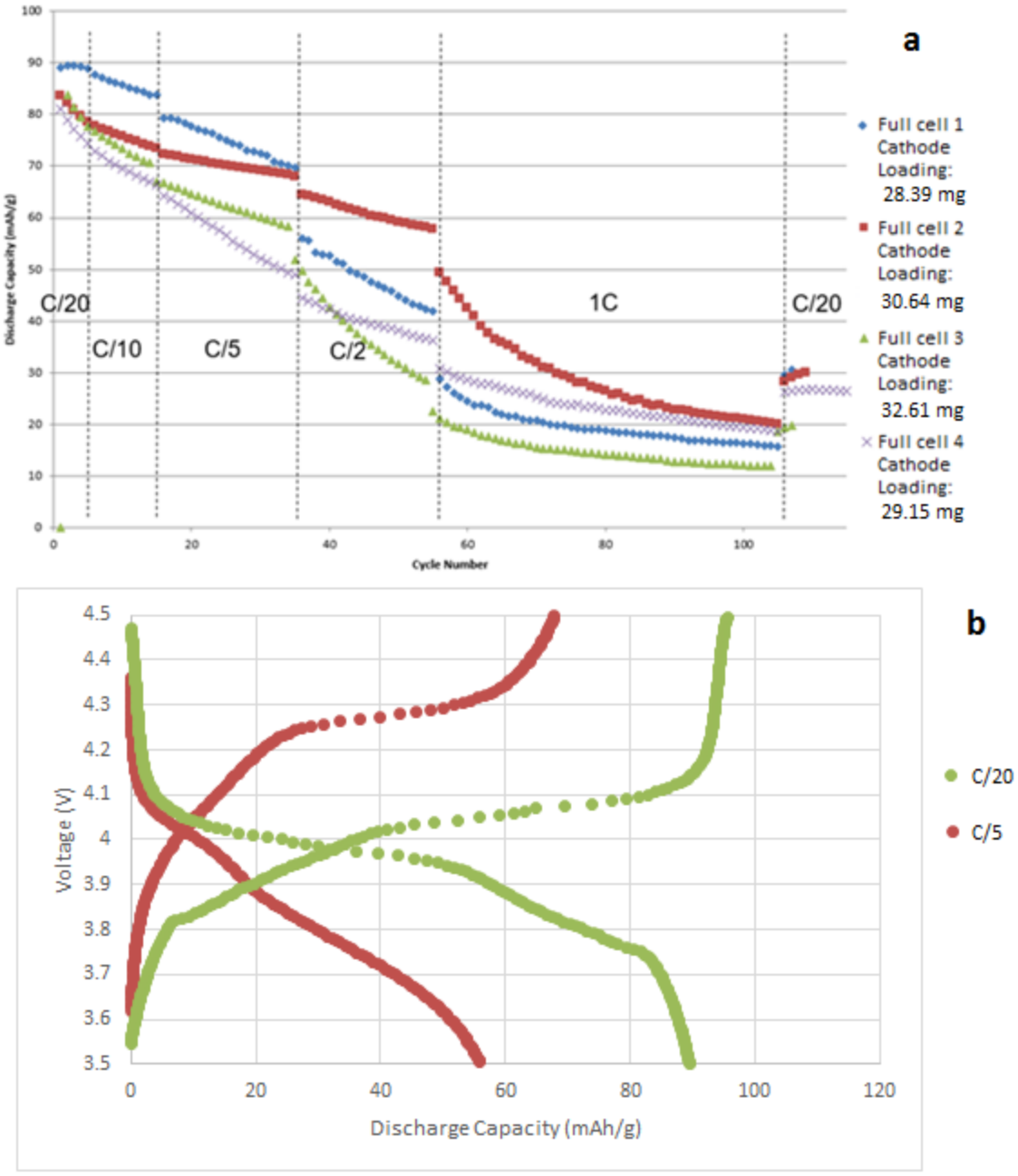

Figure 67: (a) Cycling results for graphite/LMO full cells with matching ratio of approximately 2.78. (b) Voltage profiles for Full Cell 1 (cathode loading 28.39 mg) at C/20 (green) and C/5 (red).

3.6.2 Conclusions and Future Directions for Full Cells

Cells were fabricated using calculated data, which compared well to published results, to determine the matching ratio. Performance of these cells was poor, however, so an experiment was designed to determine the ideal matching ratio by fabricating cells with a range of ratios near the expected result. The ideal matching ratio was found to be between 2.75 and 3.00 (cathode : anode ratio). Cells made with a ratio within this range showed significantly improved capacity, however capacity retention was still poor. Future work should address this issue by identifying the cause of the capacity fade.

4. Conclusions and Future Directions

Portable electronics have been rapidly progressing in recent years, however they are still limited by the batteries that power them. There is high demand for batteries to charge faster, last longer, and deliver higher energy and power, however this has proven to be a major challenge for engineers. Advances in nanomaterials show great potential to meet these demands in theory, but in practice have been difficult to implement because of the additional challenges they pose such as low packing density, high electrolyte reactivity, and expensive, complicated fabrication.

The multi-layer architecture described here aims to enhance the performance of lithium-ion batteries through the incorporation of a CNT scaffold which enhances the surface area of the substrate without increasing the footprint of the battery and also provides a conductive path through the electrode so that full utilization of the material can be achieved, even at higher charge and discharge rates. The fabrication procedure for this architecture has been developed using several different methods: doctor blade, spin casting, and spray casting. It was determined that spray casting creates the most uniform coating and is also best suited to commercialization.

The architecture was then applied to both a silicon anode and a lithium manganese oxide cathode. It was shown that the multi-layer architecture was able to enhance the silicon anode capacity, power density, and energy density, however the capacity fade issue still remains because of the degradation of the silicon material and SEI layer buildup. Several strategies to mitigate this problem were attempted including increasing the conductivity of the electrode with carbon additives, carbon coatings, alternative binders and doped particles, controlling SEI formation with electrolyte additives and by limiting the initial capacity, and retaining vacant space by reducing the pressure on the electrode during the pressing step of fabrication. Unfortunately, none of these strategies succeeded in stabilizing the capacity, therefore future work should continue to address the issue. Once a suitable form of silicon is found, this architecture will further enhance its performance.

Because cathode materials typically do not exhibit the degradation of silicon, the LMO cathodes showed much better performance. It was demonstrated that high-loading cathodes could be fabricated using the multi-layer architecture and would show about twice the capacity, energy density, and power density of a standard cell at a charge/discharge rate of 2C. This performance enhancement was even greater when the cells were charged at a low rate and then discharged at a high rate, the conditions necessary for high-power applications. The connectivity of the CNT network in these multi-layer cells was shown to be the same as an electrode with a direct connection to the substrate, proving the hypothesis that the CNTs would provide conductivity throughout the entire electrode. It was also shown that the same performance enhancement can be achieved with minimal CNTs, which is important in maintaining high gravimetric and volumetric energy and power density. Another method of fabrication is to substitute a CNT paper sheet for the sprayed CNT layers, and this was shown to provide the same performance enhancement.

The half cell data is helpful in improving the performance of each electrode individually, however it is also important to be able to create a full cell, since half cells cannot be commercialized. Initial experiments using calculated and theoretical data to get a matching ratio yielded poor capacity, so a range of matching ratios was tried to determine the true best fit for these cells. This was determined to be between 2.75 and 3.00 (cathode : anode ratio). The capacity of cells made using a ratio within this range was significantly higher, however the

capacity of these full cells faded much faster than half cells. Future work will need to address this issue before it will be possible to commercialize these batteries.

There are still a few challenges to be worked out in the future, however, once these concerns are addressed, the multi-layer architecture promises to deliver higher power and energy density, higher and more stable capacity with better rate capability, and longer cycle life, all with a high-rate and low-cost fabrication process that is easily adaptable to commercial processes and readily able to be scaled to meet commercial needs.

REFERENCES

1. Buchmann, I. *Battery University*. [Website] 2016 [cited 2016; Available from: http://batteryuniversity.com/.
2. MIT. *MIT Libraries Special Collections*. [cited 2016 February 1]; Available from: https://libraries.mit.edu/collections/.
3. CPC. *GP Batteries*. 2016 [cited 2016 February 3]; Available from: http://cpc.farnell.com/1/1/19913-gp-batteries-gp300sch1a1p-battery-ni-mh-tags-sub-c-1-2v-2200mah.html.
4. Sony. *Keywords to Understanding Sony Energy Devices*. 2016 [cited 2016 February 3]; Available from: http://www.sonyenergy-devices.co.jp/en/keyword/.
5. Curtiswood. *Battery Facts*. [cited 2016 February 1]; Available from: http://www.batteryfacts.co.uk/BatteryHistory/Plante.html.
6. Armand, M. and J.M. Tarascon, *Building Better Batteries.* Nature, 2008. **451**(7): p. 652-657.
7. Abraham, K.M., *Rechargeable Batteries for the 300-Mile Electric Vehicle and Beyond.* ECS Transactions, 2012. **41**(31): p. 27-34.
8. Scrosati, B. and J. Garche, *Lithium batteries: Status, prospects and future.* Journal of Power Sources, 2010. **195**(9): p. 2419-2430.
9. Thackeray, M.M., et al., *Spinel Electrodes from the Li-Mn-O System for Rechargeable Lithium Battery Applications.* Journal of the Electrochemical Society, 1992. **139**(2): p. 363-366.
10. Padbury, R. and X. Zhang, *Lithium–oxygen batteries—Limiting factors that affect performance.* Journal of Power Sources, 2011. **196**(10): p. 4436-4444.
11. Park, M., et al., *A review of conduction phenomena in Li-ion batteries.* Journal of Power Sources, 2010. **195**(24): p. 7904-7929.
12. *One Million Electric Vehicles by 2015*, in *February 2011 Status Report*, U.D.o. Energy, Editor. 2011.

13. Whittingham, M.S., *Materials Challenges Facing Electrical Energy Storage.* MRS Bulletin, 2008. **33**: p. 411-419.
14. Etacheri, V., et al., *Challenges in the development of advanced Li-ion batteries: a review.* Energy & Environmental Science, 2011. **4**(9): p. 3243.
15. *Advanced Space Transportation Program: Paving the Highway to Space*. 2008 [cited 2016 February 9]; Available from: http://www.nasa.gov/centers/marshall/news/background/facts/astp.html.
16. Wang, Y., et al., *Nano active materials for lithium-ion batteries.* Nanoscale, 2010. **2**(8): p. 1294.
17. Shah, A., *Electrode architectures for efficient ionic and electronic transport pathways in high-power lithium ion batteries*, in *Dept. of Electrical and Computer Engineering*. 2014, Northeastern University: Boston.
18. Fagas, G., ed. *Energy Storage: Battery Materials and Architectures at the Nanoscale*. ICT- Energy Concepts Towards Zero-Power Information and Communication Technology. 2014, InTech.
19. Ogihara, N., et al., *Theoretical and Experimental Analysis of Porous Electrodes for Lithium-Ion Batteries by Electrochemical Impedance Spectroscopy Using a Symmetric Cell.* Journal of The Electrochemical Society, 2012. **159**(7): p. A1034-A1039.
20. Griffiths, D.J., *Introduction to Electrodynamics*. 1999, Upper Saddle River, NJ: Prentice Hall.
21. Chagnes, A. and J. Swiatowska, eds. *Electrolyte and Solid-Electrolyte Interphase Layer in Lithium-Ion Batteries*. Lithium Ion Batteries - New Developments, ed. I. Belharouak. 2012.
22. Bard, A.J. and L.R. Faulkner, *Electrochemical Methods: Fundamentals and Applications*. 2001, Danvers, MA: John Wiley & Sons, Inc.
23. Zheng, H., et al., *A comprehensive understanding of electrode thickness effects on the electrochemical performances of Li-ion battery cathodes.* Electrochimica Acta, 2012. **71**: p. 258-265.
24. Marks, T., et al., *A Guide to Li-Ion Coin-Cell Electrode Making for Academic Researchers.* Journal of The Electrochemical Society, 2011. **158**(1): p. A51.
25. Tarascon, J.M. and M. Armand, *Issues and Challenges Facing Rechargeable Lithium Batteries.* Nature, 2001. **414**: p. 359-367.

26. Isidor, B., *Batteries in a Portable World - A Handbook on Rechargeable Batteries for Non-Engineers*. Third ed. 2011: Cadex Electronics.
27. Thackeray, M.M., *Lithium-Ion Batteries: An Unexpected Conductor.* Nature Materials, 2002. **1**: p. 81-82.
28. Thackeray, M.M., C. Wolverton, and E.D. Isaacs, *Electrical energy storage for transportation—approaching the limits of, and going beyond, lithium-ion batteries.* Energy & Environmental Science, 2012. **5**(7): p. 7854.
29. Lanz, M., et al., *Large-Agglomerate-Size Lithium Manganese Oxide Spinel with High Rate Capability for Lithium-Ion Batteries.* Journal of The Electrochemical Society, 2000. **147**(11): p. 3997-4000.
30. Huang, H., S.C. Yin, and L.F. Nazar, *Approaching Theoretical Capacity of LiFePO[sub 4] at Room Temperature at High Rates.* Electrochemical and Solid-State Letters, 2001. **4**(10): p. A170.
31. Thackeray, M.M., et al., *Li2MnO3-stabilized LiMO2 (M = Mn, Ni, Co) electrodes for lithium-ion batteries.* Journal of Materials Chemistry, 2007. **17**(30): p. 3112.
32. Belharouak, I., et al., *Safety characteristics of Li(Ni0.8Co0.15Al0.05)O2 and Li(Ni1/3Co1/3Mn1/3)O2.* Electrochemistry Communications, 2006. **8**(2): p. 329-335.
33. Croy, J.R., et al., *Li2MnO3-based composite cathodes for lithium batteries: A novel synthesis approach and new structures.* Electrochemistry Communications, 2011. **13**(10): p. 1063-1066.
34. West, W.C., et al., *Electrochemical Behavior of Layered Solid Solution Li2MnO3−LiMO2 (M = Ni, Mn, Co) Li-Ion Cathodes with and without Alumina Coatings.* Journal of The Electrochemical Society, 2011. **158**(8): p. A883.
35. Girishkumar, G., et al., *Lithium-Air Battery: Promise and Challenges.* Journal of Physical Chemistry Letters, 2010. **1**: p. 2193-2203.
36. Abraham, K.M., *Prospects and Limits of Energy Storage in Batteries.* The Journal of Physical Chemistry Letters, 2015. **6**(5): p. 830-844.
37. Bianco, S., ed. *Carbon Nanotubes--From Research to Applications*. 2011, InTech.
38. Lai, Y., et al., *Encapsulation of Selenium in Porous Hollow Carbon Spheres for Advanced Lithium-Selenium Batteries.* RSC Advances, 2014. **4**: p. 39312-39315.

39. Wang, W., R. Epur, and P.N. Kumta, *Vertically aligned silicon/carbon nanotube (VASCNT) arrays: Hierarchical anodes for lithium-ion battery.* Electrochemistry Communications, 2011. **13**(5): p. 429-432.
40. Park, M.-H., et al., *Silicon Nanotube Battery Anodes.* Nano Letters, 2009. **9**(11): p. 3844-3847.
41. Liu, N., et al., *A Yolk-Shell Design for Stabilized and Scalable Li-Ion Battery Alloy Anodes.* Nano Letters, 2012. **12**(6): p. 3315-3321.
42. Wu, H., et al., *Stable Cycling of Double-Walled Silicon Nanotube Battery Anodes Through Solid-Electrolyte Interphase Control.* Nature Nanotechnology, 2012. **7**: p. 310-315.
43. Kim, H., et al., *A Critical Size of Silicon Nano-Anodes for Lithium Rechargeable Batteries.* Angewandte Chemie International Edition, 2010. **49**(12): p. 2146-2149.
44. Green, M., et al., *Structured Silicon Anodes for Lithium Battery Applications.* Electrochemical and Solid-State Letters, 2003. **6**(5): p. A75.
45. Guo, J., X. Chen, and C. Wang, *Carbon scaffold structured silicon anodes for lithium-ion batteries.* Journal of Materials Chemistry, 2010. **20**(24): p. 5035.
46. Hu, Y.-S., et al., *Superior Storage Performance of a Si@SiOx/C Nanocomposite as Anode Material for Lithium-Ion Batteries.* Angewandte Chemie International Edition, 2008. **47**(9): p. 1645-1649.
47. Lee, J.K., et al., *Silicon nanoparticles–graphene paper composites for Li ion battery anodes.* Chemical Communications, 2010. **46**(12): p. 2025.
48. Wang, W. and P.N. Kumta, *Nanostructured Hybrid Silicon/Carbon Nanotube Heterostructures: Reversible High-Capacity Lithium-Ion Anodes.* ACS Nano, 2010. **4**(4): p. 2233-2241.
49. Zhao, X., et al., *In-Plane Vacancy-Enabled High-Power Si-Graphene Composite Electrode for Lithium-Ion Batteries.* Advanced Energy Materials, 2011. **1**(6): p. 1079-1084.
50. Kim, M.G. and J. Cho, *Reversible and High-Capacity Nanostructured Electrode Materials for Li-Ion Batteries.* Advanced Functional Materials, 2009. **19**(10): p. 1497-1514.
51. McDowell, M.T., et al., *25th Anniversary Article: Understanding the Lithiation of Silicon and Other Alloying Anodes for Lithium-Ion Batteries.* Advanced Materials, 2013. **25**(36): p. 4966-4985.

52. Wang, C., et al., *Self-Healing Chemistry Enables the Stable Operation of Silicon Microparticle Anodes for High-Energy Lithium-Ion Batteries.* Nature Chemistry, 2013. **5**: p. 1042-1048.

53. Zhang, Y., et al., *Composite anode material of silicon/graphite/carbon nanotubes for Li-ion batteries.* Electrochimica Acta, 2006. **51**(23): p. 4994-5000.

54. Honsberg, C. and S. Bowden. *PVEducation*. 3/11/16]; Available from: http://www.pveducation.org/pvcdrom/pn-junction/doping.

55. Liu, X.H., et al., *Ultrafast Electrochemical Lithiation of Individual Si Nanowire Anodes.* Nano Letters, 2011. **11**(6): p. 2251-2258.

56. Chakrapani, V., et al., *Silicon nanowire anode: Improved battery life with capacity-limited cycling.* Journal of Power Sources, 2012. **205**: p. 433-438.

57. Li, J., R.B. Lewis, and J.R. Dahn, *Sodium Carboxymethyl Cellulose.* Electrochemical and Solid-State Letters, 2007. **10**(2): p. A17.

58. Sivakkumar, S.R. and D.-W. Kim, *Polyaniline/Carbon Nanotube Composite Cathode for Rechargeable Lithium Polymer Batteries Assembled with Gel Polymer Electrolyte.* Journal of the Electrochemical Society, 2007. **154**(2): p. A134.

59. Chen, W.-M., et al., *Insight into the improvement of rate capability and cyclability in LiFePO4/polyaniline composite cathode.* Electrochimica Acta, 2011. **56**(6): p. 2689-2695.

60. Chen, L., et al., *Effect of vinylene carbonate (VC) as electrolyte additive on electrochemical performance of Si film anode for lithium ion batteries.* Journal of Power Sources, 2007. **174**(2): p. 538-543.

61. Etacheri, V., et al., *Effect of Fluoroethylene Carbonate (FEC) on the Performance and Surface Chemistry of Si-Nanowire Li-Ion Battery Anodes.* Langmuir, 2012. **28**(1): p. 965-976.

62. Hosono, E., et al., *Synthesis of Single Crystalline Spinel LiMn2O4 Nanowires for a Lithium Ion Battery with High Power Density.* Nano Letters, 2009. **9**(3): p. 1045-1051.

63. Chen, Y., et al., *Nano-sized LiMn2O4 spinel cathode materials exhibiting high rate discharge capability for lithium-ion batteries.* Journal of Power Sources, 2011. **196**(15): p. 6493-6497.

64. Liu, Z., et al., *Nanostructured TiO2(B): the effect of size and shape on anode properties for Li-ion batteries.* Progress in Natural Science: Materials International, 2013. **23**(3): p. 235-244.

65. Poizot, P., et al., *Nano-Sized Transition-Metal Oxides as Negative-Electrode Materials for Lithium-Ion Batteries.* Nature, 2000. **407**: p. 496-499.

66. Ding, Y.-L., et al., *Double-shelled hollow microspheres of LiMn2O4 for high-performance lithium ion batteries.* Journal of Materials Chemistry, 2011. **21**(26): p. 9475.

67. Jiao, F. and P.G. Bruce, *Mesoporous Crystalline β-MnO2—a Reversible Positive Electrode for Rechargeable Lithium Batteries.* Advanced Materials, 2007. **19**(5): p. 657-660.

68. Luo, J.-Y., et al., *Ordered Mesoporous Spinel LiMn2O4 by a Soft-Chemical Process as a Cathode Material for Lithium-Ion Batteries.* Chem. Mater., 2007. **19**: p. 4791-4795.

69. Li, C. and T.-W. Chou, *A structural mechanics approach for the analysis of carbon nanotubes.* International Journal of Solids and Structures, 2003. **40**(10): p. 2487-2499.

70. Thostenson, E.T., Z. Ren, and T.-W. Chou, *Advances in the Science and Technology of Carbon Nanotubes and their Composites: A Review.* Composites Science and Technology, 2001. **61**: p. 1899-1912.

71. Anantram, M.P. and F. Léonard, *Physics of carbon nanotube electronic devices.* Reports on Progress in Physics, 2006. **69**(3): p. 507-561.

72. Landi, B.J., et al., *Carbon nanotubes for lithium ion batteries.* Energy & Environmental Science, 2009. **2**(6): p. 638.

73. Hone, J., et al., *Thermal Conductivity of Single-Walled Carbon Nanotubes.* Physical Review B, 1999. **59**(4): p. R2514-R2516.

74. Yang, D.J., et al., *Thermal conductivity of multiwalled carbon nanotubes.* Physical Review B, 2002. **66**(16).

75. Jia, X., et al., *Building Robust Architectures of Carbon and Metal Oxide Nanocrystals Toward High-Performance Anodes for Lithium-Ion Batteries.* ACS Nano, 2012. **6**(11): p. 9911-9919.

76. Jiang, J., et al., *Recent Advances in Metal Oxide-based Electrode Architecture Design for Electrochemical Energy Storage.* Advanced Materials, 2012. **24**(38): p. 5166-5180.

77. Long, J.W., et al., *Three-Dimensional Battery Architectures.* Chem. Rev., 2004. **104**: p. 4463-4492.

78. Rolison, D.R., et al., *Multifunctional 3D nanoarchitectures for energy storage and conversion.* Chem. Soc. Rev., 2009. **38**(1): p. 226-252.

79. Corporation, M. [cited 2016 3/9/16]; Available from: http://www.mtixtl.com/Li-IonBatteryCathode-AluminumfoilsinglesidecoatedbyLiFePO4267m-1.aspx.

80. Bergin, S.D., et al., *New Solvents for Nanotubes: Approaching the Dispersibility of Surfactants.* Journal of Physical Chemistry C, 2010. **114**: p. 213-237.

81. Dirican, M., et al., *SiO2-confined silicon/carbon nanofiber composites as an anode for lithium-ion batteries.* RSC Advances, 2015. **5**: p. 34744-34751.

82. Beattie, S.D., et al., *Understanding capacity fade in silicon based electrodes for lithium-ion batteries using three electrode cells and upper cut-off voltage studies.* Journal of Power Sources, 2016. **302**: p. 426-430.

83. Ma, D., Z. Cao, and A. Hu, *Si-Based Anode Materials for Li-Ion Batteries: A Mini Review.* Nano-Micro Letters, 2014. **6**(4): p. 347-358.

84. Nanocomp Technologies, I. *Miralon Sheet and Tape*. 3/16/16]; Available from: http://www.nanocomptech.com/.

85. Arora, P., R.E. White, and M. Doyle, *Capacity Fade Mechanisms and Side Reactions in Lithium-Ion Batteries.* Journal of The Electrochemical Society, 1998. **145**(10): p. 3647-3667.